UNIVERSIDADE FEDERAL DO RIO DE JANEIRO

INSTITUTO DE FÍSICA

Exclusive production in pp and PbPb collisions at the LHCb experiment

Luiz Gustavo Silva de Oliveira

Ph.D. Thesis presented to the Graduate Program in Physics of the Institute of Physics of the Federal University of Rio de Janeiro - UFRJ, as part of the requirements to the obtainment of the title of Doctor in Sciences (Physics).

Advisor: Murilo Santana Rangel

Co-advisor: Erica Ribeiro Polycarpo Macedo

Rio de Janeiro

June/2019

Exclusive production in pp and PbPb collisions at the LHCb experiment

Luiz Gustavo Silva de Oliveira

Murilo Santana Rangel
Erica Ribeiro Polycarpo Macedo

Tese de Doutorado submetida ao Programa de Pós-Graduação em Física, Instituto de Física, da Universidade Federal do Rio de Janeiro – UFRJ, como parte dos requisitos necessários à obtenção do título de Doutor em Ciências (Física).
Aprovada por:

.....
Prof. Murilo Santana Rangel
(Presidente e Orientador)

.....
Profª. Erica Ribeiro Polycarpo Macedo
(Coorientadora)

.....
Prof. João Ramos Torres de Melo Neto

.....
Prof. Victor Paulo Barros Gonçalves

.....
Prof. Luiz Martins Mundim Filho

.....
Prof. Rogério Menezes de Almeida

.....
Prof. Sandro Fonseca de Souza

Rio de Janeiro, RJ – Brasil
Março de 2019

CIP - Catalogação na Publicação

O48e

Oliveira, Luiz Gustavo Silva de
Exclusive production in pp and PbPb collisions at the LHCb experiment / Luiz Gustavo Silva de Oliveira. -- Rio de Janeiro, 2019.
124 f.

Orientador: Murilo Santana Rangel.
Coorientadora: Erica Ribeiro Polycarpo Macedo.
Tese (doutorado) - Universidade Federal do Rio de Janeiro, Instituto de Física, Programa de Pós Graduação em Física, 2019.

1. LHCb. 2. Produção exclusiva. 3. Seção de choque. 4. Eletrodinâmica Quântica. 5. Cromodinâmica Quântica. I. Rangel, Murilo Santana, orient. II. Macedo, Erica Ribeiro Polycarpo, coorient. III. Título.

Elaborado pelo Sistema de Geração Automática da UFRJ com os dados fornecidos pelo(a) autor(a), sob a responsabilidade de Miguel Romeu Amorim Neto - CRB-7/6283.

Resumo

Produção exclusiva em colisões pp e PbPb no experimento LHCb

Luiz Gustavo Silva de Oliveira

Orientador: Murilo Santana Rangel

Coorientadora: Erica Ribeiro Polycarpo Macedo

Resumo da Tese de Doutorado apresentada ao Programa de Pós-Graduação em Física do Instituto de Física da Universidade Federal do Rio de Janeiro - UFRJ, como parte dos requisitos necessários à obtenção do título de Doutor em Ciências (Física).

O experimento LHCb é um dos quatro principais detectores instalados ao redor dos pontos de colisão dos feixes acelerados pelo LHC. Inicialmente o LHCb foi idealizado para o estudo de mésons B e D a fim de esclarecer a violação da simetria CP. Entretanto, este detector se mostrou também bastante eficaz no estudo de processos de produção exclusiva (CEP). Nesta tese apresentamos duas medidas de seção de choque de processos de produção exclusiva a partir dos dados coletados no LHCb durante os anos de 2011, 2012 e 2015. A seção de choque de produção eletromagnética de *dimúons* em colisões pp é realizada para duas energias no referencial do centro de massa: $\sqrt{s} = 7\,\text{TeV}$ com dados de 2011 e $\sqrt{s} = 8\,\text{TeV}$ com dados de 2012. O estudo da produção fotonuclear coerente de J/ψ em colisões PbPb com uma energia $\sqrt{s_{NN}} = 5\,\text{TeV}$ no centro de massa é realizado com dados coletados durante Novembro e Dezembro de 2015.

Palavras-chave: Seção de choque, Produção exclusiva, Cromodinâmica Quântica, Eletrodinâmica Quântica, LHCb, Pomeron.

Abstract

Exclusive production in pp and PbPb collisions at the LHCb experiment

Luiz Gustavo Silva de Oliveira

Advisor: Murilo Santana Rangel

Co-advisor: Erica Ribeiro Polycarpo Macedo

Abstract da Tese de Doutorado apresentada ao Programa de Pós-Graduação em Física do Instituto de Física da Universidade Federal do Rio de Janeiro - UFRJ, como parte dos requisitos necessários à obtenção do título de Doutor em Ciências (Física).

The LHCb experiment is one of the four main detectors installed around the points where beams collide after accelerated by LHC. Initially the LHCb was designed to study B and D mesons in order to elucidate the CP violation mechanism. However, this detector turned out fairly effective to study central exclusive production (CEP). Two cross-section measurements performed using the data collected during the years of 2011, 2012 and 2015 are described in this thesis. The cross-section of dimuon electromagnetic production is performed with pp collisions at two center-of-mass energies: $\sqrt{s} = 7\,\text{TeV}$ with 2011 data and $\sqrt{s} = 8\,\text{TeV}$ with 2012 data. The study of coherent photonuclear production of J/ψ at a nucleon-nucleon center-of-mass energy $\sqrt{s_{NN}} = 5\,\text{TeV}$ is performed with PbPb collisions collected during November and December of 2015.

Keywords: Cross-section, Exclusive production, Quantum Chromodynamics, Quantum Electrodynamics, LHCb, Pomeron.

Acknowledgements

I would like to thank God for giving me the opportunity to study and learn the nature He created. It is a pleasure and an honor. I thank my wife for all unconditional support and love. Sometimes I think I don't deserve it so much but I am really grateful for having it in my life. I thank my parents for giving me all the help needed during the hard times and beyond. You are my heroes!

I am very grateful to my advisors. Murilo and Erica showed me many times how a true researcher behaves. Your support and guidance were fundamental. I could not reach this day without both of you, literally.

I thank the staff and professors of Physics Institute of UFRJ. It was a 11-years journey since the undergraduation admission and through all these years I always found help and support for bureaucracy and the doubts about courses subjects.

Last but not least I thank CAPES for all the financial support.

Contents

List of Figures

List of Tables

Chapter 1

Introduction

The Standard Model [1] is the most successful theory describing the fundamental particles and forces. Quarks and leptons are recognized as elementary particles and Strong, Weak and Electromagnetic are the fundamental forces. Particles have particular characteristics such as electric charge, intrinsic angular momentum (spin), colour, among others. A particle's electric charge can be represented by a multiple of the electron charge absolute value (e), *e.g.*, the muon lepton (μ) has charge number equal -1. Similarly, the spin of a particle can be expressed by a multiple of the Planck reduced constant, $\hbar$. The spin of all quarks and leptons are semi-integer multiples and therefore they are fermions and obey the Pauli exclusion principle. Particles with integer spin are called bosons. Except for the neutrinos, all quarks and leptons have electric charge but only quarks have colour. The colour can assume the values red, green or blue and whilst only charged particles can interact via electromagnetic force, only coloured particles can interact via strong force. The interactions are mediated by the exchange of force carriers: photons are exchanged by particles interacting electromagnetically and gluons are exchanged in a strong interaction. Both photon and gluon are bosons.

Two sectors of the Standard Model are particularly important for the objectives of this document: Quantum Electrodynamics (QED) and Quantum Chromodynamics (QCD). They are quantum field theories describing the electroweak and the strong forces, respectively. QED is the most accurate and precise physics theory [2]. On the other hand, the

QCD sector brings up open questions [3]. An attempt to conceive theoretical insights using experimental results is in progress making use of **C**entral **E**xclusive **P**roduction (CEP) processes. CEP is a special type of production in which the initial particles (protons or heavy ions) remain structurally intact after the collision.

There is a growing interest in CEP processes currently in the experimental high energy physics community since these processes show a low detector activity environment: only the particles exclusively produced or their decay products deposit energy in the subdetectors. Therefore, CEP is a extremely clean signal in terms of track multiplicity. Since the beam particles remain intact after they collide, the interaction between them occurs mainly by the exchange of colourless objects. Particularly two known objects satisfy these requirements: photon and pomeron.

Photon mediated processes can be calculated with high accuracy within the QED framework. Therefore a cross-section measurement of an "electromagnetic" process can be translated in a luminosity calibration [4]. This is why these processes are called "standard candles". However there are quantum-mechanical processes forbidden in the classical theory of electrodynamics only accessible at large electromagnetic field strengths. Recently evidence of light-by-light scattering was reported by one of the experiments at LHC and the measured cross-section is in agreement with Standard Model predictions [5]. On the other hand discrepancy of experimental results of physical observables of the very well known predictions can indicate an insight of new physics beyond Standard Model, *e.g.*, the anomalous coupling in the production of W bosons in photon-photon scattering could be observed at the LHC [6, 7, 8].

The pomeron [9] was initially postulated as a Regge trajectory [10] in order to describe the slow growth of production cross-sections of hadronic processes. In the QCD, the pomeron is represented by a double gluon exchange. However, the pomeron existence lacks experimental confirmation. CEP processes constitute one of the great candidates to provide this confirmation. In this context the photonuclear production of mesons in

heavy ions collisions can be insightful [11].

In heavy ions collisions, photonuclear production can occur in ultra-peripheral collisions where the distance between their centers is greater than the sum of radii. In this case, the cloud of virtual photons of each ion can interact with the other ion in a coherent photonuclear interaction. The cross-section of this type of production is sensitive to the gluon distribution and a measurement of this value can help to constrain this distribution function and reduce its uncertainty. ALICE collaboration is one of the four main experiments in LHC and has measured this type of production using PbPb collisions with center-of-mass energy of $\sqrt{s_{NN}} = 5.02\,\text{TeV}$ [12].

In this thesis two cross-section measurements are described. Both analyses are performed using data collected by the LHCb detector. LHCb is one of the main detectors collecting data from both proton and heavy ions collisions at the LHC. During 2011 and 2012 a data sample corresponding to an integrated luminosity of $\sim 3\,\text{fb}^{-1}$ was collected using protons collisions. The center-of-mass energy of the collisions was $\sqrt{s} = 7\,\text{TeV}$ during 2011 and $\sqrt{s} = 8\,\text{TeV}$ during 2012. The cross-section measurement is performed separately for each year since the cross-section is expected to vary with the collision energy. The process studied with this data is the CEP of a $\mu^+\mu^-$ pair (dimuon). During November and December of 2015 an integrated luminosity of $\sim 10\,\mu\text{b}^{-1}$ of PbPb collisions was recorded at nucleon-nucleon center-of-mass energy $\sqrt{s_{NN}} = 5\,\text{TeV}$. The J/ψ coherent production is studied with this sample. The cross-section measurement is performed in bins of J/ψ rapidity and a comparison with some of the main theoretical predictions is presented.

In the next chapter, a brief review of the two phenomena is described. The LHC machine and the LHCb detector are described in Chapter 3. Chapters 4 and 5 are the core of this document, where the two analyses are detailed. The last chapter is devoted to the conclusions of this work.

Chapter 2

Theoretical aspects and previous measurements

The idea of atomic theory has been in philosophy for a long time. According to this theory all observed matter can be subdivided into smaller and smaller objects, but there would be a limit to this division: the atom, as the name itself supposes, would be indivisible. After millennia of hypotheses and research, trial and error, the answer seems closer. The aim of this chapter is to describe the current knowledge of some of the fundamental particles and their interactions. The historical approach presented in this section and the next one is inspired in references [13] and [14]. A set of textbooks are available also [15, 16, 17].

Atoms are presently understood as structures compounded by fundamental particles. Therefore the term *atom* is no longer used as a synonymous of indivisible. There are two types of indivisible particles present in the atom arrangement: electrons and quarks. Electrons are the particles constituting the cloud of negatively charged particles surrounding the atomic nucleus. The nucleus is composed of neutrons and protons but those are not fundamental particles, *i.e.*, both neutron and proton are bound states of quarks.

The Rutherford atomic model, foremost reported in the 1911's article [18], was the first theory to describe the atomic scheme as a positive nucleus with a eletrosphere. However, many questions raised from this scheme. The main question for the purposes of this work

is: why protons do keep so close from each other and do not separate by electromagnetic repulsion?

2.1 Strong force

The experiments performed by Hans Geiger and Ernest Marsden between 1908 and 1913 under Rutherford's guidance proved the existence of electrical positive particles inside the atomic nucleus. It may be considered as the birth of strong force hypothesis. In fact, if there were positive particles inside atomic nucleus why would them persist together as there is an electromagnetic repulsion between them? A new interaction was proposed, stronger than the electromagnetic and in opposite way.

Further, in 1932, Chadwick discovered the neutrons. These particles are heavier than protons by a very small fraction and they are not electrically charged. The absence of electrical charge brought a broader hypothesis about the strong force: both protons and neutrons can interact via this new force, otherwise they would not persist inside the nuclear structure. In order to explain this behaviour, Heisenberg proposed soon after a new quantum number called isospin. The brand-new strong interaction would be insensible to the charge of particles but not to the isospin. In fact, Heisenberg hypothesis was that the isospin would be unaltered after a strong interaction. It would be a conserved quantity just like electrical charge is conserved in electromagnetic processes.

A similar intriguing feature was observed in another property of nucleons (neutrons and protons): the magnetic momentum. At the time of the discovery of the nucleons, they were regarded as fundamental particles like electrons. In fact, it makes sense at a first glance: all particles in the atom would be fundamentals. The intrinsic magnetic momentum is null for a fundamental particle without electrical charge. However, the intrinsic magnetic momentum of the neutron was found to be non-zero and the intrinsic magnetic momentum of the proton was found to be larger than expected, indicating that there could be an extra dipole momentum.

In 1964, Murray Gell-Mann and George Zweig proposed independently the quark model. In this model, quarks are the fundamental constituents of matter and the nucleons are formed by combinations of these fundamental particles. Each of these quarks have a half-integer spin and, if the neutron is compounded by quarks, there could be a non-zero dipole momentum and therefore a non-zero intrinsic magnetic momentum. The quark model started with the prediction of three quarks. A total of six quarks were observed and the quark model was updated in order to describe all of them. They are represented in Figure 2.1.

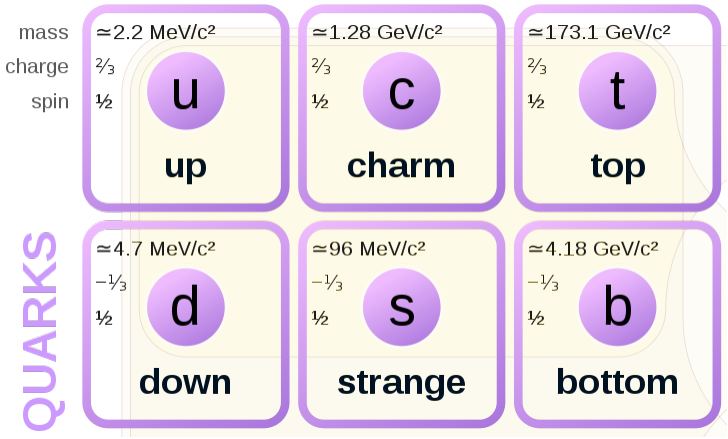

Figure 2.1: A chart with all six quarks and their respective mass, electrical charges and spins [19].

Baryons, like protons and neutrons, are bound states of three quarks and mesons, like J/ψ, are bound states of two quarks. The quark content of these particles are

$$p = uud$$

$$n = udd$$

$$J/\psi = c\bar{c}$$

The total spin of baryons and mesons can be obtained by adding the spin of all quarks within. It becomes clear that mesons can only have integer spin, thus they are bosons. On the other hand, the baryons are only allowed to have half-integer spin, making them

fermions. Fermions obey the Pauli principle that requires a wave function containing identical fermions to be totally antisymmetric. It does not represent any problem in the current scenario as all considered particles can easily obey this principle. In the proton case there are three quarks and two of them are from the same kind, u, but if one of them is spin-up and the other one is spin-down the Pauli principle is complied. It is easy to see the same feature occurs for the neutron and J/ψ. However it is not possible to explain the existence of all baryons in this way. In the mid-1950s at the University of Chicago cyclotron and the Carnegie Institute of Technology synchro-cyclotron established the Δ resonances. One of them is particularly interesting to this discussion. The Δ^{++} resonance is the bound state of three u quarks,

$$\Delta^{++} = uuu.$$

Therefore the wave function for this state, with three identical fermions, would be symmetric under the exchange of any two quarks. Of course this would be incompatible with the Pauli principle and the Δ^{++} would be an state that this quark model could not describe, unless there was a new quantum number with three possible states for quarks. This additional degree of freedom was called *colour* and it can come in three different values: red, blue and green. In the Δ^{++} case, each u quark has a colour different from the other two. Moreover, it is possible for a quark to have an anticolour, *e.g*, the quark-antiquark pair of J/ψ shows this feature. Thus, all hadrons have null net colour charge.

At first, colour was regarded purely as a quantum number needed for phenomenological reasons for understanding the nucleons internal structure. Many observations and examples showed, though, that the colour is not simply a theoretical tool but rather a physical quantum number. One of these examples was the eletron-positron annihilation into a $q\bar{q}$ pair, which occurs through a virtual photon, as showed in Figure 2.2.

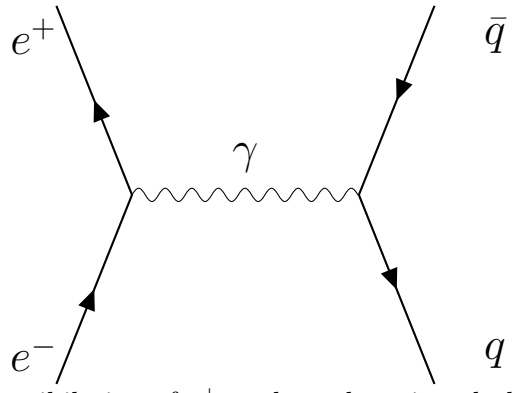

Figure 2.2: The annihilation of e^+e^- through a virtual photon into $q\bar{q}$ pair.

The total cross-section of quark-antiquark pair production is dependent on the number of possible $q\bar{q}$ final states. If the colour is a physical degree of freedom there must be more numbers of final states (with different colours distributions) and than a higher cross-section is observed. Indeed, the measurements are consistent with exactly three colours for quarks. On the other hand, there is no evidence of existence of coloured leptons. In fact, the colour is not just another degree of freedom but the charge of strong interactions. Leptons do not interact strongly because they do not feature colours just as neutrons do not interact with electric fields because of the lack of electrical charge.

On the other hand, if hadrons were colourless too, it would imply that they do not interact strongly and therefore the strong interaction would not be useful to explain how the protons remain combined in atomic nucleus.

Nevertheless, hadrons are not fully colourless. It turns out the cancellation is not quite absolute and a residual strong force arises between protons and neutrons. It is analogue to the Van der Waals force between charge-neutral molecules. Van der Waals force is a residual electromagnetic force that reflects the charged atoms content of molecules. It is known that the residual electromagnetic force falls more rapidly with distance than the original electromagnetic interaction. The residual strong force is also very short-range and its effects are only relevant within a few femtometers.

At the time strong force was discovered and its theory, QCD, was developed, the

QED was already very successful. A very noteworthy aspect of QED was the existence of electromagnetic carriers also known as photons. Photons are massless, electrically neutral bosons (spin = 1) responsible for carrying the electromagnetic force from a charged particle to another charged particle. The null electrical charge of photons is an important feature as these particles can not auto interact.

Similarly to QED, the gluon was postulated as the carrier of the strong force. In 1968, after deep-inelastic electron-proton scattering experiments of SLAC, Bjorken and Feynman interpreted these measurements with the parton model. In this model, not only quarks were inside the proton but other kinds of partons too. Chris Llewellyn-Smith proposed a measurement of the fraction of proton momentum carried by the quarks as a test to establish if there could be other partons. The experiment was carried out and the results confirmed that about half of the proton momentum was not carried by its quarks. It was the first evidence of the existence of gluons.

In 1976, John Ellis, Graham Ross and Mary Gaillard calculated the gluon bremsstrahlung in electron-positron annihilation with three jets in final state, $e^+e^- \to \bar{q}qg$. In June of 1979, the TASSO collaboration observed the first three-jets event and the existence of gluon was proved. Many questions have arisen since this discovery. In this document we aim to improve the answer to one of these questions: what is the nuclear gluon density distribution at large energy scales?

First, we discuss the exclusive production of dimuons in pp interactions at LHCb. The cross-section for this reaction can be used as a standard candle of the experiment since it can be compared to precise QED theory calculations. Second, the data analysis of the coherent production of the vector meson J/ψ in PbPb collisions at the LHCb experiment is described.

2.2 Central exclusive production in pp collisions

CEP processes feature the exchange of a colourless electrically neutral singlet object carrying an energy fraction x of proton and the exchanged object can either be a pomeron or a photon. The photon virtuality is defined as $Q^2 = -q^2$ where q is the four-momentum transfer.

In the QCD framework, the pomeron is described as a bound state of at least two gluons [20, 21] in order to transfer the momentum building the centrally produced system and cancel colour flow in the interaction. It carries the same quantum numbers as the vacuum state [22].

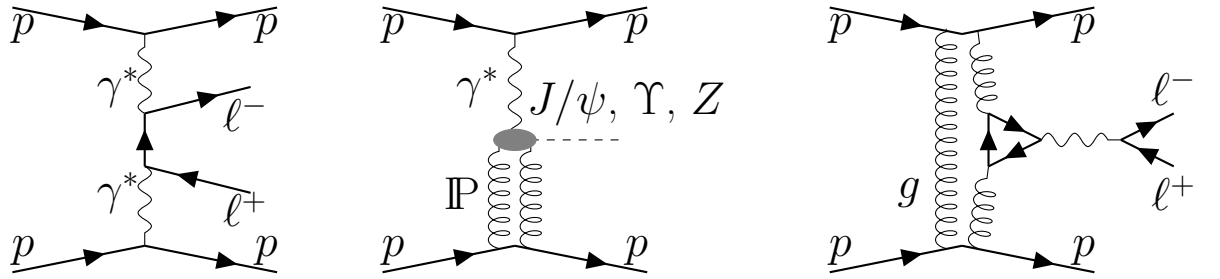

(a) Two-photon exchange

(b) Photon-pomeron fusion (photoproduction)

(c) Double-pomeron exchange (DPE)

Figure 2.3: Examples of exclusive processes in proton-proton scatterings.

Starting with two kinds of particle exchange three general classes of interactions can occur. These classes are represented in the diagrams of the Figure 2.3. In all the three possible interactions, $\gamma\gamma$, $\gamma\mathbb{P}$ and $\mathbb{P}\mathbb{P}$, a distinctly isolated and well-defined central system is present. The two-photon processes (Figure 2.3a) [23, 24] are since long time studied and they are regarded as the main contribution to the cross-section of lepton pairs in hadronic collisions at LHCb energy range and kinematic region [25, 26]. The photoproduction of vector mesons in pp collisions (Figure 2.3b) constitute one of the backgrounds for this analysis and it is removed by excluding the mass windows around the invariant masses of the mesons. The double-pomeron exchange production (Figure 2.3c) of lepton pairs

presents a cross-section much smaller than the two-photon contribution. In the considered kinematic region, it is predicted to be smaller by 2 to 4 orders of magnitude.

Considering the low virtuality reaction $pp \to p\mu^+\mu^- p$ in the two-photon mechanism, the cross-section is calculated within the framework of the **E**quivalent **P**hoton **A**pproximation (EPA) [27]:

$$\sigma_{pp\to p\mu^+\mu^- p} = \int_{W_0}^{\sqrt{s}} dW_{\gamma\gamma} \frac{d\mathcal{L}_{\gamma\gamma}}{dW_{\gamma\gamma}} \sigma_{\gamma\gamma\to\mu^+\mu^-}, \tag{2.1}$$

where $\sigma_{\gamma\gamma\to\mu^+\mu^-}$ is the $\gamma\gamma \to \mu^+\mu^-$ QED cross-section [23], $W_{\gamma\gamma}$ is the two-photon center-of-mass energy, W_0 is the minimal two-photon centre of mass energy allowed by the full process kinematics. The relative two-photon luminosity spectrum is defined in [28]:

$$\frac{d\mathcal{L}_{\gamma\gamma}}{dW_{\gamma\gamma}} = \int dx \frac{2}{xs} W_{\gamma\gamma} f_\gamma(x) f_\gamma\left(\frac{W_{\gamma\gamma}^2}{xs}\right), \tag{2.2}$$

where f_γ is the photon flux and a numerical estimation is presented in Figure 2.4 for pp collisions with 7 TeV center-of-mass energy. This figure uses a parameterisation extracted from ep collisions at HERA. In this figure, the solid line corresponds to the two-photon CEP of dimuons with both protons remaining intacts after collision. It represents the reaction studied in Chapter 4. The dashed line in Figure 2.4 corresponds to the case when one of the protons do not remain intact. This case is called *semi-inelastic* or *single dissociative*. The dotted line corresponds to the process when both protons dissociate and it is commonly called *fully-inelastic* or *double dissociative*. These semi- and fully-inelastic contributions are irreducible backgrounds to the analysis presented in this thesis. These three possible outcomes can be ordered by the virtuality of the emitted photons. The higher the virtuality the greater is the probability of dissociation.

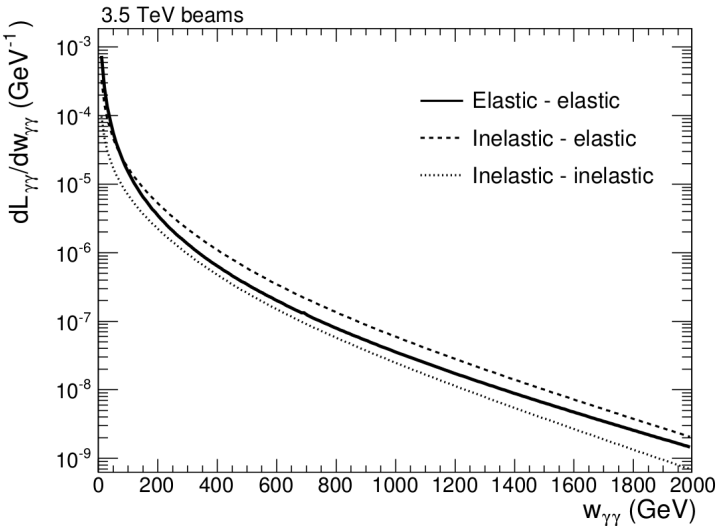

Figure 2.4: Integrated photon flux as given by the equivalent photon approximation, for the elastic, the single- and the double-dissociative proton case. The elastic contribution is simulated using a maximal momentum transfer $Q^2_{max} = 2\,\mathrm{GeV}^2$, while the dissociative cases use $Q^2_{max} = 300\,\mathrm{GeV}^2$. Figure extracted from reference [29].

The cross-section of CEP dimuon is predicted by Equation 2.1 using the relative two-photon luminosity spectrum of elastic process. The photon flux is a function of the electric and magnetic form factors and can be assessed through the dipole approximation [30, 31]. The integration is performed by the SuperChic event generator [32]. The resultant cross-section is dependent of many factors including the center-of-mass energy of pp collisions, $\sqrt{s}$, and the pseudorapidity acceptance of the detector. The results for the energies of Run 1 integrated over the LHCb acceptance are showed in Equations 2.3 and 2.4.

$$\sigma_{theo}(pp \to p\mu^+\mu^- p, \sqrt{s} = 7\,\mathrm{TeV}) = (158.66 \pm 1.02)\,\mathrm{pb} \tag{2.3}$$

$$\sigma_{theo}(pp \to p\mu^+\mu^- p, \sqrt{s} = 8\,\mathrm{TeV}) = (166.81 \pm 0.98)\,\mathrm{pb} \tag{2.4}$$

Previous measurements of the cross-section of CEP dilepton using the LHC data show good agreement between experimental results and theoretical predictions [33, 34, 35] (see Figure 2.5 for Run 1 and Figure 2.6 for Run 2 results). The cross-section measured by

LHCb in 2010 data ($\sqrt{s} = 7\,\text{TeV}$) is [36]

$$\sigma(pp \to p\mu^+\mu^- p, \sqrt{s} = 7\,\text{TeV}, m(\mu^+\mu^-) > 2.5\,\text{GeV}/c^2) = 67 \pm 10(\text{stat.}) \pm 7(\text{syst.}) \pm 15(\text{lumi.})\,\text{pb}, \tag{2.5}$$

and the prediction calculated by the LPair event generator [37] for the same kinematic region is 42 pb with an error of less than 1%.

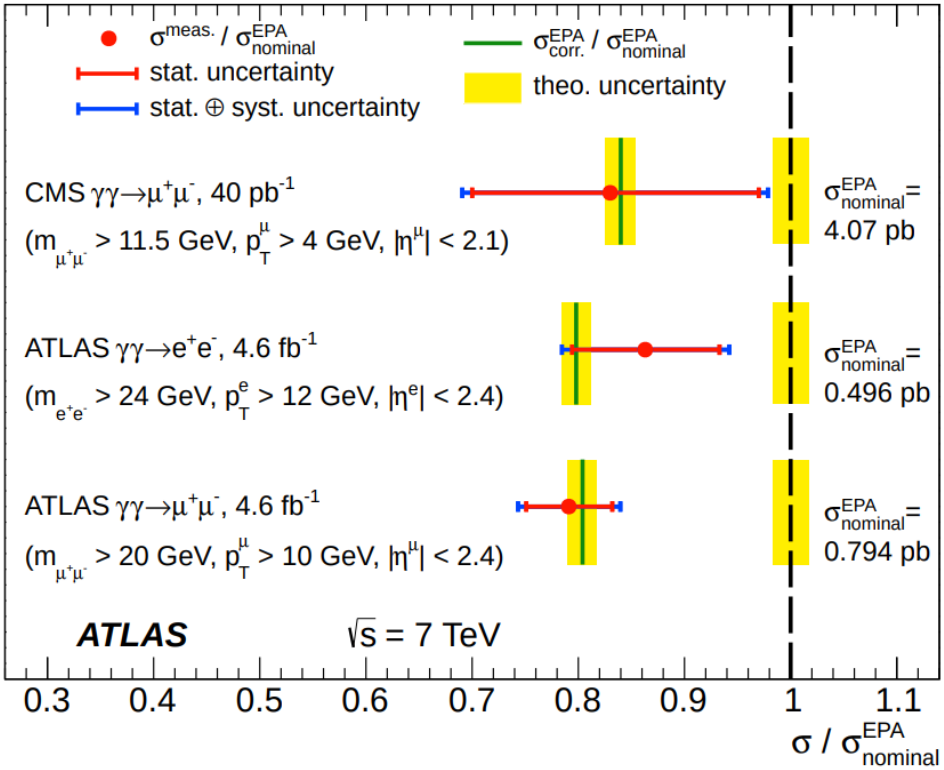

Figure 2.5: Comparison of the ratios of measured (red points) and predicted (solid green lines) cross-sections to the uncorrected EPA calculations (black dashed line). Results for the muon and electron channels are also compared with a similar CMS measurement [33]. The inner red error bar represents the statistical error, and the blue bar represents the total error on each measurement. The yellow band represents the theoretical uncertainty of 1.8% (1.7%) on the predicted (uncorrected EPA) cross-sections, assumed to be uniform in the phase space of the measurements [34].

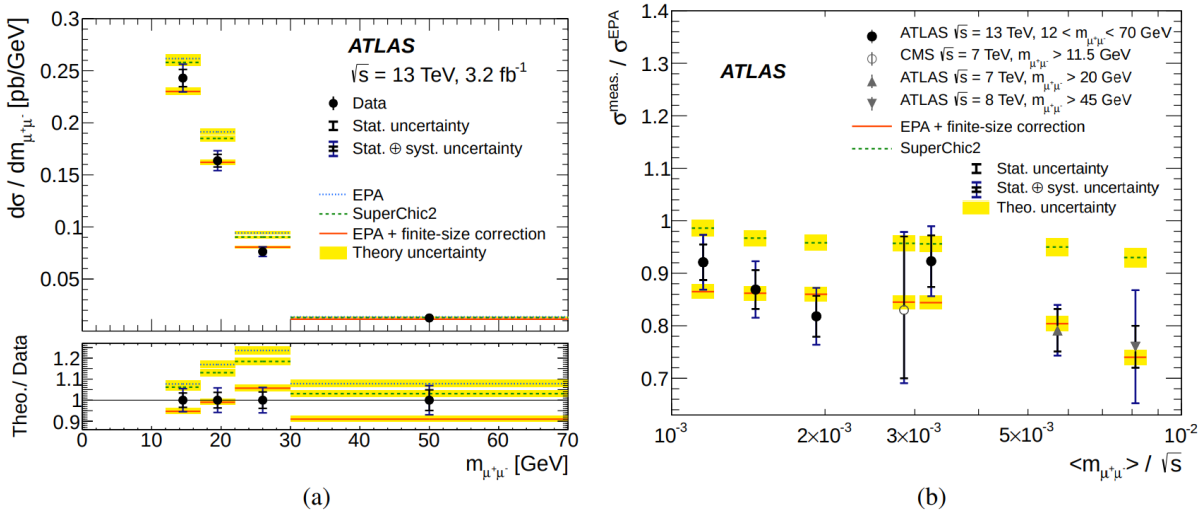

Figure 2.6: The exclusive $\gamma\gamma \to \mu^+\mu^-$ differential fiducial cross-section measurements as a function of dimuon invariant mass. (b) Comparison of the ratios of measured and predicted cross-sections to the bare EPA calculations as a function of the average dimuon invariant mass scaled to the *pp* center-of-mass energy used. Data (markers) are compared to various predictions (lines). Full circle markers represent the four mass points presented in [35], while open circle, up-triangle and down-triangle depict the previous results obtained with $m_{\mu^+\mu^-} > 11.5\,\text{GeV}$, $m_{\mu^+\mu^-} > 20\,\text{GeV}$ and $m_{\mu^+\mu^-} > 45\,\text{GeV}$ requirements on the dimuon invariant mass. The inner error bars represent the statistical uncertainties, and the outer bars represent the total uncertainty in each measurement. The yellow bands represent the theoretical uncertainty in the predictions. The bottom panel in (a) shows the ratio of the predictions to the data [35].

In addition, several questions in particle physics rely in the research of two-photon interactions, *e.g.*, light-by-light scattering processes ($\gamma\gamma \to \gamma\gamma$) provides a prompt experimental probe of Standard Model gauge couplings [38], extra dimensions [39, 40] and graviton search [41]. Even a search for SUSY particles can be performed in two-photon production data [42]. Further confirmation of Higgs boson can be established in a clean exclusive photo-production process [43, 44]. Finally, tests of QED are realized by measuring the cross-sections of leptons and bosons pairs.

2.3 Photonuclear production in PbPb collisions

In this work, a data analysis of gamma-nucleus coherent J/ψ production is performed using lead ions collisions. In this context, coherent means that the photon emitted by

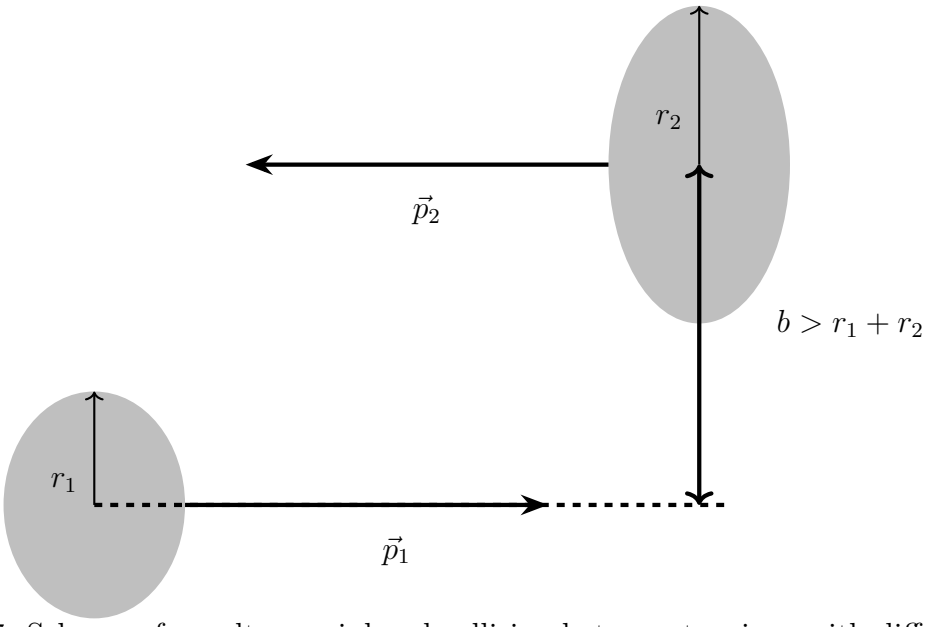

Figure 2.7: Scheme of an ultra-peripheral collision between two ions with different radii.

the source nucleus interacts with the target nucleus as a whole. Therefore, both nuclei remain intacts after collision. This type of interaction is more likely to happen in **U**ltra-**P**eripheral **C**ollisions (UPC). UPC occur when two nuclei interact with a distance between their center, defined as impact parameter, greater than the sum $r_1 + r_2$ of their radii, see Figure 2.7. In this type of collision the interaction is carried out by the cloud of virtual photons surrounding the nuclei.

The **E**quivalent **P**hoton **A**pproximation method was firstly proposed by Enrico Fermi in 1924 [45]. The main proposal of this method is to describe the electromagnetic field of a moving charged particle as a cloud of quasi-real photons. Using this archetype a full description of protons or ions collisions can be achieved simply by means of photon densities. It facilitates the theoretical description of pure electromagnetic processes. In particular, years later, Weizsaker and Williams introduced the EPA concept in the treatment of relativistic ions [46]. The intensity of the electromagnetic field, and therefore the number of photons in the cloud surrounding the nucleus, is proportional to Z^2, where Z is the number of protons found in the nucleus. Thus these types of interactions are highly favored when heavy ions collide.

The cross-section of the photoproduction of a particle X in a heavy ions UPC is determined by the equation

$$\sigma_{AA\to A+X+A} = 2\int dk \frac{dN_\gamma^Z(k)}{dk}\sigma_{\gamma A\to X}(k) \tag{2.6}$$

where $\frac{dN_\gamma^Z(k)}{dk}$ is the flux of photons with energy k in the rest frame of the target nucleus, determined as the Fourier transform of the electromagnetic field of the source ion and $\sigma_{\gamma A\to X}(k)$ is the photonuclear cross-section. In this case, the photoproduction cross-section must be multiplied by a factor 2 in order to account for the symmetry of source and target in identical ions collision.

The photon flux of the source nucleus is given by [47, 48]:

$$\frac{dN_\gamma^Z(k)}{dk} = \frac{2Z^2\alpha_{em}}{k\pi}\left\{\xi K_0(\xi)K_1(\xi) - \frac{\xi^2}{2}\left[K_1^2(\xi) - K_0^2(\xi)\right]\right\} \tag{2.7}$$

where $\xi \equiv k(r_1 + r_2)/(2\gamma_L^2)$ is the reduced adiabacity parameter, K_0 and K_1 are the modified Bessel functions and γ_L is the Lorentz factor of the source ion in the target ion frame. The photon flux determined by this formula is represented in Figure 2.8 for three different accelerators. In the LHC the cross-section of this type of process is favored by the larger reachable values of photon flux.

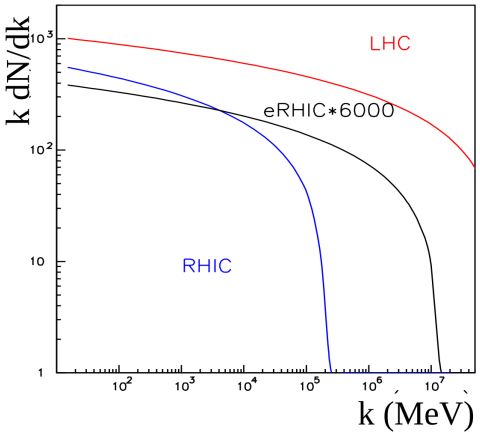

Figure 2.8: The photon flux from $\sqrt{s_{NN}} = 5.5\,\text{TeV}$ Pb-Pb collisions at LHC in comparison with the photon fluxes of Au-Au collisions at RHIC with $\sqrt{s_{NN}} = 200\,\text{GeV}$ and $10\,\text{GeV} + 100\,\text{GeV}$ e-Au collisions at the eRHIC multiplied by 6000 to account for improved gold beam parameters. k is given in the rest frame of the target nucleus in all three cases [49].

The virtual photon from the source ion can interact coherently with all nucleons of the target ion or it can interact directly with one of the nucleons of the target ion. In the former case, the photonuclear process is showed in the diagram of Figure 2.9a. In this diagram both nuclei remain intacts after the collision and it is called a *coherent* production. In the case of an interaction with one of the nucleus of the target ion, the breakup of the target ion may occur as illustrated in Figure 2.9b where A' correspond to the fragments of the target ion. This case is called an *incoherent* production.

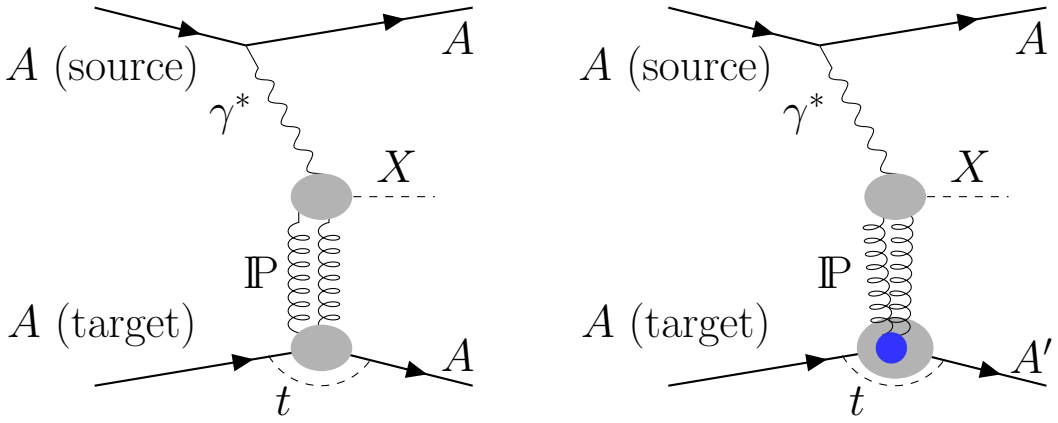

(a) Coherent production (b) Incoherent production

Figure 2.9: Diffractive photonuclear production of X in A-A collisions. In diagram (a) the photon interacts with the full nucleus A, while in (b) it scatters off one of the nucleons in A. Accordingly these processes are called coherent and incoherent X production, respectively.

Considering the coherent production of the J/ψ vector meson in UPCs, the photonuclear cross-section is written as:

$$\sigma_{\gamma A\to J/\psi A}(k) = \left.\frac{d\sigma_{\gamma A\to J/\psi A}}{dt}\right|_{t=0} \int dt|F(t)|^2 \tag{2.8}$$

where $F(t)$ is the nuclear form factor, t is the squared momentum transfer and $d\sigma_{\gamma A\to J/\psi A}/dt|_{t=0}$ is the cross-section of forward scattering.

In Reference [50] the cross-section of forward scattering for the production of vector mesons is deduced within the double logarithmic approximation and is given by

$$\left.\frac{d\sigma_{\gamma A\to J/\psi A}}{dt}\right|_{t=0} \propto \frac{1}{[m(J/\psi)]^5}[xg_A(x,Q^2)]^2 \tag{2.9}$$

where $g_A(x, Q^2)$ is the nuclear gluon distribution, $x = [m_(J/\psi)/s]e^{\pm y}$ is the Bjorken variable, $m(J/\psi) = (3096.916 \pm 0.011)\,\mathrm{MeV}/c^2$ [2], y is the rapidity of J/ψ, $Q^2 = -q^2$ is the photon virtuality where q is the four-momentum transfer.

There are several theoretical predictions available for the vector meson production in PbPb UPCs [51, 52, 53, 54, 55, 56]. Each model has a proper way to describe the photonuclear interaction.

In the model by Gonçalves et al [56], the J/ψ-proton cross-section is calculated within the framework of the Colour-Dipole model. Three different parametrisations of the dipole-proton cross-section (IIM, IP-SAT, bCGC), based on saturation physics, are combined with two different models of vector meson wave functions, namely boosted Gaussian (BG) and Gauss-LC (GLC) wave functions. All the parameters are tuned using the latest HERA data.

The model from Cepila et al. [54] can be seen as a variation of the Color Dipole model. The main differences with respect to [56] come from the parametrisation of the dipole-proton cross-section and the prescription used to propagate it to the dipole-nucleus scattering amplitudes, namely the Glauber-Gribov methodology (GG) or a geometric scaling between the nuclear saturation scale and the saturation scale in the proton (GS). Two models for the nuclear profile are explored, one where the nucleus are made up of nucleons and the other that includes subnucleonic degrees of freedom in the form of hot spots (hs).

In the model proposed by Möntysaari et al. [55], the cross-section is also calculated using the Colour-Dipole model including subnucleon scale fluctuations. Predictions with and without subnucleonic fluctuations using the IP-SAT parametrisation for the dipole proton cross-section and the GLC for the vector-meson wave function are available.

The model provided by Guzey et al. [51] is based on perturbative QCD (pQCD) calculation. The exclusive J/ψ photoproduction cross-section on a proton target is calculated at leading order pQCD within the leading log approximation. Several prescriptions for the

nuclear shadowing effect are then used to compute the final cross-section: weaker (LTA_W) and a stronger (LTA_S) scenarios using leading twist nuclear shadowing model [57], and EPS09 [58] nPDFs.

Two previous measurements of the differential cross-section of J/ψ coherent production in PbPb UPC are available through the ALICE collaboration [12, 59]. The result obtained by ALICE with $\sqrt{s_{NN}} = 5.02\,\text{TeV}$ center-of-mass energy data is presented in Figure 2.10 accompanied of some theoretical predictions. The rapidity coverage of ALICE is 1 unity smaller than the LHCb coverage.

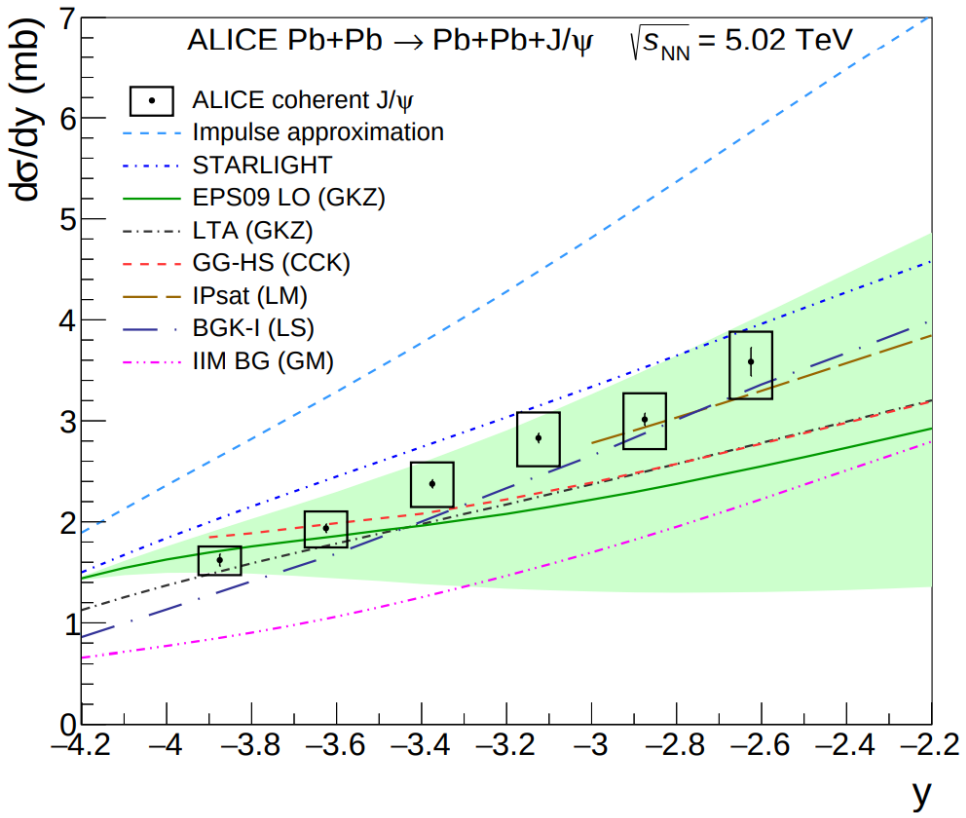

Figure 2.10: Measured coherent differential cross section of J/ψ photoproduction in ultra-peripheral PbPb collisions at $\sqrt{s_{\text{NN}}} = 5.02\,\text{TeV}$. The error bars represent the statistical uncertainties, the boxes around the points the systematic uncertainties [59].

The measurement of the coherent cross-section of $\gamma A \to J/\psi A$ provides not only a constraint to the nuclear gluon distribution at the x and Q^2 range given by the experi-

ment, but also to its relation to the proton gluon distribution, allowing us to extract the modification of the gluon distribution from the proton to the more complex system of the nucleus. Particularly, the coherent production shows a clean scenario to measure the cross-sections and improve theoretical progress enabled by the comparison with data. In addition it is the first measurement making use of PbPb collisions in LHCb. It shows how broad the physics programme of this experiment is. In this context, the work presented in Chapter 5 is to describe the results from [60] in details and reports an extension of this analysis using a high-rapidity detector recently installed in LHCb. An updated cross-section measurement is then presented and compared to the models described here.

Chapter 3

LHC machine and LHCb detector

The experimental apparatus used to acquire the data is described in references [61, 62]. This chapter presents a transcript of excerpts from these references that are the most relevant for the CEP analyses which are the subject of this thesis.

3.1 Large Hadron Collider

LHC is currently the larger particle accelerator operating in the world. The host of LHC is the *Organisation Européenne pour la Recherche Nucléaire* (CERN) at the french-swiss border. The accelerator is an almost circular 27-km perimeter ring. It is located within a tunnel in the underground of Geneva suburbs.

LHC supports both protons or ions collisions. The machine was originally designed to carry out proton collisions with proton-proton centre of mass energy of 14 TeV and with a luminosity of $L = 10^{34}\,\mathrm{cm}^{-2}\mathrm{s}^{-1}$. To achieve such a luminosity, the accelerator would be filled with two beams, both with 2808 bunches with around 1.1×10^{11} protons each. With this configuration it would provide a bunch crossing every 25 ns.

During 2010 and 2011 data-taking epochs the center-of-mass energy was set to a lower value of 7 TeV for machine sustainability and development reasons. It was then pushed up to 8 TeV in 2012, to achieve a peak energy of 13 TeV after the first long shut-down in 2013-2014.

Along with the proton-proton collisions, two other operating modes are also made available for the LHC, as lead ions ($Z = 82$) can also be accelerated using a slightly different chain of injectors. This enables the access to a larger spectrum of studies probing lead-lead collisions or asymmetric proton-lead collisions.

Beams must have an initial energy of 450 GeV in order to be accelerated in LHC. For this purpose, a pre-acceleration system is used. Protons, acquired from hydrogen atoms, go through a linear accelerator (LINAC 2), where they achieve an energy of 50 MeV. Beams of such protons are inserted in the Proton Syncrotron Booster (PSB), reaching the energy of 1.4 GeV at the output. These beams are sent to the Proton Syncrotron (PS) and accelerated up to the energy of 25 GeV. The last stage before LHC is the Super Proton Syncrotron (SPS) where the beams acquire enough energy to be inserted at the LHC.

Two beam pipes are present inside the LHC, they are kept in high level vacuum and at the temperature of $-271°$C. The acceleration is provided by superconducting magnets: 1232 magnetic dipoles are responsible for driving the beam and 329 magnetic quadrupoles are responsible for the beam focusing. The beams can be bent to collide at four points where the main experiments are installed: ATLAS, CMS, ALICE and LHCb. A schematic view of LHC and its experiments is in the Figure 3.1.

A **T**oroidal **L**HC **A**pparatu**S** (ATLAS) [63] and **C**ompact **M**uon **S**olenoid (CMS) [64] are general-purpose experiments studying proton-proton collisions and the proton-lead and lead-lead collisions as well. **A** **L**arge **I**on **C**olliding **E**xperiment (ALICE) [65] is dedicated to study the quark-gluon plasma states created at the collision of heavy ions. The **L**arge **H**adron **C**ollider **b**eauty experiment (LHCb) [61] studies are focused in the b quark phenomenology using high-precision flavour physics to search and study matter-antimatter asymmetry. LHCb was used to acquire the data used in this work and will be further detailed in the following section.

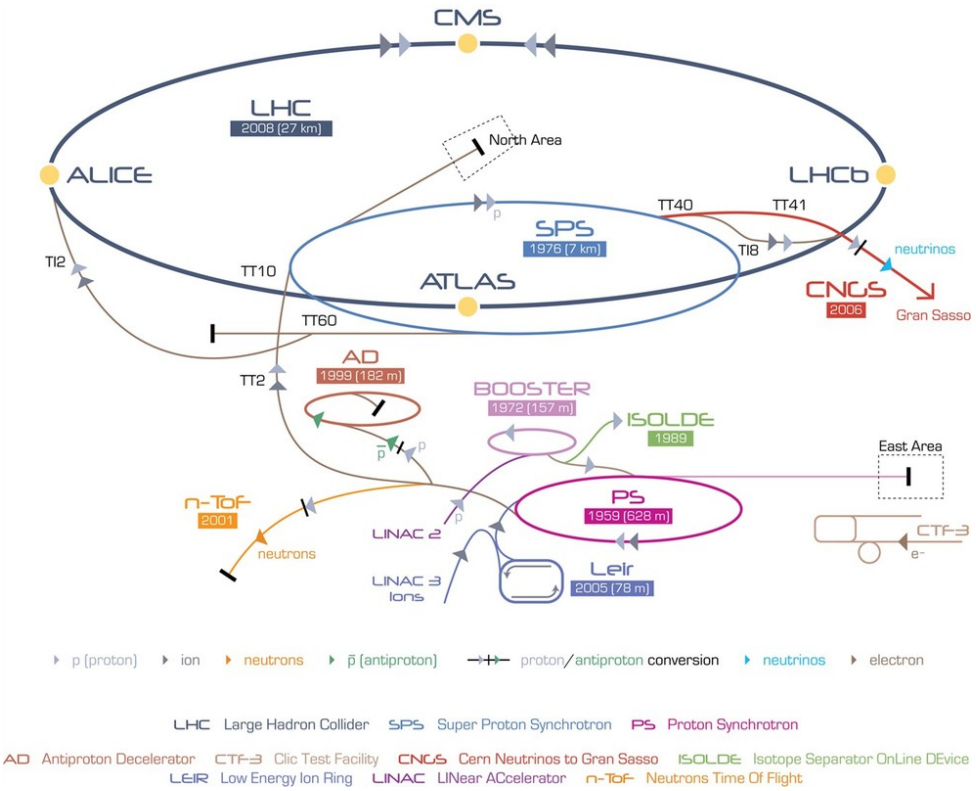

Figure 3.1: Schematic view of the LHC and its experiments. The LHCb experiment lies on the right side of this figure, at LHC's "Point 8" [66].

3.2 LHCb detector

The LHCb experiment has been conceived to study CP-violation and other rare phenomena in B meson decays with very high precision. This should provide a profound understanding of quark flavour physics in the framework of the Standard Model, and may reveal a sign of the physics beyond.

LHCb is a single-arm spectrometer with a forward angular coverage from approximately 10 mrad to 300 mrad (250 mrad) in the bending (non-bending) plane. The choice of the detector geometry is motivated by the fact that at high energies both the b- and $\bar{b}$-hadrons are predominantly produced in the same forward cone, a feature exploited in the flavour tag. This is demonstrated in Figure 3.2, where the polar angles of the b- and $\bar{b}$-hadrons calculated by the PYTHIA event generator [67, 68] are shown. The polar angle

is defined with respect to the beam axis in the proton-proton center-of-mass system.

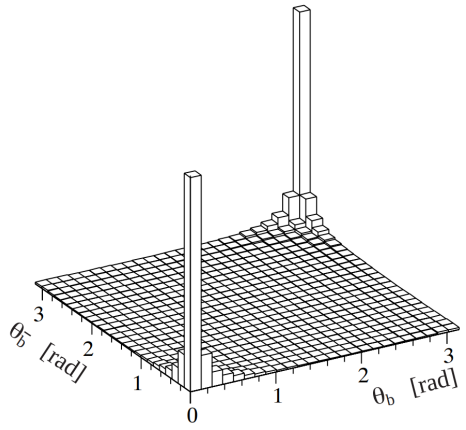

Figure 3.2: Polar angles of the b- and $\bar{b}$-hadrons calculated by the PYTHIA event generator [69].

The layout of the LHCb spectrometer is shown in Figure 3.3. A right-handed coordinate system is defined with its origin at the interaction point, with z along the beam axis pointing to right and y pointing upwards. LHCb comprises a vertex detector system (including a pile-up veto counter), a tracking system (partially inside a dipole magnet), aerogel and gas RICH counters, an electromagnetic calorimeter with preshower detector, a hadron calorimeter and a muon detector. All detector subsystems, except the vertex detector, are assembled in two halves, which can be separated horizontally for assembly and maintenance, as well as to provide access to the beam pipe.

A last subdetector was added during the first long shut-down (2013-2014). The HeRSCheL (**H**igh-**R**apidity **S**hower **C**ounters for **L**HCb) consists of a set of scintillating counters, designed to increase the coverage of the LHCb experiment in the high-rapidity regions on either side of the main spectrometer. This detector improves the capabilities of LHCb for studies of diffractive interactions, most notably Central Exclusive Production. It is descibed in detail in [70], and a selection of its content is presented in Section 3.2.9.

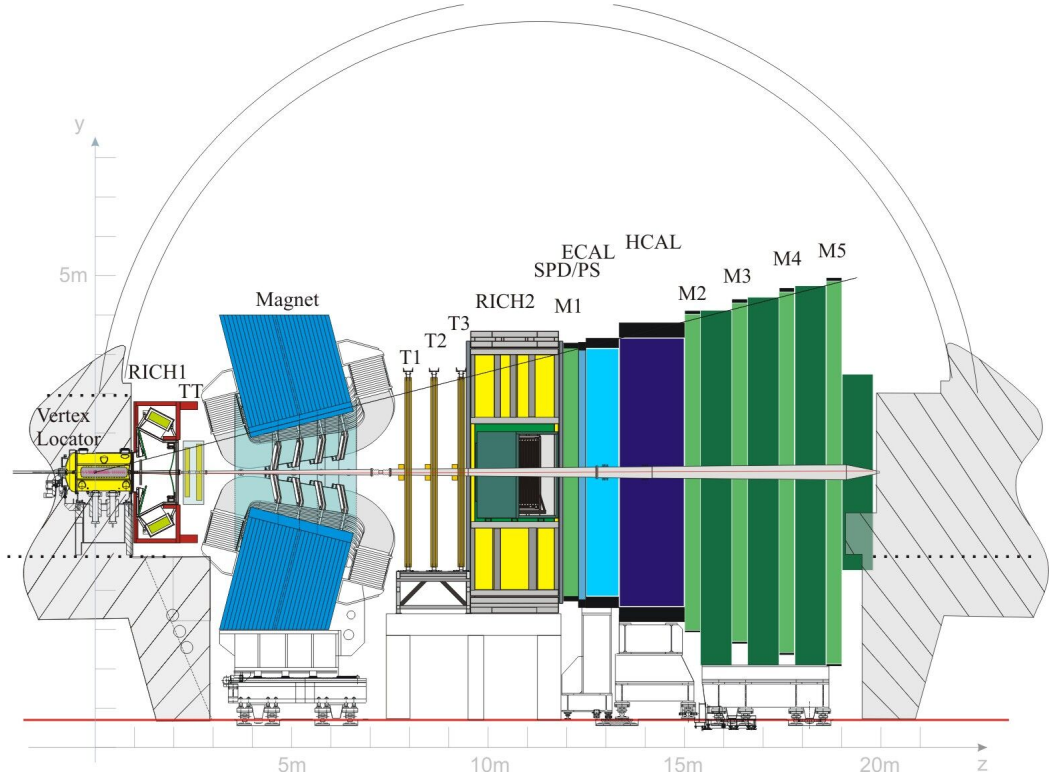

Figure 3.3: Schematic view of LHCb experiment and its subdetectors. The HeRSCheL detector is not present in this figure [61].

3.2.1 Vertex detector system

The LHCb **VE**rtex **LO**cator (VELO) is a silicon microstrip detector positioned around the interaction region. The VELO provides precise measurements of track coordinates which are used to identify the primary interaction vertices and the secondary vertices which are a distinctive feature of b- and c-hadrons decays, e.g. the $J/\psi \to \mu^+\mu^-$ meson decays. The VELO was designed to optmise the LHCb physics programme adopting the following aspects (among others):

- **Angular coverage.** The VELO is designed to cover the forward region, such that all tracks inside the nominal LHCb acceptance of 15-300 mrad cross at least three VELO stations. In this way the detector fully reconstructs roughly 27% of $b\bar{b}$ production for 7 TeV proton-proton center-of-mass collisions, while covering just 1.8% of the solid angle. The VELO also reconstructs tracks in the forward and

backward directions which do not have momentum information, but are useful to improve the primary vertex reconstruction and to select exclusive events.

- **Triggering.** The reconstruction of the primary vertex and the displaced secondary decay vertex of a heavy flavour hadron in the VELO is a key ingredient of the high level trigger which reduces the event rate from 1 MHz to a few kHz.

The VELO contains a series of silicon modules arranged along the beam direction, as shown in Figure 3.4. The region of the detector at positive (negative) z values is known as the forward (backward) or downstream (upstream) end. The sensors are positioned only 7 mm from the LHC beams. This is smaller than the aperture required by the LHC beam during injection. Hence, the detector is produced in two retractable halves. There is a small overlap between the two detector halves when closed. This aids alignment and ensures that full angular coverage is maintained. The position of the VELO halves are moveable in x and y and the VELO is closed at the beginning of each fill such that it is centred on the interaction region.

Approximately semi-circular silicon sensors are used. Each module contains one r and one ϕ coordinate measuring sensor, known as R and Φ sensors. The inter-strip pitch varies from approximately 40 to 100 μm across the sensor. The strips are read out from around the circumference of the sensor through the use of routing lines on the sensor. There are 21 standard modules in each VELO half. Two further modules, known as the pile-up system, containing R sensors only are located in the most upstream positions.

The VELO is very important for CEP analyses considering *i*) the veto of fake exclusive events with backward tracks and *ii*) the precise measurement of primary interactions which helps to ensure that a true exclusive event occurred even when there is more than one primary interaction.

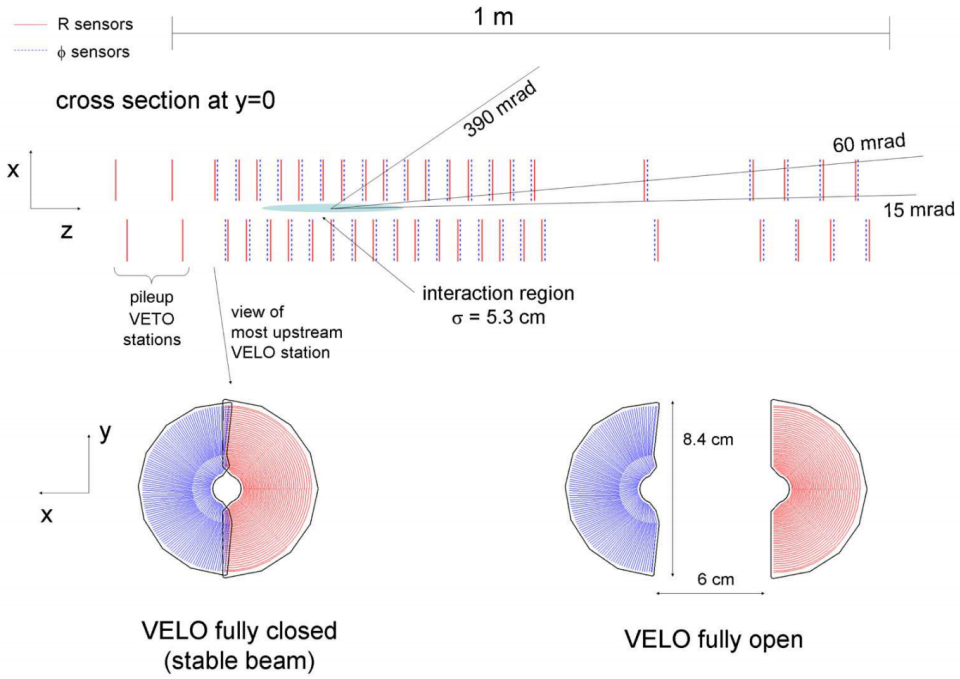

Figure 3.4: Cross-section in the (x,z) plane of the VELO silicon sensors, at $y = 0$, with the detector in the fully closed position (top). In both the closed and open positions the front face of the first modules is also illustrated (bottom). The two pile-up veto stations are located upstream of the VELO sensors [61].

3.2.2 Magnet

A dipole magnet is used in the LHCb experiment to measure the momentum of charged particles. It is a warm magnet design with saddle-shaped coils in a window-frame yoke with sloping poles in order to match the required detector acceptance. The design of the magnet with an integrated magnetic field of 4 Tm for tracks of 10 m length had to accommodate the contrasting needs for a field level inside the RICHs envelope less than 2 mT and a field as high as possible in the regions between the vertex locator and the Trigger Tracker tracking station. The design was also driven by the boundary conditions in the experimental hall previously occupied by the DELPHI detector. This implied that the magnet had to be assembled in a temporary position and to be subdivided into two relatively light elements. The DELPHI rail systems and parts of the magnet carriages have been reused as the platform for the LHCb magnet for economic reasons. Plates, 100 mm

thick, of laminated low carbon steel, having a maximum weight of 25 tons, were used to form the identical horizontal bottom and top parts and the two mirror-symmetrical vertical parts (uprights) of the magnet yoke. The total weight of the yoke is 1500 tons and of the two coils is 54 tons.

Each coil consists of fifteen pancakes arranged in five triplets and produced of pure Aluminum hollow conductor in an annealed state which has a central cooling channel of 25 mm diameter. The coils were produced in industry with some equipment and technical support from CERN. Cast Aluminum clamps are used to hold together the triplets making up the coils, and to support and centre the coils with respect to the measured mechanical axis of the iron poles with tolerances of several millimeters. As the main stress on the conductor is of thermal origin, the design choice was to leave the pancakes of the coils free to slide upon their supports, with only one coil extremity kept fixed on the symmetry axis, against the iron yoke, where electrical and hydraulic terminations are located. After rolling the magnet into its nominal position, final precise alignment of the yoke was carried out in order to follow the 3.6 mrad slope of the LHC machine and its beam. The resolution of the alignment measurements was about 0.2 mm while the magnet could be aligned to its nominal position with a precision of ± 2 mm. A perspective view of the magnet is given in Figure 3.5. The magnet is operated via the Magnet Control System that controls the power supply and monitors a number of operational parameters (e.g. temperatures, voltages, water flow, mechanical movements, etc.). A second, fully independent system, the Magnet Safety System (MSS), ensures the safe operation and acts autonomously by enforcing a discharge of the magnet if critical parameters are outside the operating range. Several magnetic field measurement campaigns have been carried out during which the magnet has shown stable and reliable performance.

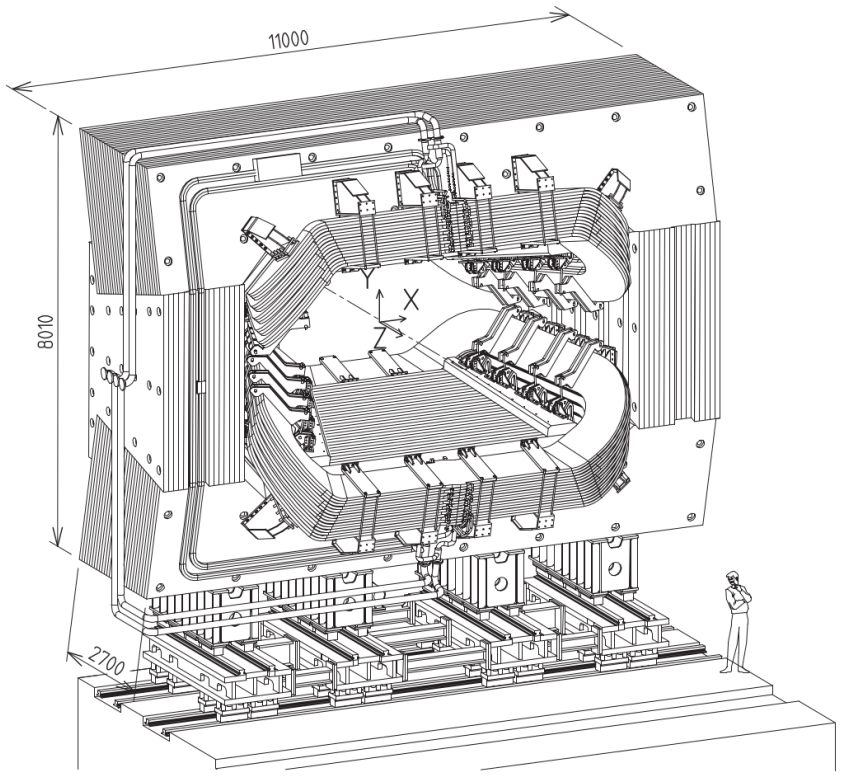

Figure 3.5: Perspective view of the LHCb dipole magnet with its current and water connections (units in mm). The interaction point lies behind the magnet [61].

Field mapping

In order to achieve the required momentum resolution for charged particles, the magnetic field integral $\int B\mathrm{d}\ell$ must be measured with a relative precision of a few times 10^{-4} and the position of the B-field peak with a precision of a few millimetres. A semi-automatic measuring device was constructed which allowed remotely controlled scanning along the longitudinal axis of the dipole by means of an array of Hall probes. The measuring machine was aligned with a precision of 1 mm with respect to the experiment reference frame. The support carrying the Hall probes could be manually positioned in the horizontal and vertical direction such as to cover the magnetic field volume of interest. The calibration process allowed correcting for non-linearity, temperature dependence and non-orthogonal mounting of the Hall probes. The goal of the field mapping campaigns was to measure the three components of the magnetic field inside the tracking volume of

the detector for both magnet polarities and to compare it to the magnetic field calculations obtained with software. For the measurement of CP asymmetries it is important to control the systematic effects of the detector, by changing periodically the direction of the magnetic field. The magnetic field has been measured in the complete tracking volume inside the magnet and in the region of the VELO and the tracking stations, and also inside the magnetic shielding for the RICH1 and RICH2 photon detectors. The precision of the measurement obtained for the field mapping in the tracking volume is about 4×10^{-4}. The main component, B_y, is shown in Figure 3.6 for both polarities, together with the result of the model calculation. The overall agreement is excellent; however, in the upstream region of the detector (VELO, RICH1) a discrepancy of about 3.5% for the field integral has been found which can be attributed both to the precision of the software model and to the vicinity of the massive iron reinforcement embedded in the concrete of the hall. In all other regions the agreement between measurement and calculation is better than 1%.

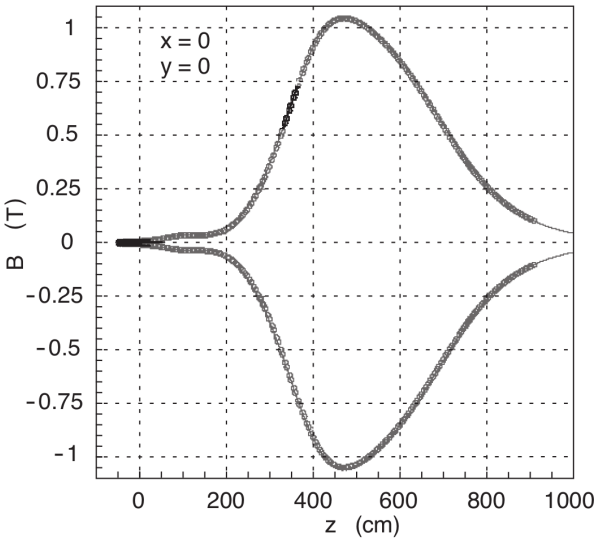

Figure 3.6: Magnetic field along the z axis [61].

3.2.3 Tracking system

LHCb tracking system comprises three subsystems: VELO, silicon tracker and the outer tracker. These systems are different in layout, location and technology as well. The main

purpose of this system is to reconstruct digitally the tracks of charged particles using the hits of the particles on the detectors.

Silicon tracker

The Silicon Tracker (ST) comprises two detectors: the Tracker Turicensis 10 (TT) and the Inner Tracker (IT). Both TT and IT use silicon microstrip sensors with a strip pitch of about 200 μm. The TT is a 150 cm wide and 130 cm high planar tracking station that is located upstream of the LHCb dipole magnet and covers the full acceptance of the experiment. The IT covers a 120 cm wide and 40 cm high cross shaped region in the centre of the three tracking stations downstream of the magnet. Each of the four ST stations has four detection layers in an $(x-u-v-x)$ arrangement with vertical strips in the first and the last layer and strips rotated by a stereo angle of -5° and $+5^\circ$ in the second and the third layer, respectively. The TT has an active area of about 8.4 m^2 with 143,360 readout strips of up to 38 cm in length. The IT has an active area of 4.0 m^2 with 129,024 readout strips of either 11 cm or 22 cm in length.

Different constraints on the detector geometries resulted in different designs for the detector modules and station mechanics of the TT and the IT. Common to both parts of the ST are the readout electronics, the power distribution, and the detector control and monitor systems.

All four detection layers of the TT are housed in one large light tight and thermally and electrically insulated detector volume, in which a temperature below 5°C is maintained. The detector volume is continuously flushed with nitrogen to avoid condensation on the cold surfaces. To aid track reconstruction algorithms, the four detection layers are arranged in two pairs, (x,u) and (v,x), that are separated by approximately 27 cm along the LHC beam axis.

The layout of one of the detection layers is illustrated in Figure 3.7. Its basic building block is a half module that covers half the height of the LHCb acceptance. It consists of a row of seven silicon sensors organized into either two or three readout sectors. The readout

hybrids for all readout sectors are mounted at one end of the module. The regions above and below the LHC beam pipe are covered by one such half module each. The regions to the sides of the beam pipe are covered by rows of seven (for the first two detection layers) or eight (for the last two detection layers) 14-sensor long full modules. These full modules cover the full height of the LHCb acceptance and are assembled from two half modules that are joined together end-to-end. Adjacent modules within a detection layer are staggered by about 1 cm in z and overlap by a few millimeters in x to avoid acceptance gaps and to facilitate the relative alignment of the modules. In the u and v detection layers, each module is individually rotated by the respective stereo angle.

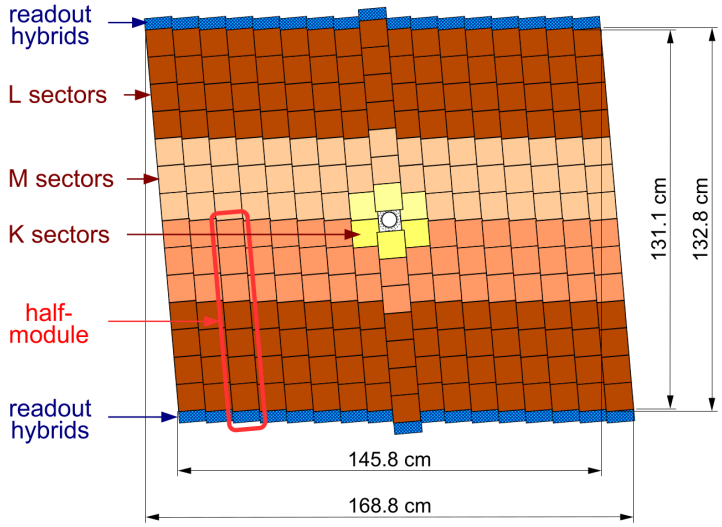

Figure 3.7: Layout of the third TT detection layer. Different readout sectors are indicated by different shadings [61].

A main advantage of this detector design is that all front-end hybrids and the infrastructure for cooling and module supports are located above and below the active area of the detector, outside of the acceptance of the experiment.

The layout of a half module is illustrated in Figure 3.8. It consists of a row of seven silicon sensors with a stack of two or three readout hybrids at one end. For half modules close to the beampipe, where the expected particle density is higher, the seven sensors are organized into three readout sectors (4-2-1 type half modules). For the other half

modules, the sensors are organized into two readout sectors (4-3 type half modules).

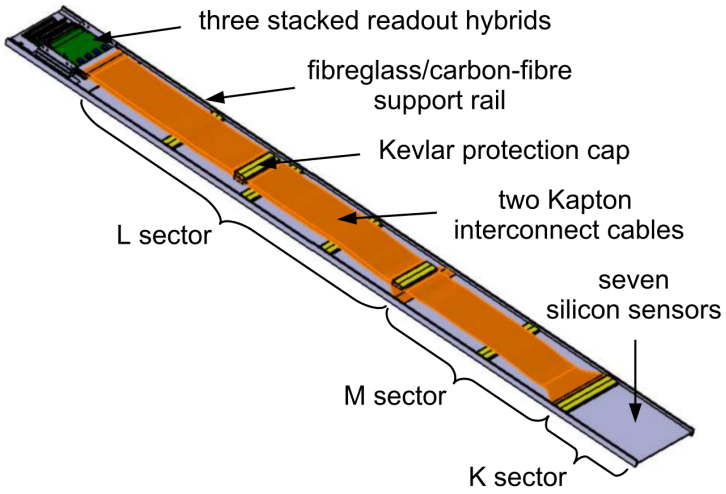

Figure 3.8: View of a 4-2-1 type TT detector module [61].

Inner tracker

Each of the three IT stations consists of four individual detector boxes that are arranged around the beampipe as shown in Figure 3.9. The detector boxes are light tight and electrically and thermally insulated, and a temperature below 5°C is maintained inside them. They are continuously flushed with nitrogen to avoid condensation on the cold surfaces. Each detector box contains four detection layers and each detection layer consists of seven detector modules. Adjacent modules in a detection layer are staggered by 4 mm in z and overlap by 3 mm in x to avoid acceptance gaps and facilitate the relative alignment of the modules. Detector modules in the boxes above and below the beampipe (top and bottom boxes) consist of a single silicon sensor and a readout hybrid. Detector modules in the boxes to the left and right of the beampipe (side boxes) consist of two silicon sensors and a readout hybrid. The resulting layout and dimensions of one of the IT detection layers are illustrated in Figure 3.10.

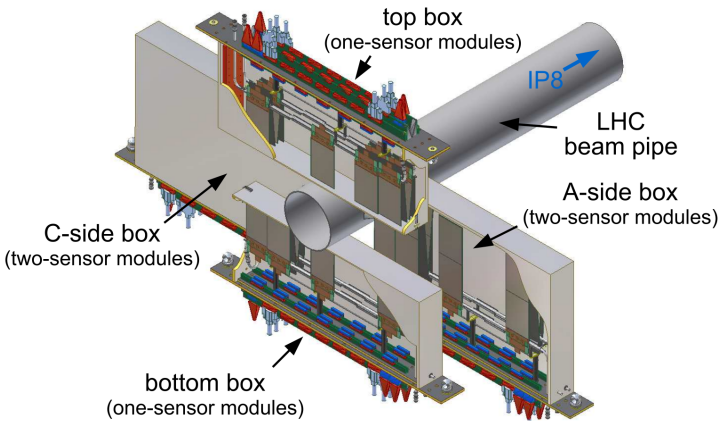

Figure 3.9: View of the four IT detector boxes arranged around the LHC beampipe [61].

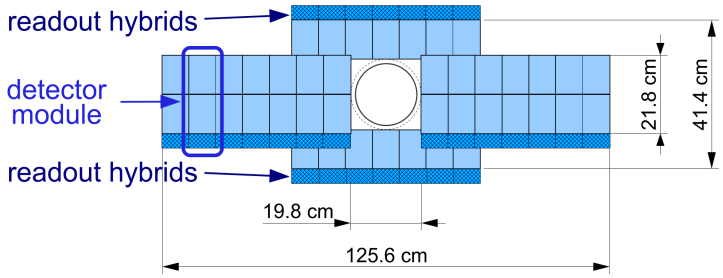

Figure 3.10: Layout of an x detection layer in the second IT station [61].

An exploded view of a detector module is shown in Figure 3.11. The module consists of either one or two silicon sensors that are connected via a pitch adapter to a front-end readout hybrid. The sensor(s) and the readout hybrid are all glued onto a flat module support plate.

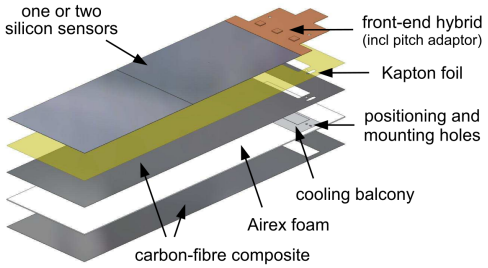

Figure 3.11: Exploded view of a two-sensor IT module. One-sensor modules are similar except that the support plate is shorter and carries only one sensor [61].

Outer tracker

The LHCb Outer Tracker (OT) is a drift-time detector, for the tracking of charged particles and the measurement of their momentum over a large acceptance area. Excellent momentum resolution is necessary for a precise determination of the invariant mass of the reconstructed b-hadrons: a mass resolution of $10\,\mathrm{MeV}/c^2$ for the decay $B_s^0 \to D_s^- \pi^+$ translates into a required momentum resolution of $\delta p/p \approx 0.4\%$. The reconstruction of high multiplicity B decays demands a high tracking efficiency and at the same time a low fraction of wrongly reconstructed tracks: a track efficiency of 95% would result, for the decay $B_s^0 \to D_s^- \pi^+$, in an overall reconstruction efficiency of 80%.

The detector modules are arranged in three stations, see Figure 3.12. Each station consists of four layers, arranged in an $x-u-v-x$ geometry: the modules in the x-layers are oriented vertically, whereas those in the u and v layers are tilted by $\pm 5^\circ$ with respect to the vertical, respectively. The total active area of a station is $5971 \times 4850\,\mathrm{mm}^2$. The outer boundary corresponds to an acceptance of $300z$, mrad in the magnet bending plane (horizontal) and 250 mrad in the non-bending plane (vertical).

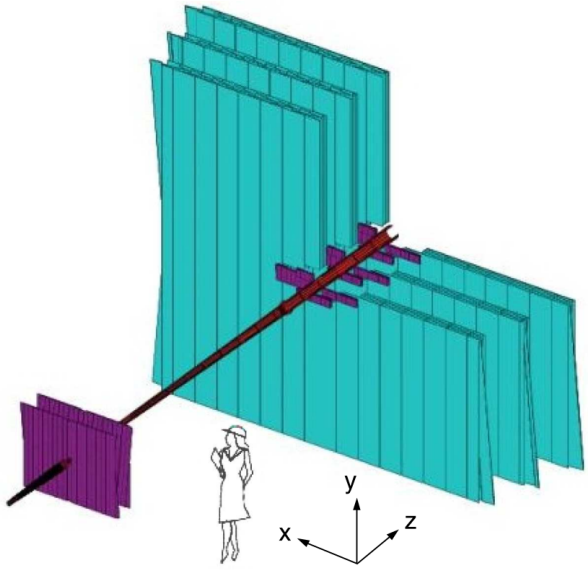

Figure 3.12: Arrangement of OT straw-tube modules in layers and stations (green) [61].

The layout of the straw-tube modules is shown in Figure 3.13. The modules are composed of two staggered layers (monolayers) of 64 drift tubes each. In the longest modules (type F) the monolayers are split longitudinally in the middle into two sections composed of individual straw tubes. Both sections are read out from the outer end. The splitting in two sections is done at a different position for the two monolayers to avoid insensitive regions in the middle of the module. F-modules have an active length of 4850 mm and contain a total of 256 straws. In addition to the F-type modules there exist short modules (type S) which are located above and below the beam pipe. These modules have about half the length of F-type modules, contain 128 single drift tubes, and are read out only from the outer module end. A layer half is built from 7 long and 4 short modules. The complete OT detector consists of 168 long and 96 short modules and comprises about 55000 single straw-tube channels.

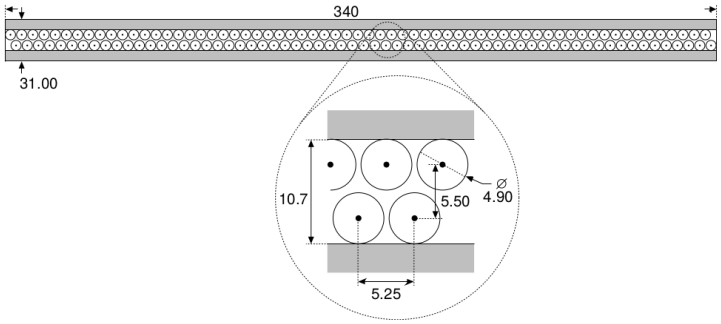

Figure 3.13: Cross-section of a straw-tubes module [61].

The tracking efficiency is defined as the probability that the trajectory of a charged particle that has passed through the full tracking system is reconstructed. In particular it does not account for interactions with the material, decays in flight and particles that fly outside of the detector acceptance. The average tracking efficiency is measured from tag-and-probe method using $J/\psi \to \mu^+\mu^-$ decays and found to be around 96% in the momentum range $5 < p < 200\,\mathrm{GeV}/c$ and in the pseudorapidity range $2 < \eta < 5$, which covers the phase space of LHCb [62].

3.2.4 Particle identification

Particle identification (PID) is a fundamental requirement for LHCb. It is essential for the goals of the experiment to separate pions from kaons in selected B hadron decays. At large polar angles the momentum spectrum is softer while at small polar angles the momentum spectrum is harder; hence the particle identification system consistes of two RICH detectors to cover the full momentum range. The upstream detector, RICH 1, covers the low momentum charged particle range $\approx$ 1–60 GeV/c using aerogel and C_4F_{10} radiators, while the downstream detector, RICH 2, covers the high momentum range from $\approx$ 15GeV/c up to and beyond 100 GeV/c using a CF_4 radiator, see Figure 3.14. RICH 1 has a wide acceptance covering the full LHCb acceptance from $\pm$25 mrad to $\pm$300 mrad (horizontal) and $\pm$250 mrad (vertical) and is located upstream of the magnet to detect the low momentum particles. RICH 2 is located downstream of the magnet and has a limited angular acceptance of $\approx \pm$15 mrad to $\pm$120 mrad (horizontal) and $\pm$100 mrad (vertical) but covers the region where high momentum particles are produced. In both RICH detectors the focusing of the Cherenkov light is accomplished using a combination of spherical and flat mirrors to reflect the image out of the spectrometer acceptance. In the RICH 1 the optical layout is vertical whereas in RICH 2 is horizontal. Hybrid Photon Detectors (HPDs) are used to detect the Cherenkov photons in the wavelength range 200–600 nm. The HPDs are surrounded by external iron shields and are placed in cylinders of a nickel-iron ferromagnetic alloy to permit operation in magnetic fields up to 50 mT. A schematic view of RICH 1 (RICH 2) is showed in Figure 3.15 (Figure 3.16).

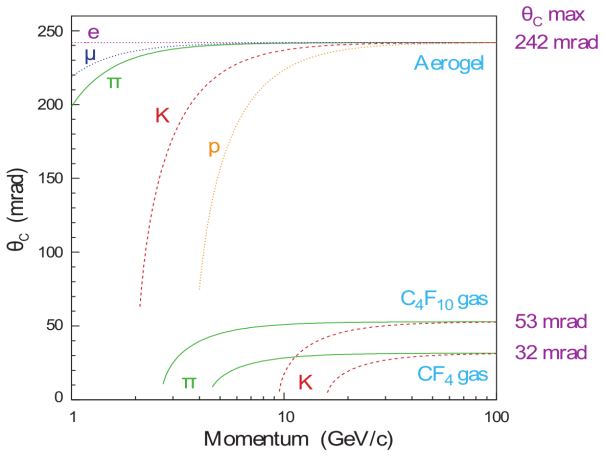

Figure 3.14: Cherenkov angle versus particle momentum for the RICH radiators [61].

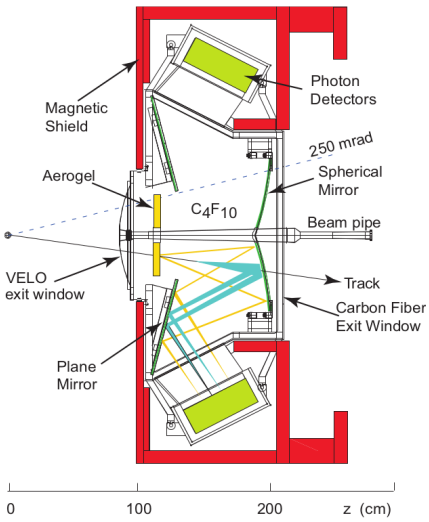

Figure 3.15: Side view schematic layout of the RICH 1 detector [61].

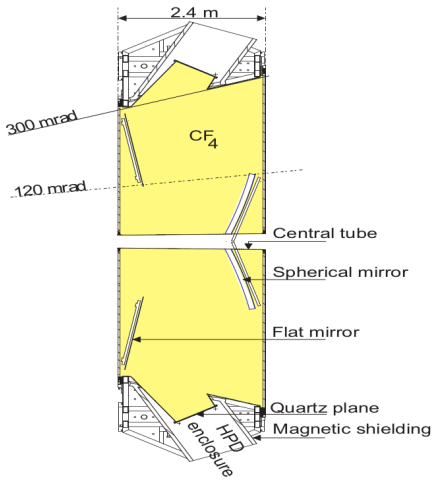

Figure 3.16: Top view schematic of the RICH 2 detector [61].

3.2.5 Calorimeters

The calorimeter system selects high transverse energy hadron, electron and photon candidates for the first trigger level (L0). It provides the identification of electrons, photons and hadrons as well as the measurement of their energies and positions.

A classical structure of an electromagnetic calorimeter (ECAL) followed by a hadron calorimeter (HCAL) has been adopted. The rejection of a high background of charged

pions requires longitudinal segmentation of the electromagnetic shower detection, i.e. a preshower detector (PS) followed by the main section of the ECAL. The choice of the lead thickness results from a compromise between trigger performance and ultimate energy resolution. The electron trigger must also reject a background of π^0's with high E_T. Such rejection is provided by the introduction, in front of the PS, of a scintillator pad detector (SPD) plane used to select charged particles. A thin lead converter is placed between SPD and PS detectors. Optimal energy resolution requires the full containment of the showers from high energy photons. For this reason, the thickness of ECAL was chosen to be 25 radiation lengths (X_0). On the other hand, the trigger requirements on the HCAL resolution do not impose a stringent hadronic shower containment condition. Its thickness is therefore set to 5.6 interaction lengths due to space limitations.

The PS/SPD, ECAL and HCAL adopt a variable lateral segmentation, shown in Figure 3.17, since the hit density varies by two orders of magnitude over the calorimeter surface. A segmentation into three different sections has been chosen for the ECAL and projectively for the SPD/PS. Given the dimensions of the hadronic showers, the HCAL is segmented into two zones with larger cell sizes.

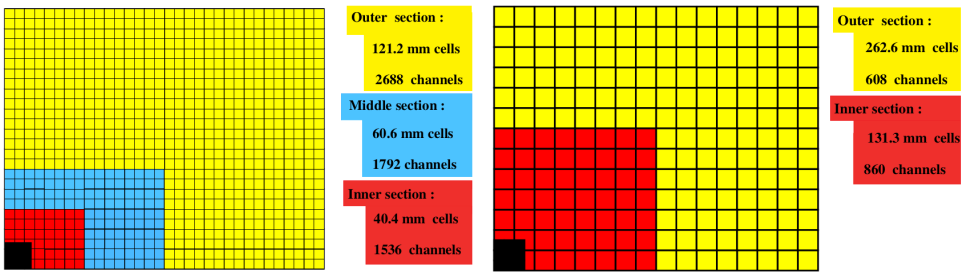

Figure 3.17: Lateral segmentation of the SPD/PS and ECAL (left) and the HCAL (right). One quarter of the detector front face is shown [61].

The SPD/PS detector consists of a 15 mm lead converter 2.5 X_0 thick, that is sandwiched between two almost identical planes of rectangular scintillator pads of high granularity with a total of 12,032 detection channels. The sensitive area of the detector is 7.6 m wide and 6.2 m high. Due to the projectivity requirements, all dimensions of the

SPD plane are smaller than those of the PS by $\approx 0.45\%$. The detector planes are divided vertically into two halves. Each can slide independently on horizontal rails to the left and right side in order to allow service and maintenance work. The distance along the beam axis between the centres of the PS and the SPD scintillator planes is 56 mm.

SPD is particularly important for exclusive production analyses as it is present on the trigger decisions of CEP data. A recurrent used variable is n(SPD hits) defined as the number of hits observed in SPD as a result of a primary interaction. *Hit* is defined as a point in a sub-detector crossed by a charged particle.

3.2.6 Muon system

Muon triggering and offline muon identification are fundamental requirements of the LHCb experiment. Muons are present in the final states of many CP-sensitive B decays, in particular the two *gold-plated* decays, $B^0_d \to J/\psi(\mu^+\mu^-)K^0_S$ and $B^0_s \to J/\psi(\mu^+\mu^-)\varphi$. They play a major role in CP asymmetry and oscillation measurements, since muons from semi-leptonic b decays provide a tag of the initial state flavour of the accompanying neutral B mesons. In addition, the study of rare B decays such as the flavour-changing neutral current decay, $B^0_s \to \mu^+\mu^-$, may reveal new physics beyond the Standard Model. For both the analyses described in this document, the muon system is very important as the final state of these studies are dimuons. Correct identification and measurement of kinematic variables are crucial to ensure the least possible error. The muon system provides fast information for the high-p_T muon trigger at the earliest level (Level-0) and muon identification for the high-level trigger (HLT) and offline analysis.

The muon system, shown in Figure 3.18, is composed of five stations (M1-M5) of rectangular shape, placed along the beam axis. The full system comprises 1,380 chambers and covers a total area of 435 m^2. The inner and outer angular acceptances of the muon system are 20 mrad (16 mrad) and 306 mrad (258 mrad) in the bending (non-bending) plane respectively. This results in an acceptance of about 20% for muons from inclusive

b semileptonic decays.

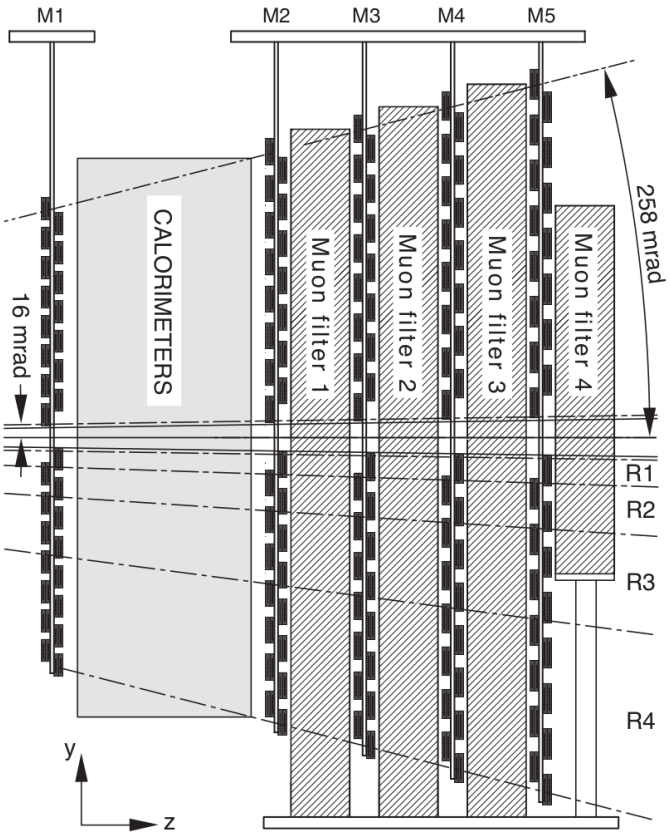

Figure 3.18: Side view of the muon system [61].

Stations M2 to M5 are placed downstream the calorimeters and are interleaved with iron absorbers 80 cm thick to select penetrating muons. The minimum momentum of a muon to cross the five stations is approximately 6 GeV/c since the total absorber thickness, including the calorimeters, is approximately 20 interaction lengths. Station M1 is placed in front of the calorimeters and is used to improve the p_T measurement in the trigger. The geometry of the five stations is projective, meaning that all their transverse dimensions scale with the distance from the interaction point.

The detectors provide space point measurements of the tracks, providing binary (yes/no) information to the trigger processor and to the data acquisition system. The information is obtained by partitioning the detector into rectangular logical pads whose dimensions

define the x, y resolution.

The muon trigger is based on stand-alone muon track reconstruction and p_T measurement and requires aligned hits in all five stations. Stations M1-M3 have a high spatial resolution along the x coordinate (bending plane). They are used to define the track direction and to calculate the p_T of the candidate muon with a resolution of 20%. Stations M4 and M5 have a limited spatial resolution, their main purpose being the identification of penetrating particles.

Appropriate programming of the L0 processing unit allows the muon trigger to operate in the absence of one station (M1, M4 or M5) or with missing chamber parts, although with degraded performance (worse p_T resolution).

The layout of the muon stations is shown in Figure 3.19. Each Muon Station is divided into four regions, R1 to R4 with increasing distance from the beam axis. The linear dimensions of the regions R1, R2, R3, R4, and their segmentations scale in the ratio 1:2:4:8. With this geometry, the particle flux and channel occupancy are expected to be roughly the same over the four regions of a given station. The (x, y) spatial resolution worsens far from the beam axis, where it is in any case limited by the increase of multiple scattering at large angles. The right part of Figure 3.19 shows schematically the partitioning of the station M1 into logical pads and the (x, y) granularity. Multi-wire proportional chambers (MWPC) are used for all regions except the inner region of station M1 where the expected particle rate exceeds safety limits for ageing. In this region triple-GEM detectors are used.

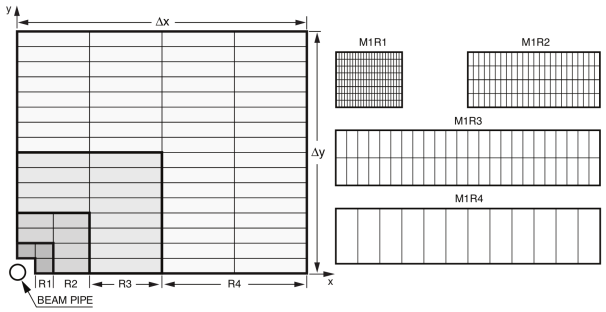

Figure 3.19: Left: front view of a quadrant of a muon station. Each rectangle represents one chamber. Each station contains 276 chambers. Right: division into logical pads of four chambers belonging to the four regions of station M1. In each region of stations M2-M3 (M4-M5) the number of pad columns per chamber is double (half) the number in the corresponding region of station M1, while the number of pad rows per chamber is the same [61].

3.2.7 Trigger

The LHCb experiment operates at an average luminosity of $2 \times 10^{32}\,\mathrm{cm}^{-2}\mathrm{s}^{-1}$, much lower than the maximum design luminosity of the LHC, reducing the radiation damage to the detectors and electronics. Furthermore, the number of interactions per bunch crossing (or event) is dominated by single interactions, which facilitates the triggering and reconstruction by assuring low channel occupancy. Due to the LHC bunch structure and low luminosity, the crossing frequency with interactions visible by the spectrometer is about 10 MHz for $\sqrt{s} = 7\,\mathrm{TeV}$ or 8 TeV, which has to be reduced by the trigger to about 2 kHz, at which rate the events are written to storage for further offline analysis. This reduction is achieved in two trigger levels as shown in Figure 3.20: Level-0 (L0) and the High Level Trigger (HLT). The L0 trigger is implemented using custom made electronics, operating synchronously with the 40 MHz bunch crossing frequency, while the HLT is executed asynchronously on a processor farm, using commercially available equipment. At a luminosity of $2 \times 10^{32}\,\mathrm{cm}^{-2}\mathrm{s}^{-1}$ the bunch crossings with visible pp interactions are expected to contain a rate of about 100 kHz of $b\bar{b}$-pairs. However, only about 15% of these events will include at least one B meson with all its decay products contained in the spectrometer acceptance. Furthermore the branching ratios of interesting

B meson decays used to study for instance CP violation are typically less than 10^{-3} . The offline analysis uses event selections based on the masses of the B mesons, their lifetimes and other stringent cuts to enhance the signal over background. For the best overall performance the trigger was therefore optimised to achieve the highest efficiency for the events selected in the offline analysis, while rejecting uninteresting background events as strongly as possible.

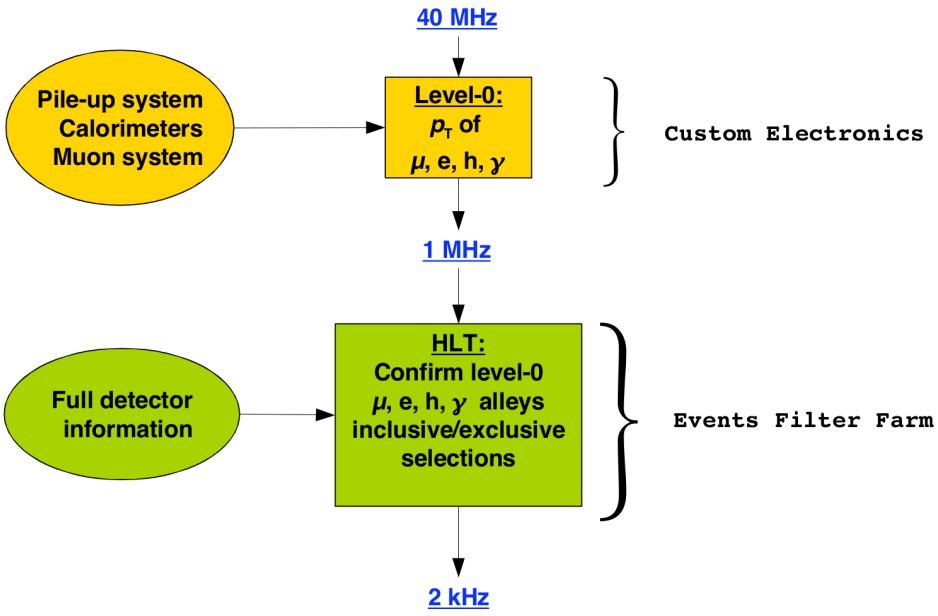

Figure 3.20: Scheme of the LHCb trigger [61].

The purpose of the L0 trigger is to reduce the LHC beam crossing rate of 40 MHz to the rate of 1 MHz with which the entire detector can be read out. Due to their large mass, B mesons decays often produce particles with large transverse momentum (p_T) and energy (E_T) respectively. The L0 trigger attempts to reconstruct:

- the highest E_T hadron, electron and photon clusters in the calorimeters,
- the two highest p_T muons in the muon chambers.

In addition, a pile-up system in the VELO estimates the number of primary pp interactions in each bunch crossing. The calorimeters calculate the total observed energy and an

estimate for the number of tracks, based on the number of hits in the SPD. With the help of these global quantities events may be rejected, which would otherwise be triggered due to large combinatorics, and would occupy a disproportionate fraction of the data-flow bandwidth or available processing power in the HLT.

A L0 Decision Unit (DU) collects all the information and derives the final L0 trigger decision for each bunch crossing. It allows for overlapping of several trigger conditions and for prescaling.

The L0 trigger system is fully synchronous with the 40 MHz bunch crossing signal of the LHC. The latencies are fixed and depend neither on the occupancy nor on the bunch crossing history. All L0 electronics is implemented in fully custom-designed boards which make use of parallelism and pipelining to do the necessary calculations with sufficient speed. In order to be able to reduce the event rate from 1 MHz down to 2 kHz, the HLT makes use of the full event data. The generic HLT algorithms refine candidates found by the L0 trigger and divide them into independent alleys. The alleys to be followed are selected from the L0 decision. The alley selections are based on the principle of confirming a previous trigger stage by requiring the candidate tracks to be reconstructed in the VELO and/or the T-stations. Requiring candidate tracks with a combination of high p_T and/or large impact parameter reduces the rate to about 30 kHz. At this rate interesting final states are selected using inclusive and exclusive criteria.

Generally speaking, selection cuts are relaxed compared to the offline analysis, in order to be able to study the sensitivity of the selections and to profit from refinements due to improved calibration constants. A large fraction of the output bandwidth is devoted to calibration and monitoring. In order to monitor trigger efficiencies and systematic uncertainties both trigger levels can be emulated fully on stored data.

CEP triggers

The trigger lines used in the search of exclusive productions exploit the singular characteristics of such processes, *i.e.*, low momentum of final state particles and low activity

in the detector. Exclusive processes can be seen as quasi-elastic collisions. In order to conserve momentum and energy, the momentum transfered to the centrally produced particles must be small. In particular in an environment of $b-$ and $c-$hadrons decays this is a distinguishable feature, as the final particles originated from these decays present high momentum.

Another crucial aspect of the exclusive production in the small number of produced particles in the detector acceptance, with the protons remaining intacts after the interaction. Since a few particles interact with the detector a small number of hits is detected as well as a small number of trajectories, or tracks, reconstructed per event.

CEP triggers hence are focused in selecting events with low number of tracks and hits and particles with low reconstructed momentum. In the analyses presented in this document, the non-resonant muon pair production in pp collisions and J/ψ production in PbPb collisions, it is expected that the dimuon and the J/ψ have small momentum. Therefore the muons individually may show high transverse momentum as they are created *back-to-back* in the dimuon (or J/ψ) frame.

3.2.8 Data storage

The LHCb data selected by trigger is recorded as RAW data. Simulated samples are recorded in a similar format with an extra "truth" information. In order to provide physical quantities such as momentum, energy and position a reconstruction is performed using the detector information stored in RAW format. The output of this reconstruction process is a new set of data called **D**ata **S**ummary **T**ape (DST). Previously acquired calibration data is used in order to perform the reconstruction. A set of pre-selection algorithms is applied to the reconstructed data in order to separate particular processes. This pre-selection is called *Stripping* and it is recognized as the first stage of the analysis procedure [71]. The complete logical dataflow scheme is presented in Figure 3.21.

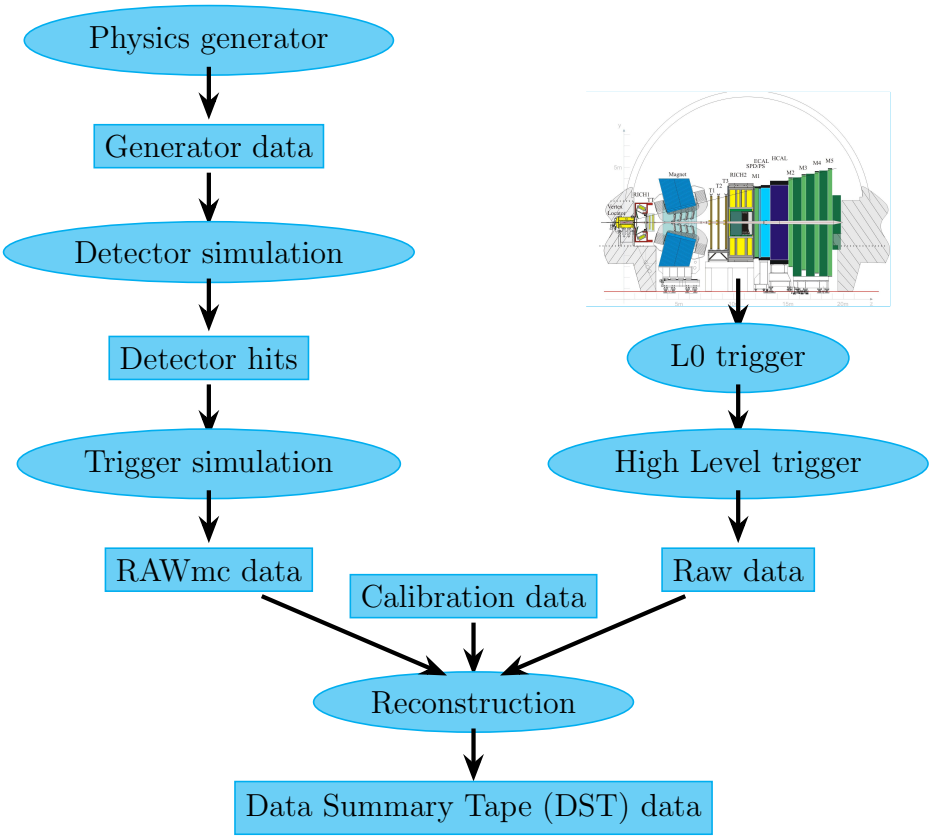

Figure 3.21: The LHCb computing logical dataflow model.

Several softwares are used by LHCb collaboration in the stages of data simulation and processing. These softwares are integrated on the Gaudi software framework. Gauss software [72] is used for the generation of simulation samples, since the simulation of *pp* collisions until detector material interaction simulation. Some external packages are employed throughout simulation by Gauss. The simulation of the *pp* colisions is performed by PYTHIA software [67, 68]. EVTGEN software [73] performs the description of the decays of the particles generated in the collision. GEANT4 simulates the interaction between particles and detector's materials [74, 75]. Boole is the digitization application, the final stage of the LHCb detector simulation [71]. It applies the detector response to the hits generated by Gauss. The Moore application is the software of the LHCb trigger, used for the implementation of the HLT algorithms. Brunel is the reconstruction application. It uses the information from the LHCb subdetectors to reconstruct the event,

including tracking and particle identification. The DaVinci application is the analysis framework. It allows vertex reconstruction and selection of events from the reconstructed data. The selected events with their related parameters of interest can be recorded for further analysis. These applications and dataflow are illustrated in Figure 3.22.

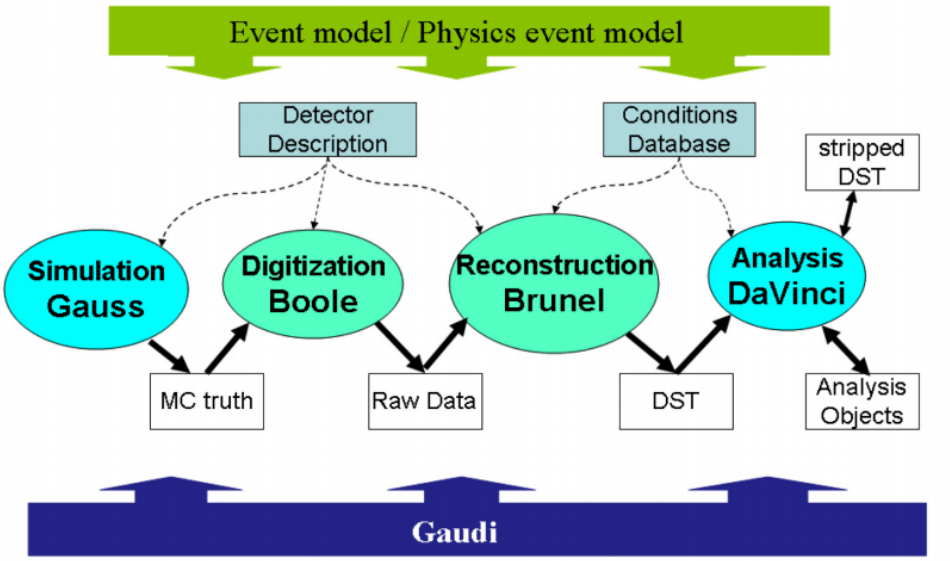

Figure 3.22: The LHCb data processing applications and data flow. Underlying all of the applications is the Gaudi framework and the event model describes the data expected. The arrows represent input/output data [71].

3.2.9 HeRSCheL

Although the design of LHCb was optimised for studies of heavy-flavour hadron decays, its operating conditions and sensitivity to low p_T particles make it ideally suited to measurements of CEP processes. The low multiplicity of the final state and the absence of activity, or large "rapidity gap", either side of the central system provides a distinctive signature of the CEP process. In practice, this signature can only be exploited by the nominal LHCb trigger in beam crossings where there are no additional interactions. The fraction of single interaction events within the acceptance of the LHCb spectrometer is relatively large during normal operation, being approximately 37% in 2015, 24% in 2011 and 19% in 2012. Contamination to the signal selection arises, however, from inelastic in-

teractions in which one or both protons disassociate. In these cases additional hadrons are produced at high rapidities, which generally means that they fall outside the acceptance of the sub-detectors of the spectrometer.

The sensitivity that HeRSCheL provides for high-rapidity particles enable the contamination from inelastic events in the CEP selection to be suppressed. Information from HeRSCheL is typically deployed in a veto mode. The absence of any significant activity in the **F**orward **S**hower **C**ounters (FSC) is used to confirm the existence of a rapidity gap extending beyond the spectrometer acceptance, and to add confidence to the central-exclusive hypothesis of CEP candidates. In this manner the purity of the CEP selection is improved, and the systematic uncertainties associated with the modelling of the residual background can be reduced.

As shown schematically in Figure 3.23, the HeRSCheL system comprises three stations at negative z, known as "backward" or "B" stations, and two stations at positive z, known as "forward" or "F" stations. The active element of each station is a plastic scintillator plane with outer dimensions of 600 mm $\times$ 600 mm, centred around the beam line. The shape and dimensions of the inner opening depend on the local vacuum chamber layout. Stations B0, B1, and F1 have circular holes with radii of 47 mm (B0, B1) and 61 mm (F1), respectively. For stations B2 and F2, the inner opening has a half-width of 115 mm in the horizontal direction (to encompass the two vacuum chambers), and a half-width of 54 mm in the vertical direction. The HeRSCheL stations are seen to add detector acceptance from five up to nearly ten pseudorapidity units.

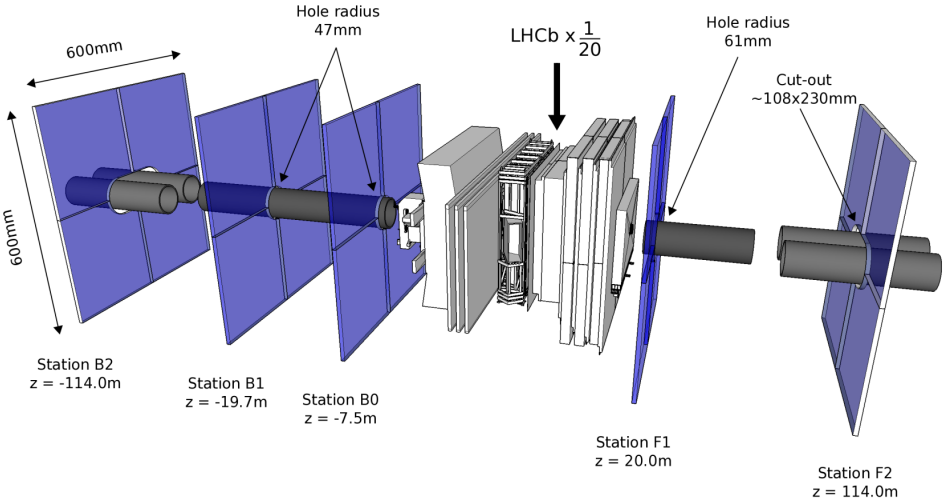

Figure 3.23: Layout of the active areas of the HeRSCheL stations around the LHCb interaction point, where for illustration the HeRSCheL stations have been magnified by a factor of 20 with respect to the rest of the LHCb detector. z-axis not to scale [70].

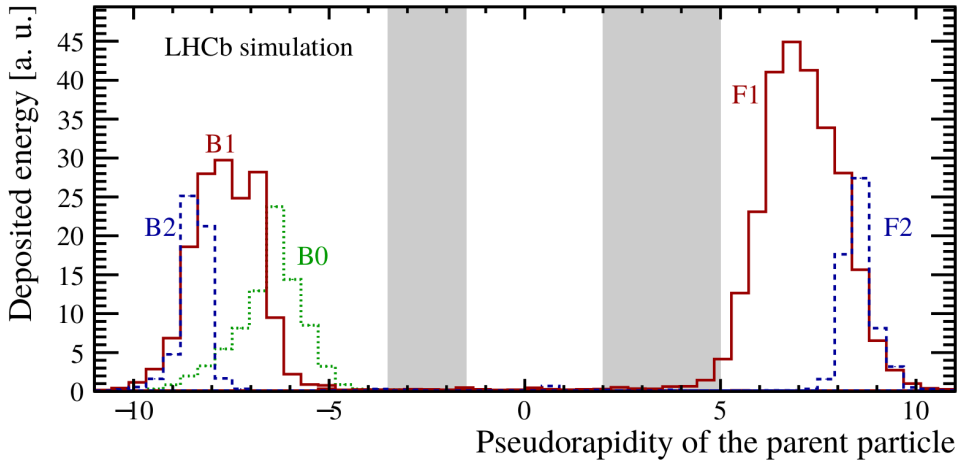

Figure 3.24: Energy deposit in the scintillators as a function of the pseudorapidity of the parent particle that caused the shower. The grey areas indicate the nominal pseudorapidity coverage of LHCb [70].

Empty-detector characterisation

Protons circulating in the LHC are distributed in bunches, separated from one another by 25 ns. Bunches are collected into "trains" by virtue of the injection procedure, separated by gaps. A 25 ns window within which proton bunches cross in LHCb is referred to as a "bunch crossing". Whilst the dominant contribution to the HeRSCheL empty-

detector signal is electronic noise, secondary contributions arise as the result of activity in nearby crossings which spill into the 25 ns time interval of the triggered crossing. The largest of these secondary contributions is the residual impact on detector electronics of successive large signals in the detector, during a train of proton-proton crossings in the LHC. It is found that the signal recorded in the counters in the window immediately after such a train, where no particle activity can be present, provides a good description of the empty-detector region of the ADC response, as in the case of a CEP interaction. This ADC response for each of the example counters is also shown in Figure 3.25.

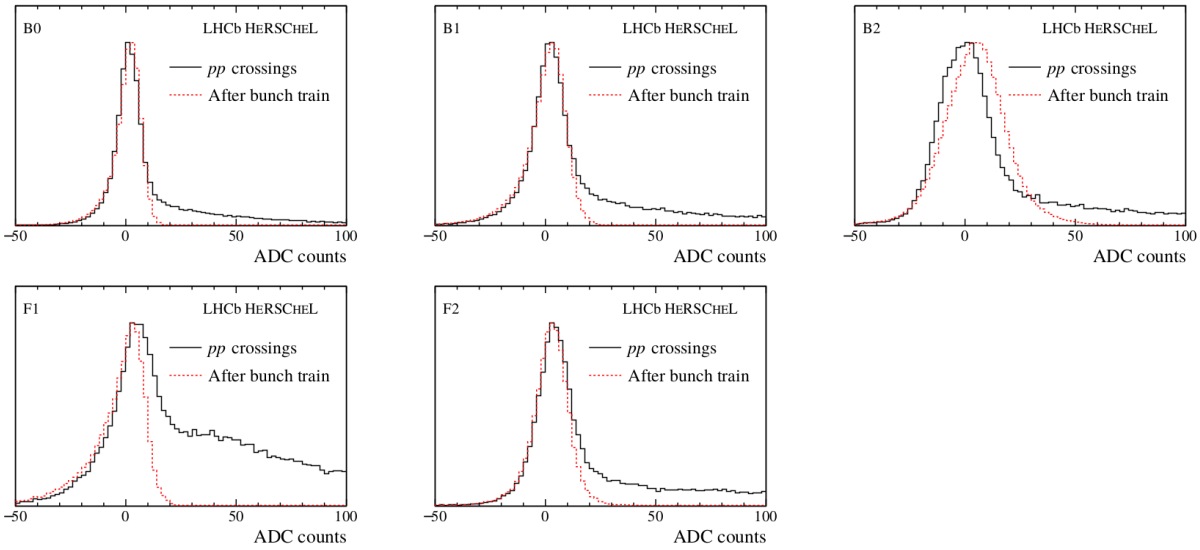

Figure 3.25: Activity registered for each HeRSCheL detector station during beam-beam crossings in the solid histogram. The empty-detector signal recorded after a bunch train is represented by the dotted histogram [70].

HeRSCheL variable

In order to construct a quantity that combines the responses of all twenty counters comprising the HeRSCheL detector effectively, it is beneficial to account for the characteristic distribution of the empty-detector signal in each counter. The most natural way to combine the activity in all the HeRSCheL detectors is to construct a χ^2 quantity, ξ_{HRC}, such that values of ξ_{HRC} close to zero correspond to events with little or no activity in all the HeRSCheL counters, as expected in the case of a single CEP interaction, and high

values of ξ_{HRC} correspond to events where the counter activity is elevated, as expected for non-CEP background.

This HeRSCheL's Figure of Merit (FOM), ξ_{HRC}, is given by:

$$\xi_{\mathrm{HRC}} = \ln\left[\sum_{i=1}^{20}\left(\frac{\mathrm{ADC}_i}{\mathrm{RMS}_i}\right)^2\right], \tag{3.1}$$

where ADC_i (analog-to-digital-converter) is a number proportional to the energy deposited in the i-th empty HeRSCheL counter in ADC counts. RMS_i is the sigma value of a Gaussian distribution of i-th empty HeRSCheL counter signals taken from the fit to ADC counts histograms. Grossly, ADC_i is the mean of the Gaussian fitted to the red distributions in Figure 3.25 and RMS_i is the standard deviation from the same fit procedure.

Chapter 4

Cross-section measurement of the exclusive production of muon pairs in pp collisions

Lepton pair production in proton-proton collisions is an excellent probe to test the fundamental electromagnetic nature of the Standard Model. As detailed in Chapter 2, the QED provides precise prediction for CEP of dimuon. A measurement of the cross-section of this reaction can be used as a luminosity measurement or calibration. In this chapter, the experimental determination of this cross-section using pp collisions acquired in LHCb during Run 1 is presented.

4.1 Method

The cross-section of a generic reaction, $pp \to X$, is defined experimentally as

$$\sigma\left(pp \to X\right) = \frac{N\left(pp \to X\right)}{\mathcal{L}} \tag{4.1}$$

where $N\left(pp \to X\right)$ is the number of occurrences of the $pp \to X$ reaction in a number of pp collisions corresponding to an integrated luminosity

$$\mathcal{L} = \int L dt \tag{4.2}$$

where L is the instantaneous luminosity. In this scenario, in order to obtain the cross-section of the central exclusive production

$$pp \to p\mu^+\mu^- p \tag{4.3}$$

it is necessary to determine how many times this CEP occurred out of the total number of collisions. Unfortunately it is not possible to determine this number directly. In fact, it is indirectly determined as

$$N\left(pp \to p\mu^+\mu^- p\right) = \frac{n\left(pp \to p\mu^+\mu^- p\right)}{\varepsilon} \tag{4.4}$$

where the signal efficiency, ε, is usually calculated using simulation samples. Therefore the cross-section formula with the accessible number of occurrences $n\left(pp \to p\mu^+\mu^- p\right)$ is

$$\sigma\left(pp \to p\mu^+\mu^- p\right) = \frac{n\left(pp \to p\mu^+\mu^- p\right)}{\varepsilon \cdot \mathcal{L}} \tag{4.5}$$

Thus, the objective is to obtain the number of events, $n\left(pp \to p\mu^+\mu^- p\right)$, after an event selection, the efficiency ε and the integrated luminosity of the data sample in order to determine the cross-section of dimuon CEP in pp collisions.

In this analysis only events with a single interaction are selected. Therefore, the number of events $n\left(pp \to p\mu^+\mu^- p\right)$ is reduced and a correction factor, called fraction of single interactions, f_{SI}, must be estimated and taken into account in order to determine the cross-section properly. The cross-section is finally determined by:

$$\sigma\left(pp \to p\mu^+\mu^- p\right) = \frac{n\left(pp \to p\mu^+\mu^- p\right)}{\varepsilon \cdot f_{SI} \cdot \mathcal{L}} \tag{4.6}$$

4.2 Samples

In this analysis the Run 1 LHCb data is used. The Run 1 comprises the data acquired during 2011 and 2012 years. In 2011, the collision energy was 7 TeV in the centre of mass frame. This energy was raised to 8 TeV in 2012. As the cross-section is expected to vary with the collision energy, the analysis is performed separately for each year.

4.2.1 Simulation samples

At the time this work began, there was no exclusive production generators in the LHCb simulation framework. Among all possible software, the event generator used is the LPair [37]. It was developed during the early 1980s and allows to simulate the full $\gamma\gamma \to \ell^+\ell^-$ reaction in a fully-embedded piece of code.

The method used in the code [76] provides an accurate description of both the elastic and dissociative component of the possible final states. The incoming particles can either be the *ep*, *ee*, or *pp*. The outgoing system is therefore defined as the central dilepton system produced, along with the outgoing beam particles. While the *ee* case leads to a trivial expression of the form factors, the proton-induced reactions can produce three different outcomes (listed in increasing order of Q^2 energy transfers): fully-elastic, single proton dissociative, fully-inelastic or double dissociative. In this thesis only the first option is used.

Even if LPair shows a good description of diffractive processes, it is an old code and there are some demands that are not met by this generator. The controllable kinematic parameters are not flexible enough. In fact, a script based in Python and BASH was developed to enable a pre-selection at generator level in order to reduce the time consumption and disk space of reconstruction of simulated samples. The variables and the cuts used to produce the simulation samples are listed in Table 4.1. Event generation is performed considering the center-of-mass energy of $\sqrt{s} = 7\,\text{TeV}$ ($\sqrt{s} = 8\,\text{TeV}$) for 2011 (2012) data analysis. In order to determine the efficiency the simulated data is reconstructed using the same LHCb framework used to reconstruct collision data.

Table 4.1: Lpair generator kinematic parameters for non-resonant dimuons.

Property	**Criterion**
Pseudorapidity (both muon candidates)	$1.5 \leq \eta(\mu^{\pm}) \leq 5.0$
Transverse momentum (both muon candidates)	$p_T(\mu^{\pm}) \geq 375\,\text{MeV}/c$
Invariant mass (dimuon candidate)	$m(\mu^+\mu^-) \geq 1\,\text{GeV}/c^2$

4.3 Selection

At L0 trigger, events are selected by the criteria shown in Table 4.2. The SPD multiplicity is defined as the number of hits observed in the SPD sub-setector. There is only one criterion in the HLT: both muons have $p_T > 400\,\mathrm{MeV}/c^2$. This trigger line was only implemented in May 2011 and any data taken before this are excluded.

Table 4.2: L0 trigger criteria used to select non-resonant dimuons.

Property	**Criterion**
SPD multiplicity	$n(\mathrm{SPD\,hits}) < 10$
Transverse momentum (at least one muon)	$p_T(\mu) > 200\,\mathrm{MeV}/c^2$

The pre-selection detailed in Table 4.3 is applied offline. $n(\mathrm{Long\,Tracks})$ is the number of long tracks in the event and $n(\mathrm{Back\,Tracks})$ is the number of backward tracks in the event. Long tracks traverse the full tracking system. They have hits in both the VELO and the T stations, and optionally in TT. As they traverse the full magnetic field they have the most precise momentum estimate and therefore are the most important set of tracks for physics analyses. An illustration in Figure 4.1 shows the representation of a long track crossing the LHCb detector and the B_y field as well. The selection $n(\mathrm{Long\,Tracks}) > 0$ is a very loose cut as muon tracks are expected to be long. However it removes fully elastic interactions were the protons interact but do not dissociate or provoke a CEP. On the other hand, a backward track is associated with a particle which is created inside the VELO but its momentum points to the pile-up stations of VELO. Thus the selection $n(\mathrm{Back\,Tracks}) < 1$ rejects CEP-like events with extra backward tracks not fully detected by LHCb sub-detectors.

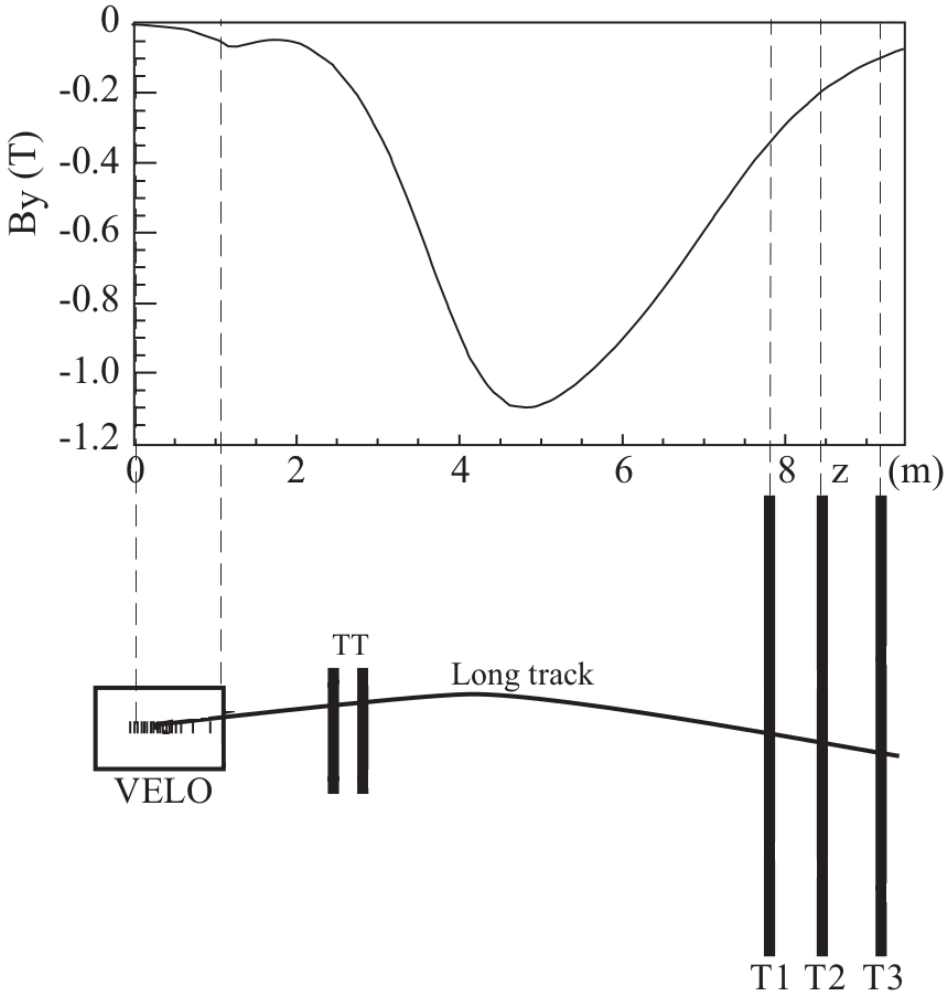

Figure 4.1: A schematic illustration of the long track type. For reference the main B-field component (B_y) is plotted above as a function of the z coordinate [62].

Table 4.3: Pre-selection applied to the non-resonant dimuons.

Property	**Criterion**
n(Long Tracks)	> 0
n(Back Tracks)	< 1

A final set of selection is applied offline in order to reduce the contamination from events where the dimuon is produced inclusively. The criteria, shown in Table 4.4, are therefore chosen in order to select events with no activity in the detector other than that associated to the dimuon.

Table 4.4: Offline selection criteria applied to the non-resonant dimuons.

Property	**Criterion**
Pseudorapidity (both muon candidates)	$2 \leq \eta(\mu^{\pm}) \leq 4.5$
Track type (both muon candidates)	Long
Muon ID (both muon candidates)	True
n(Long Tracks)	$= 2$
n(Muon Tracks)	$= 2$
Transverse momentum (dimuon candidate)	$p_T^2(\mu^+\mu^-) \leq 2\,(\mathrm{GeV}/c)^2$
Invariant mass (dimuon candidate)	$0 \leq m(\mu^+\mu^-) \leq 20\,\mathrm{GeV}/c^2$
Resonance vetoes	
Low mass resonances (ρ, a, η)	$m \geq 1.5\,\mathrm{GeV}/c^2$
J/ψ	$m \leq m(J/\psi) - 300\,\mathrm{MeV}/c^2$ or $m \geq m(J/\psi) + 100\,\mathrm{MeV}/c^2$
$\psi(2S)$	$\lvert m - m(\psi(2S))\rvert \geq 100\,\mathrm{MeV}/c^2$
$\Upsilon(nS)$ $(n = 1, 2, 3)$	$m \leq 9$ or $m \geq 10.6\,\mathrm{GeV}/c^2$

In this analysis, a long track is identified as a muon when hits in the muon system are found with a pattern which matches the trajectory in the tracking system (Muon ID). The transverse momentum of the dimuon system p_T^2 is expected to be low in CEP as the momentum transfer is smaller in this case (see Chapter 2). The last criteria of Table 4.4 are designed to reject CEP of resonances decaying in two muons. The low mass resonances (ρ, a, η, etc.) are rejected by requiring the dimuon invariant mass to be greater than $1.5\,\mathrm{GeV}/c^2$. For the J/ψ veto we remove all candidates with dimuon invariant mass within 2.796 and $3.196\,\mathrm{GeV}/c^2$. The ψ(2S) resonance is rejected by removing candidates with dimuon invariant mass between 3.586 and $3.786\,\mathrm{GeV}/c^2$. The dimuon invariant mass window rejection from 9 to $10.6\,\mathrm{GeV}/c^2$ is responsible to take out the Υ resonances from our samples. The dimuon system p_T^2 distribution of all samples after all selections is presented in Figures 4.2 and 4.3 for 2011 and 2012 data set respectively. The invariant mass of dimuons is shown in the Figures 4.4 and 4.5 for 2011 and 2012 data set respectively. These distributions are expected to contain three components: CEP, partially inelastic with the dissociation of one of the protons and the fully inelastic where both protons dissociate. In terms of $p_T^2(\mu\mu)$, the full inelastic contribution shows larger

values in comparison with the partial inelastic contribution. The CEP process is expected to exhibit a narrow distribution around zero in $p_T^2(\mu\mu)$ as one can see in the Figures 4.2 and 4.3.

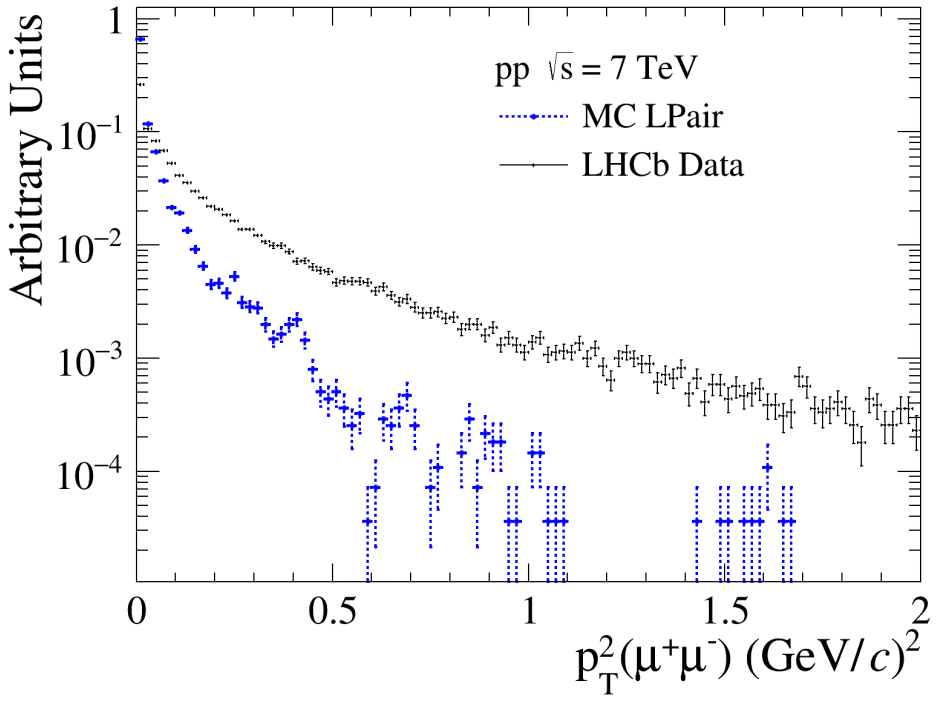

Figure 4.2: Square transverse momentum distribution using dimuons from LPair simulated and LHCb data of the CEP $pp \to p\mu\mu p$ where $\sqrt{s} = 7\,\text{TeV}$ and the full selection chain is applied.

4.4 Selection efficiency

Simulated events are used to detemine the selection efficiency. The total efficiency is factorised in the three stages of the selection presented in the previous section:

$$\varepsilon = \varepsilon_{pre-selection} \cdot \varepsilon_{trigger} \cdot \varepsilon_{offline} \tag{4.7}$$

The definition of each efficiency is given by:

$$\varepsilon_i = \frac{N_{After}}{N_{Before}}, \tag{4.8}$$

where i = trigger, pre-selection or offline and N_{After} is the number of events in the simulated sample after the i-th selection and N_{Before} is the number of events in the simulated

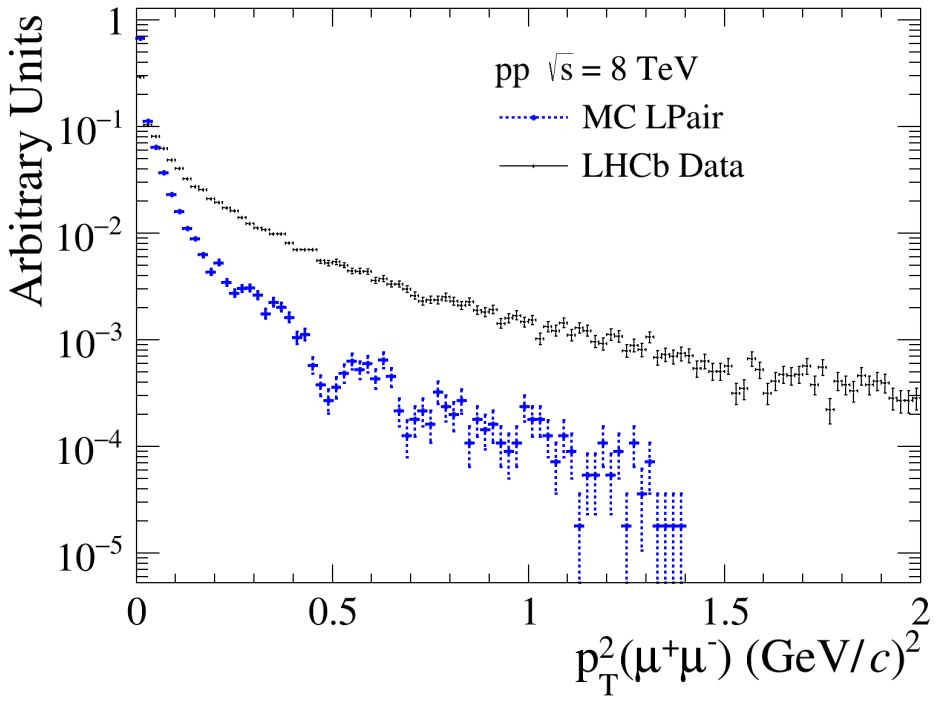

Figure 4.3: Square transverse momentum distribution using dimuons from LPair simulated and LHCb data of the CEP $pp \to p\mu\mu p$ where $\sqrt{s} = 8\,\text{TeV}$ and the full selection chain is applied.

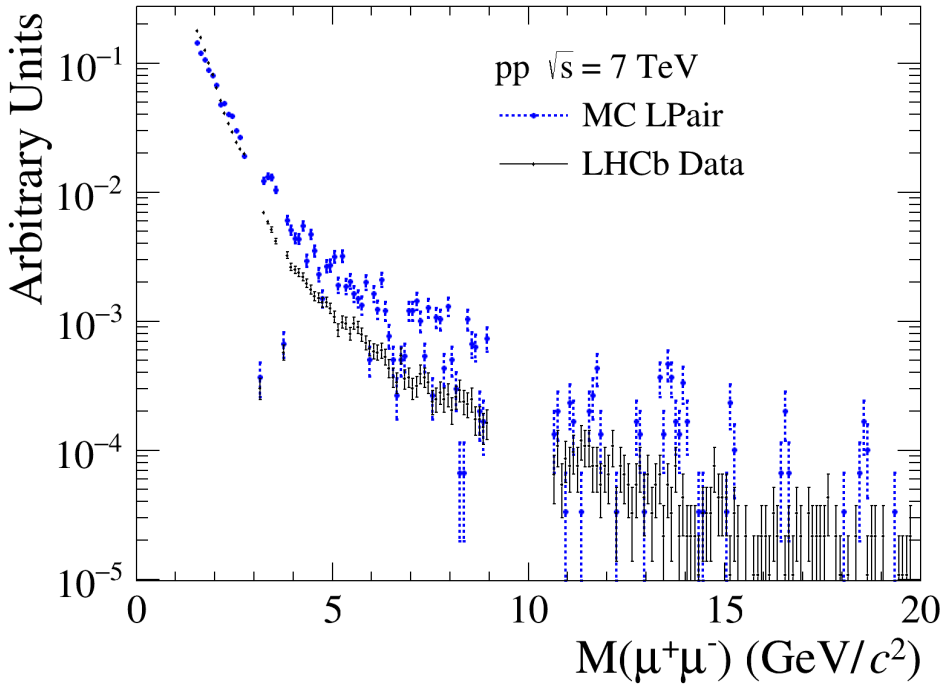

Figure 4.4: Invariant mass distribution using dimuons from LPair simulated and LHCb data of the CEP $pp \to p\mu\mu p$ where $\sqrt{s} = 7\,\text{TeV}$ and the full selection chain is applied.

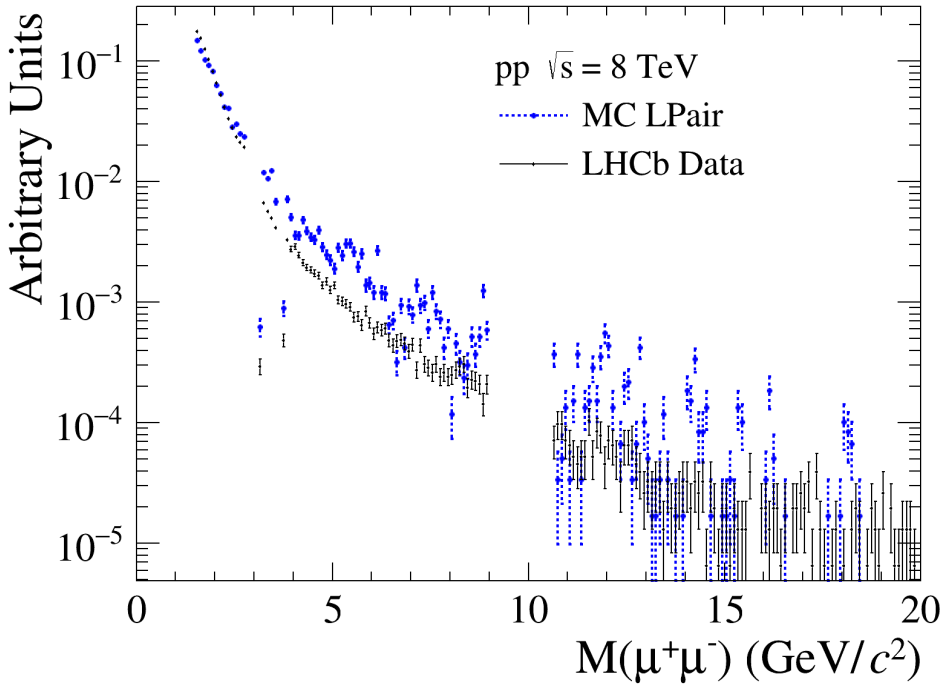

Figure 4.5: Invariant mass distribution using dimuons from LPair simulated and LHCb data of the CEP $pp \to p\mu\mu p$ where $\sqrt{s} = 8\,\text{TeV}$ and the full selection chain is applied.

sample before applying the i-th selection. The efficiencies of the trigger and acceptance, pre-selection and offline selections are presented in Table 4.5. The uncertainties are statistical and estimated assuming a binomial distribution for the number of events satisfying a given selection step.

Table 4.5: Efficiency of the different sets of selection criteria. Uncertainties are statistical.

Selection	$\sqrt{s} = 7\,\text{TeV}$	$\sqrt{s} = 8\,\text{TeV}$
Acceptance and Trigger	$(86.96 \pm 0.11)\%$	$(86.94 \pm 0.08)\%$
Pre-selection	$(99.993 \pm 0.003)\%$	$(99.992 \pm 0.002)\%$
Offline selection	$(36.85 \pm 0.17)\%$	$(36.70 \pm 0.12)\%$
Full selection	$(31.22 \pm 0.15)\%$	$(31.16 \pm 0.11)\%$

4.5 Integrated luminosity

A complete description of the luminosity measurements can be found in the reference [77]. The integrated luminosity is found to be:

$$\mathcal{L}\left(\sqrt{s} = 7\,\text{TeV}\right) = (0.908 \pm 0.012)\,\text{fb}^{-1}, \tag{4.9}$$

and

$$\mathcal{L}\left(\sqrt{s} = 8\,\text{TeV}\right) = (1.990 \pm 0.016)\,\text{fb}^{-1}. \tag{4.10}$$

Fraction of single interactions

The cuts related to the event (*e.g.* $n(\text{Long Tracks}) = 2$) remove not only non-CEP of dimuons, but they also exclude pp collisions where more than one pp interaction took place. It is therefore necessary to multiply the full integrated luminosity by a factor which is the fraction of events with no additional interactions. This factor can be determined by using data containing n_{total} randomly triggered events, and applying our selection criteria to find the fraction of events where no interactions are observed. The level of detector activity which is defined as an interaction in addition to the signal candidate depends on the global event cuts employed in the selection. The fraction of n_{total} events which pass the requirements that $n(\text{SPD hits}) < 8$, $n(\text{Back Tracks}) = 0$, $n(\text{Long Tracks}) = 0$ and $n(\text{Muon Tracks}) = 0$ is $(23.620 \pm 0.027)\%$ for 2011 and $(18.466 \pm 0.017)\%$ for 2012.

4.6 Determination of the yield of CEP

The yield of CEP candidates (N_{CEP}) is obtained from a fit to the $p_T^2(\mu^+\mu^-)$ distribution. The 2011 and 2012 data sets are fitted separately. The distributions to be fitted are represented in Figures 4.2 and 4.3 where the three contributions are CEP, partial inelastic and full inelastic. It is assumed that each inelastic background components are distributed according to a single exponential function ($e^{-bp_T^2}$). The slope and yield of this background function are free to vary in the fit. The shape of the CEP signal is taken from

simulated data using a kernel estimator and used as a fixed template, T_{CEP}, in the total fit function:

$$F(p_T^2) = N_{CEP} \cdot T_{CEP} + N_{partial} \cdot e^{-b_1 p_T^2} + N_{full} \cdot e^{-b_2 p_T^2} \tag{4.11}$$

where all N's and both b's are free to vary. The fits to LHCb data are shown in Figures 4.6 and 4.7.

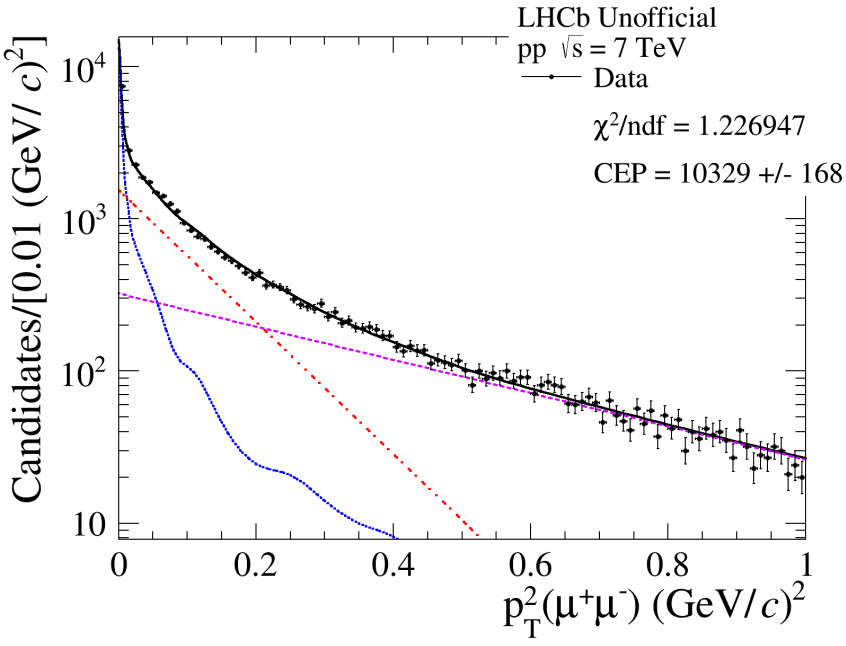

Figure 4.6: Fit to quadratic transverse momentum for 2011 LHCb data. The dots represent the data, the blue line the signal contribution and the purple and red lines corresponds to the inelastic contributions.

4.7 Cross-section measurement

The cross-section is given by

$$\sigma = \frac{N_{CEP}}{f_{SI} \cdot \mathcal{L} \cdot \varepsilon}, \tag{4.12}$$

where N_{CEP} is the yield of exclusive signal candidates determined from the fit to p_T^2, the integrated luminosity is represented by $\mathcal{L}$, the fraction of events with only one interaction is f_{SI} and the quantity ε is the efficiency correction. Using the results from the previous

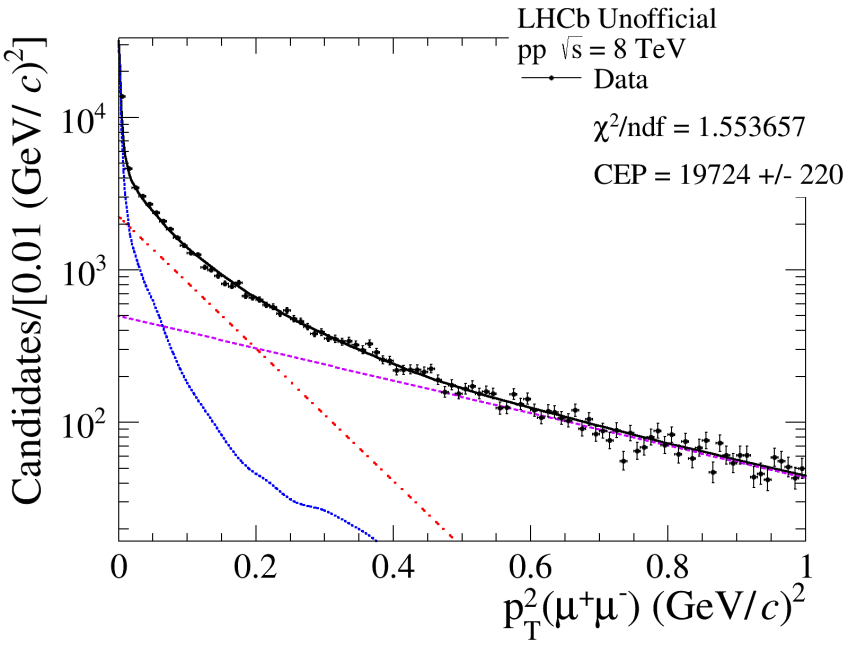

Figure 4.7: Fit to quadratic transverse momentum for 2012 LHCb data. The dots represent the data, the blue line the signal contribution and the purple and red lines corresponds to the inelastic contributions.

sections, we have:

$$\sigma(pp \to p\mu^+\mu^- p, \sqrt{s} = 7\,\text{TeV}) = (154.2 \pm 2.5)\,\text{pb} \tag{4.13}$$

$$\sigma(pp \to p\mu^+\mu^- p, \sqrt{s} = 8\,\text{TeV}) = (172.3 \pm 1.9)\,\text{pb} \tag{4.14}$$

Comparison with theory prediction

In order to obtain the cross-section prediction in the LHCb geometrical acceptance the SuperChic generator is used [78]. The cross-section is calculated within the pseudo-rapidity $2 < \eta < 4.5$ and for the center-of-mass energies of $\sqrt{s} = 7$ TeV and $\sqrt{s} = 8$ TeV. The results are listed below.

$$\sigma_{theo}(pp \to p\mu^+\mu^- p, \sqrt{s} = 7\,\text{TeV}) = (158.66 \pm 1.0)\,\text{pb} \tag{4.15}$$

$$\sigma_{theo}(pp \to p\mu^+\mu^- p, \sqrt{s} = 8\,\text{TeV}) = (166.81 \pm 0.98)\,\text{pb} \tag{4.16}$$

4.8 Conclusions

The cross-section of dimuon non-resonant CEP is measured using pp collisions for two center-of-mass energies. A first comparison with theoretical prediction is available through the SuperChic event generator and a discrepancy of 1.7σ (2.6σ) is observed in the $\sqrt{s} = 7\,\text{TeV}$ ($\sqrt{s} = 8\,\text{TeV}$) data analysis. The measured cross-section uncertainties are purely statistical and a next step for this analysis is to determine the systematic uncertainties. The measurement of differential cross-section in bins of dimuon rapidity or pseudorapidity may be useful as well in order to compare with theoretical predictions.

Chapter 5

Cross-section measurement of J/ψ coherent production in PbPb collisions

Heavy ion collisions at the LHC are an excellent environment to study gamma-gamma or gamma-nucleus interactions with or without break-up of any of the nuclei. In gamma-nucleus interaction, one can study vector meson production, e.g. J/ψ, which is sensitive to the square of the nuclear gluon density at the leading order of perturbation. This makes those production processes ideal probes to study and constraint gluon distribution functions in the small Bjorken-x regime (typically from 10^{-5} until 10^{-2} for the present analysis, depending on which nuclei emits the photon) and at energy scales of $Q^2 \approx m^2_{J/\psi}/4$, where those functions are poorly constrained. At this regime, saturation phenomena are expected, giving an insight of non-linear properties of the gluonic interactions at high-field density.

5.1 Analysis Strategy

In this work, a measurement for gamma-nucleus coherent J/ψ production is performed using the LHCb data of lead ion collisions taken in 2015. Even though the coherent production is expected to occur with a higher cross-section in UPC, there are other two important contributions to J/ψ production that must be considered: incoherent production

(with break-up of one or both of the heavy ions) and decay of coherent $\psi(2S)$ production (feed-down). Note that the branching ratio $\mathcal{B}[\psi(2S) \to J/\psi + \text{anything}] = (61.4 \pm 0.6)\%$ [2]. These two constributions constitute the main background sources for our exclusive J/ψ sample.

As for the previous analysis presented in Chapter 4, the cross-section is given by Equation 4.1. However, since background contributions are expected, an event selection must be used and efficiency corrections applied. Moreover, in order to compare with different theoretical models, the cross-section measurement is performed in bins of J/ψ rapidity. A last important aspect is that the J/ψ meson is not directly observed. Rather than that, only its decay products are directly detected by the LHCb detector. In this work the decay $J/\psi \to \mu^+\mu^-$ is studied in order to measure the cross-section of J/ψ production. Therefore, the cross-section calculation must be corrected also by the branching ratio of this decay. In conclusion, the differential cross-section of J/ψ coherent production can be written as:

$$\frac{\mathrm{d}\sigma_{\text{coh}}}{\mathrm{d}y} = \frac{n_{\text{coh}}}{\varepsilon_y \cdot \Delta y \cdot \mathcal{L} \cdot \mathcal{B}}, \tag{5.1}$$

where ε_y is the efficiency and acceptance correction factor for each rapidity bin, n_{coh} is the coherent yield observed in the experiment after selection, Δy is the bin width in meson rapidity, $\mathcal{L}$ is the integrated luminosity of the used sample and $\mathcal{B} = (5.961 \pm 0.033)\%$ [2] is the branching ratio of $J/\psi \to \mu^+\mu^-$.

The total efficiency is the product of trigger, track reconstruction, muon identification and offline selection efficiencies. These efficiencies are mostly determined using simulated samples with the exception of HLT efficiency. All efficiencies are described in Section 5.4. The signal yield is determined in two steps. First, a fit to the dimuon invariant mass spectrum is performed to obtain the number of J/ψ candidates, which includes coherent and incoherent J/ψ and $\psi(2S)$ feed-down components. A fit to the J/ψ transverse momentum, p_T, is used to estimate the number of signal candidates where the non-resonant background is constrained from the first fit.

5.2 Samples

The data used in this analysis are PbPb collisions at $\sqrt{s_{NN}} = 5\,\text{TeV}$, collected by the LHCb collaboration in November and December 2015. In about two thirds of the data taking Argon was injected in the interaction region in order to collect Pb-Ar interactions at the same time.

In total, four MC samples are used in this analysis. Three simulated samples were generated using the STARlight [53] event generator and the remaining sample was based on the SuperChic event generator [32].

The STARlight samples are compounded by 10^{10} events of coherently produced J/ψ mesons decaying to dimuons, 10^{10} events of incoherently produced J/ψ mesons decaying to dimuons and 10^{10} events of two-photon reactions $\gamma\gamma \to \mu^+\mu^-$. These samples are produced only at generator level and a smearing process is applied in order to match the detector response before the usage of these samples in the fit procedure described in Section 5.5.

The SuperChic samples have been privately produced and provided by the group of the J/ψ CEP cross-section measurement at 13 TeV pp collisions [79]. A full detector simulation and reconstruction is implemented using the Geant4 toolkit [75]. A total of 100,000 signal events for $J/\psi \to \mu^+\mu^-$ were generated. This sample is to determine the efficiencies described in Section 5.4

5.3 Selection

Events containing a coherently photo-produced J/ψ meson are expected to contain two identified muons in the LHCb acceptance and nothing else. In this section the trigger strategy and offline selections applied to select candidate events are described.

5.3.1 Trigger selection

Two different trigger strategies (paths) are used in this analysis:

- *muon trigger strategy*: this trigger path is the one used in the data analysis. The events are selected by the lines `L0MUON` at L0 and `Hlt1DiMuonHighMass` at HLT1, as described in Table 5.1.

- *min-bias trigger strategy*: this trigger path is used for efficiency studies only. The lines L0SPD and Hlt1BBMicroBiasVELO and its requirements are used to select events (see Table 5.1).

A summary of the trigger line conditions is given in Table 5.1.

Table 5.1: Trigger lines used in this analysis and their requirements.

Type of trigger	**Requirements**
L0	**L0MUON:** $p_T(\mu) > 900\,\text{MeV}/c$ **L0SPD:** $n(\text{SPD hits}) > 2$ $E_T(\text{HCAL}) > 240\,\text{MeV}$
HLT1	**Hlt1BBMicroBiasVelo:** $n(\text{Velo Tracks}) \geq 1$ **Hlt1DiMuonHighMass:** $m(\mu^+\mu^-) > 2.7\,\text{GeV}/c^2$

5.3.2 Offline Selection

In order to select low activity events, the number of SPD hits is required to be less than 20. A VELO track passes only through this detector and is typically a large-angle track. The number of VELO tracks (nVeloTracks) with DOCA $< 1\,\text{mm}$ is required to be equal to 2. Here DOCA refers to the distance of closest approach between the Velo track and the J/ψ decay vertex. The reason for this cut is due to the presence of a residual electron contamination from PbPb $\rightarrow$ Pb e^+e^- Pb events.

The coherent J/ψ candidates are selected by requiring two long tracks identified as muons with transverse momentum $p_T > 500\,\text{MeV}/c$. Both muons have to be in the

pseudo-rapidity range $2.0 < \eta < 4.5$. In addition, the dimuon system must have a transverse momentum smaller than $1\,\mathrm{GeV}/c$ and invariant mass within $65\,\mathrm{MeV}/c^2$ of the PDG J/ψ mass value $(3096.916 \pm 0.011)\,\mathrm{MeV}/c^2$ [2]. This invariant mass window is chosen in order to select events around 2σ where σ is the standard deviation found in the mass fit performed in the Section 5.5. As about two thirds of the data include information from beam-gas interactions (Pb-Ar collisions), the bunch-crossing type (BCType) "Beam-Beam" was required. However, it has been shown that there can still be residual Pb-Ar interactions. Only exclusively produced J/ψ could be a potential contamination. This is expected to be marginal considering the factor ~ 10 in center-of-mass energy between the two type of colliding systems. The dimuon p_T^2 and mass spectra after trigger and offline selections are represented in Figures 5.1 and 5.2 respectively.

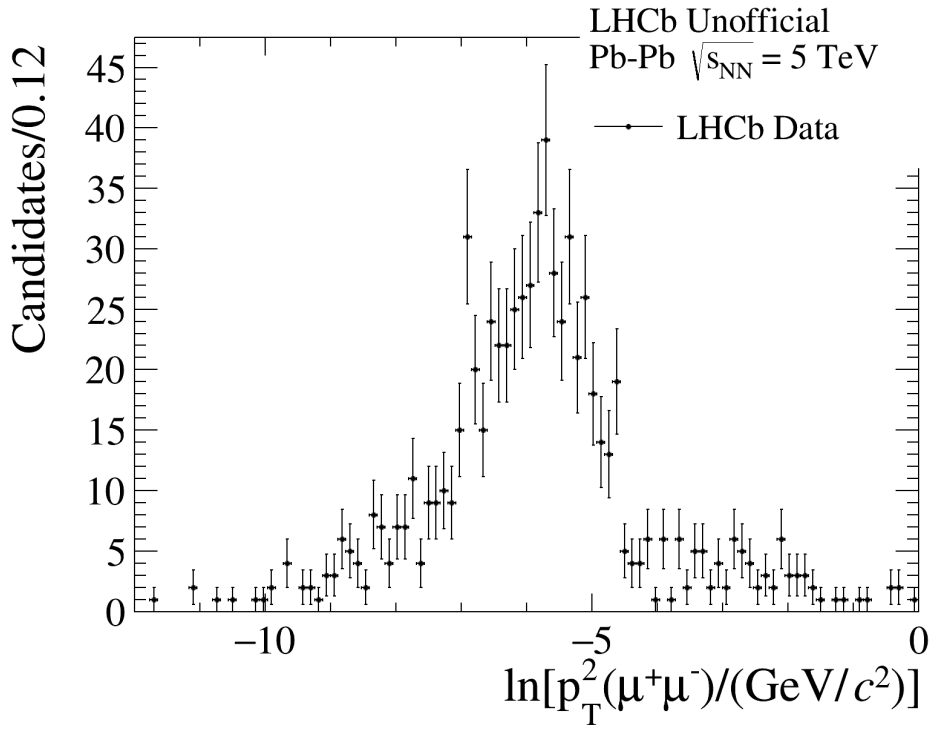

Figure 5.1: Plot of $\ln[p_T^2(\mu^+\mu^-)/(\mathrm{GeV}/c)^2]$ using LHCb 2015 data after trigger and offline selections.

Table 5.2: Offline selection criteria used in the J/ψ production in UPC analysis.

Property	**Criterion**
SPD multiplicity	$n(\text{SPD hits}) < 20$
Transverse momentum (both muon candidates)	$p_T(\mu^{\pm}) > 500\,\text{MeV}/c$
Transverse momentum (dimuon candidate)	$p_T(\mu^+\mu^-) < 1\,\text{GeV}/c$
Invariant mass (dimuon candidate)	$\lvert m(\mu^+\mu^-) - m(J/\psi)\rvert < 65\,\text{MeV}/c^2$

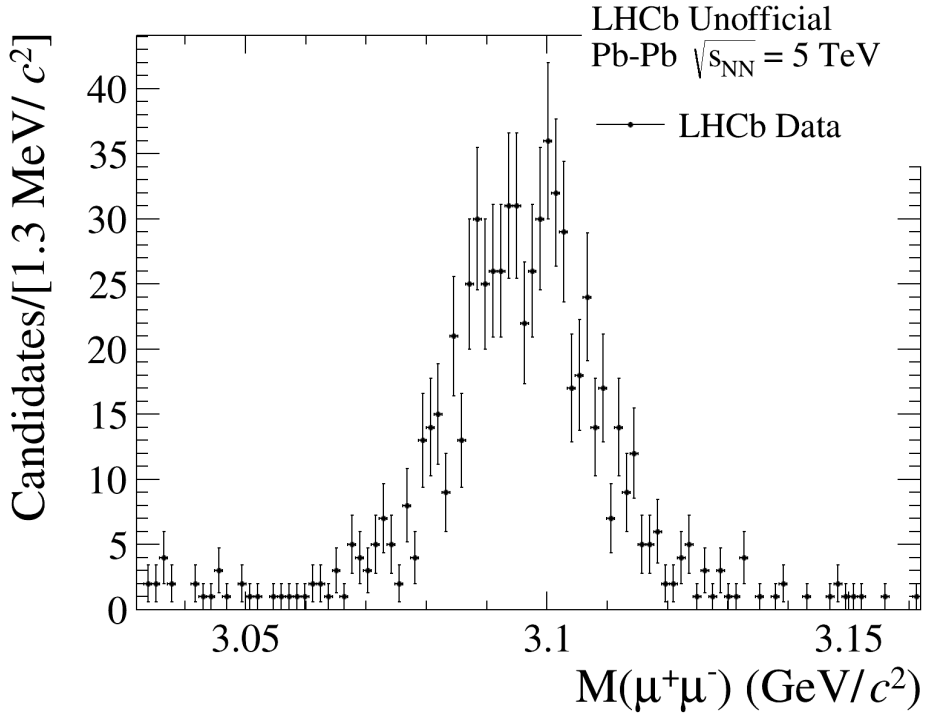

Figure 5.2: Plot of $M(\mu^+\mu^-)$ using LHCb 2015 data after trigger and offline selections.

5.4 Selection efficiency

For each J/ψ rapidity bin, the total efficiency ε_y can be factorized in several factors and be written as:

$$\varepsilon_y = \varepsilon_{geom.acc} \cdot \varepsilon_{track} \cdot \varepsilon_{mu.acc} \cdot \varepsilon_{muonID} \cdot \varepsilon_{offline} \cdot \varepsilon_{trigger} \cdot f_{rec}, \tag{5.2}$$

where $\varepsilon_{geom.acc}$ is the geometrical acceptance efficiency, ε_{track} is the track reconstruction efficiency, $\varepsilon_{mu.acc}$ is the muon chamber acceptance efficiency, ε_{muonID} is the muon identification efficiency, $\varepsilon_{offline}$ is the offline selection (Table 5.2) efficiency, $\varepsilon_{trigger}$ corresponds

for the trigger efficiency and f_{rec} is a scale factor introduced in order to correct for the discrepancies observed between data and simulation. Except for the HLT1 efficiency, all the other efficiencies are determined using SuperChic samples defined previously in Section 5.2.

The geometrical acceptance efficiency is defined as the fraction of events where both muon tracks are within the pseudorapidity range of LHCb out of the total number of generated events. The tracking reconstruction efficiency is defined as the fraction of events with both tracks reconstructed as long tracks out of the number of events with both muons inside the fiducial acceptance region. The muon chamber acceptance efficiency is defined as the fraction of events with both tracks within the muon chamber acceptance out of the number of events with two reconstructed tracks. The muon identification efficiency is defined as the fraction of events with both tracks in muon chamber acceptance identified as muons out of the number of events with both tracks in muon chamber acceptance. The offline selection efficiency is defined as the number of J/ψ candidates with both muons passing the offline selection out of the number of events with both tracks identified as muons. The trigger efficiency is defined as the fraction of J/ψ candidates passing the trigger requirements out of the number of events that passed the offline selection criteria. The trigger efficiency is determined in two steps, in the first step the L0 trigger efficiency is calculated and the HLT1 efficiency is determined in the second step. The efficiency of geometrical acceptance, track reconstruction, muon chamber acceptance, muon identification and L0 trigger are shown in the Table 5.3.

The offline selection is very loose and therefore highly efficient. There is no inefficiency due to the $p_T(\mu^+\mu^-) < 1\,\mathrm{GeV}/c$ criterion. The remaining cuts (mass window, $p_T(\mu^\pm) > 500\,\mathrm{MeV}/c$ and $n(\mathrm{SPD\,hits}) < 20$) combined yield a selection efficiency of:

$$\varepsilon_{offline} = (95.4 \pm 3.2)\% \tag{5.3}$$

The `LOMUON` efficiency is determined using simulated events of the SuperChic sample

Table 5.3: Efficiency of geometrical acceptance, track reconstruction, muon chamber acceptance, muon identification and trigger and the scale factor in bins of J/ψ rapidity.

J/ψ y bin	2.0-2.5	2.5-3.0	3.0-3.5	3.5-4.0	4.0-4.5
$\varepsilon_{geom.acc}$	0.211 ± 0.003	0.539 ± 0.004	0.727 ± 0.004	0.557 ± 0.004	0.212 ± 0.004
ε_{track}	0.742 ± 0.011	0.84 ± 0.01	0.886 ± 0.005	0.919 ± 0.005	0.91 ± 0.01
$\varepsilon_{mu.acc}$	0.770 ± 0.008	0.892 ± 0.004	0.869 ± 0.004	0.805 ± 0.005	0.747 ± 0.01
ε_{muonID}	0.980 ± 0.003	0.958 ± 0.004	0.939 ± 0.003	0.928 ± 0.003	0.902 ± 0.008
ε_{L0}	0.861 ± 0.011	0.854 ± 0.007	0.841 ± 0.005	0.876 ± 0.006	0.853 ± 0.010
ε_{HLT}	0.836 ± 0.002	0.904 ± 0.001	0.925 ± 0.001	0.925 ± 0.001	0.905 ± 0.002
f_{rec}	1.025 ± 0.037	0.97 ± 0.02	0.929 ± 0.017	0.914 ± 0.018	0.910 ± 0.026

although calibrated with data selected by the `L0SPD` line (n(SPD hits) > 2). The spectra of $p_T(\mu^{\pm})$ and $\eta(\mu^{\pm})$ of SuperChic sample are weighted in order to match the same spectra in data samples. The L0 efficiency is then determined using the weighted simulated sample. The results are represented in the Table 5.3 in bins of J/ψ rapidity. The HLT efficiency is measured in data using J/ψ candidates by requiring at least one Velo track (`Hlt1BBMicroBiasVelo`).

The efficiency of geometrical acceptance, muon identification, track reconstruction, muon chamber acceptance and L0 trigger are determined using simulated events. Those numbers are corrected for the discrepancy between data-driven methods and simulation through a scale factor f_{rec}, determined from the single particle efficiencies measured in data and simulation. f_{rec} is defined as ratio of the single particle efficiencies in data and simulation in each bin of rapidity as :

$$f^{y}_{rec} = \Sigma_{ij} w^{ij}_{geom.acc} w^{ij}_{L0} w^{ij}_{track} w^{ij}_{muonID} \phi(k,i,j), \tag{5.4}$$

where w^{ij}_{eff} are the weights computed as

$$w^{\eta_1\eta_2}_{eff} = \frac{\varepsilon^{data}(\eta^i_1)\varepsilon^{data}(\eta^j_2)}{\varepsilon^{sim}(\eta^i_1)\varepsilon^{sim}(\eta^j_2)} \tag{5.5}$$

For each efficiency , $\phi(k,i,j)$ is the physics function which gives the fraction of events having two tracks in the pseudo-rapidity bin i,j that produces a meson in rapidity bin k. f_{rec} values are listed in Table 5.3.

5.5 Signal extraction

In order to extract the number of coherent J/ψ mesons a fit to the natural logarithm of the squared transverse momentum $\ln(p_T^2)$ spectrum of J/ψ candidates is performed. The following two main sources of background are considered:

- the dimuon continuum coming from the decay channel $\gamma\gamma \to \mu^+\mu^-$,
- the incoherent J/ψ background.

A first fit to the invariant mass of the dimuon candidates allows to determine the number of dimuons originating from $\gamma\gamma \to \mu^+\mu^-$ in the J/ψ peak. Then, for candidates within J/ψ peak, the yields of coherent and incoherent J/ψ are determined from a fit to the p_T^2 of the J/ψ candidate.

A double-sided Crystal Ball function [80] is used to account for both J/ψ and $\psi(2S)$ contributions to the dimuon invariant mass distribution. The $\psi(2S)$ function shape parameters are constrained to be identical to the ones for J/ψ. The non-resonant dimuon contribution is parameterised by a exponential multiplied by a first degree polynomial, $e^{a \cdot m(\mu\mu)} \cdot (p_0 + p_1 \cdot m(\mu\mu))$ where all parameters are free to vary. The yield of each contribution is free to vary. The number of $\gamma\gamma$ events is obtained by integrating over the mass range $3032 < m(\mu^+\mu^-) < 3162\,\mathrm{MeV}/c^2$ and it will be used later as an input for the fit of the p_T^2 distribution. The procedure is repeated for all rapidity bins. An example of the fit to the invariant mass can be found in Figure 5.3.

A fit on the candidate p_T^2 for candidates in the mass window $3032 < m(\mu^+\mu^-) < 3162\,\mathrm{MeV}/c^2$ is performed to distinguish between the coherent and the incoherent photoproduced J/ψ since J/ψ candidates have characteristically low transverse momentum p_T in UPC. The fit function is given by :

$$F(\ln p_T^2) = n_{\mathrm{coh}} \cdot T_{\mathrm{coh}} + n_{\mathrm{incoh}} \cdot T_{\mathrm{incoh}} + n_{\gamma\gamma} \cdot T_{\gamma\gamma} \tag{5.6}$$

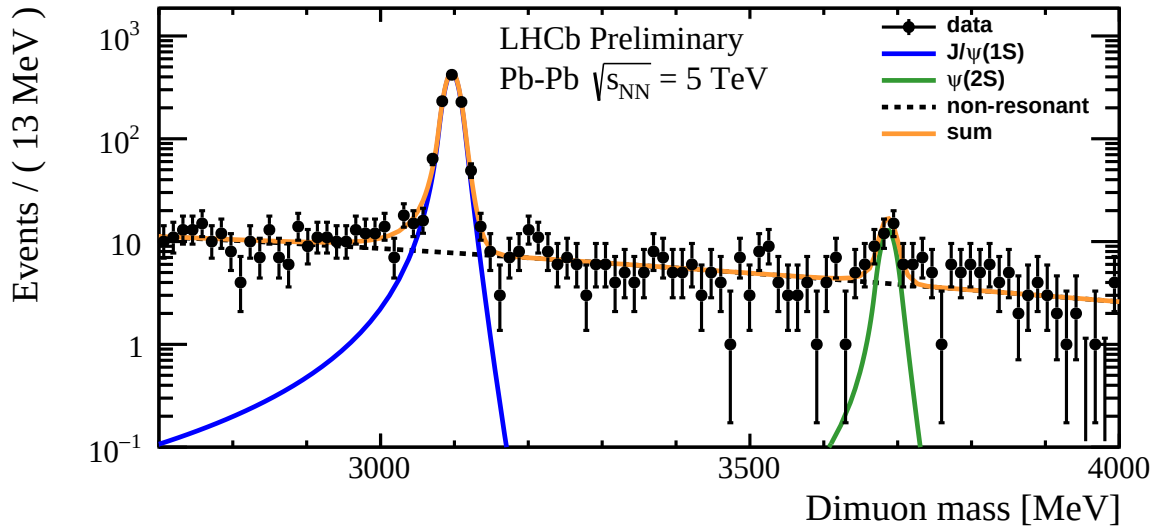

Figure 5.3: Invariant mass fit to determine the fractions of $J\psi$, $\psi(2S)$ and non-resonant events in the full J/ψ rapidity range.

where $T_{\text{coh}}, T_{\text{incoh}}, T_{\gamma\gamma}$ are the shapes of p_T distribution obtained from STARlight simulation at the generator level, requiring the two muons from the simulated J/ψ decay to be within the pseudorapidity range $2.0 < \eta_{\mu^\pm} < 4.5$ corresponding to a meson rapidity range of $2.0 < y(J/\psi) < 4.5$, $n_{\text{coh,incoh}}$ are the yields of coherent and incoherent contribution and $n_{\gamma\gamma}$ is constrained to be maximum 1 $\sigma_{non-res}$ away from $n_{non-res}$, the dimuon continuum yield value obtained in the dimuon invariant mass fit.

Prior to the fit, all MC models, $T_{\text{coh}}, T_{\text{incoh}}, T_{\gamma\gamma}$, are smeared using smearing factors to mimic the detector response. The templates are corrected for resolution effects using the following formula:

$$\vec{p_\mu} = G(p_x, 10\,\text{MeV}/c)\vec{e_x} + G(p_y, 10\,\text{MeV}/c)\vec{e_y} + G(p_z, 10\,\text{MeV}/c)\vec{e_z} \tag{5.7}$$

where $\vec{p_\mu}$ denotes the 3-momentum vector of the decay muons and $G(\mu, \sigma)$ a sample from a Gaussian distribution. This procedure is done 1000 times per event. For each randomised procedure, the event is accepted if both muons have pseudorapidity between $2.0 < \eta < 4.5$ and the invariant mass $m(\mu^+\mu^-)$ is in the range $2 < m(\mu^+\mu^-) < 4\,\text{GeV}/c^2$. The resolution of $10\,\text{MeV}/c$ for the p_x and the p_y component matches approximately $14.3\,\text{MeV}/c$ mass resolution when the mass resolution is taken as a proxy for the p_T resolution. It has

been checked that the uncertainty on the $\gamma\gamma$ continuum parametrisation that enters to the templates is negligible. Fits are performed as a maximum likelihood fit to the $\ln(p_T^2)$ spectrum. An example is shown 5.4. The signal yield in bins of J/ψ rapidity is described in Table 5.4.

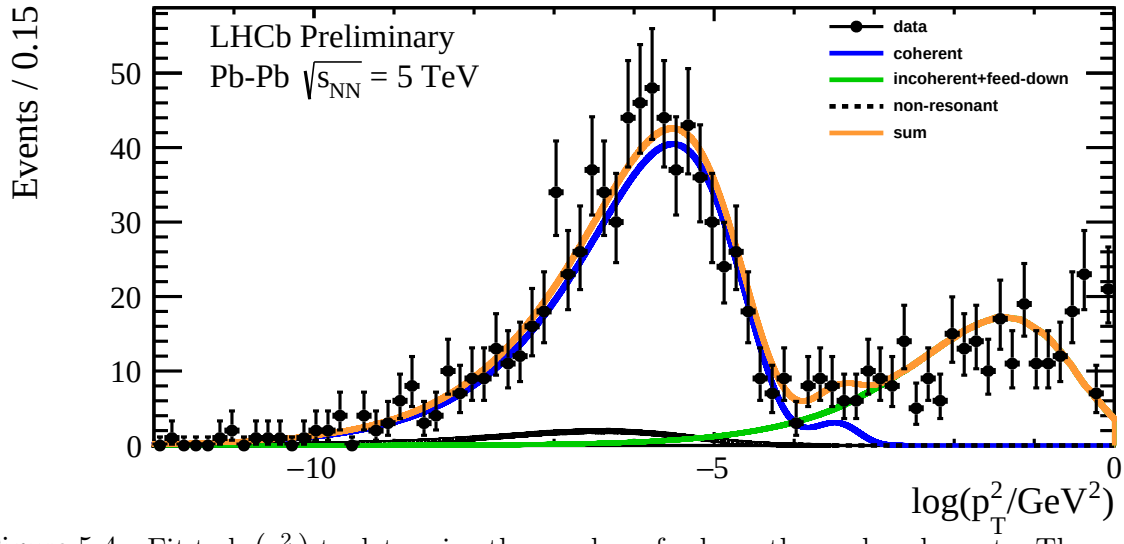

Figure 5.4: Fit to $\ln(p_T^2)$ to determine the number of coherently produced events. The number of non-resonant events is obtained from the invariant mass fit and fixed in this fit. The blue line is the coherently production template, the green line is the sum of the incoherent and feed-down templates, the black line is the non-resonant template and the orange line represents the sum of all templates.

Table 5.4: Signal yield in bins of J/ψ rapidity.

J/ψ y bin	2.0-2.5	2.5-3.0	3.0-3.5	3.5-4.0	4.0-4.5
n_{coh}	76 ± 9	217 ± 16	249 ± 17	141 ± 12	29 ± 6

5.6 Results

In order to determine the binned cross-section, the Equation 5.1 is calculated using the efficiencies and signal yields from the previous sections. The integrated luminosity of the data set, $\mathcal{L}$, is determined to be $(10.12 \pm 1.31)\,\mu\text{b}^{-1}$. The luminosity has been determined using a subset of the data where a beam profile imaging and a van der Meer scan [77] has been performed. An extrapolation method is applied to calculate $\mathcal{L}$ for the whole data set. The cross-section values are showed in Table 5.5.

Table 5.5: Cross-section of UPC J/ψ production in bins of J/ψ rapidity.

J/ψ y bin	2.0-2.5	2.5-3.0	3.0-3.5	3.5-4.0	4.0-4.5
$\frac{d\sigma}{dy}(mb)$	3.03 ± 0.18	2.60 ± 0.09	2.28 ± 0.08	1.73 ± 0.08	1.10 ± 0.11

5.6.1 Systematic uncertainties

Systematic uncertainties in the measured cross-section are related to the determination of the muon reconstruction and selection efficiencies, the trigger efficiency, the muon momentum smearing, the mass fit signal model and the modelling of the feed-down background. They are described below and summarised in Table 5.6.

Table 5.6: Relative systematic uncertainties considered for the cross-section measurement of coherent J/ψ production. The first two contributions are taken from [79]

Source	**Relative uncertainty (%)**
Reconstruction efficiency	2.1-4.5
Selection efficiency	3.2
Hardware trigger efficiency	3.0
Software trigger efficiency	1.6-5.3
Momentum smearing	3.3
Mass fit model	3.9
Feed-down background	5.8
Branching Fraction	0.6
Luminosity	13.0

The largest uncertainty comes from the integrated luminosity determination due to the small data set and the extrapolation method employed. The branching fraction uncertainty is taken from [2].

The systematic uncertainties related to the J/ψ reconstruction efficiency are taken from [79]. They include uncertainties on the track reconstruction, muon identification and selection efficiencies.

The efficiency of the L0 trigger is determined from simulated events. It is compared to the efficiency obtained with a data-driven method on a smaller data sample selected by min-bias trigger path, and the difference taken as systematic uncertainty. The smaller data sample used is compounded by the selected by `L0SPD`, `Hlt1DiMuonHighMass` and

`Hlt1BBMicroBiasVelo`. The statistical uncertainties from the HLT1 efficiency determination determine the systematic uncertainty.

The systematic uncertainties related to the efficiencies of the requirement on the multiplicity of SPD deposits and on the muon p_T are estimated by assuming that the all events failing these requirements can be either background or signal. The systematic uncertainty related to the dimuon mass efficiency is taken from the error of the integral of the double-sided Crystal Ball function. The VELO track multiplicity requirement is found to be 100% efficient and no uncertainty is assigned.

The signal and background templates used in the $\ln(p_T^2)$ fit are affected by the *ad-hoc* momentum smearing. An alternative smearing model is performed varying the smearing factor with the muon p_T instead of the muon momentum.

The systematic uncertainty associated to the signal model in the fit to the dimuon mass spectrum is assessed using an alternative model. A single-sided Crystal Ball function is used for the signal and the difference in the signal yields with respect to the nominal fit is assigned as systematic uncertainty.

Since there is no dedicated template distribution for the feed-down background in the $\ln(p_T^2)$ fit, a systematic uncertainty is evaluated. The J/ψ candidate selection is modified in order to allow for two additional opposite-sign tracks that are consistent with originating from a mixture of coherent and incoherent production of $\psi(2S) \to J/\psi\pi^+\pi^-$. After requiring the reconstructed mass of the $\psi(2S)$ candidates to be within 65 MeV of the known $\psi(2S)$ mass, 22 candidates are observed. Using the ratio between 22 and the number of observed $\psi(2S) \to \mu^+\mu^-$, 78.5 ± 3.1 J/ψ mesons are expected to come from $\psi(2S) \to J/\psi X$ feed-down. Assuming that half of these candidates may be included the signal yield, a systematic uncertainty of 5.8% is assigned.

5.6.2 Comparison to theory predictions

The results are compared to several theoretical predictions [51, 52, 53, 54, 55] for the coherent J/ψ production in PbPb collisions at $\sqrt{s_{\rm NN}} = 5\,\text{TeV}$. The main differences between the models used to make the predictions originate from the way the photonuclear interaction is treated, as explained in Section 2.3. The present results are well described by all models.

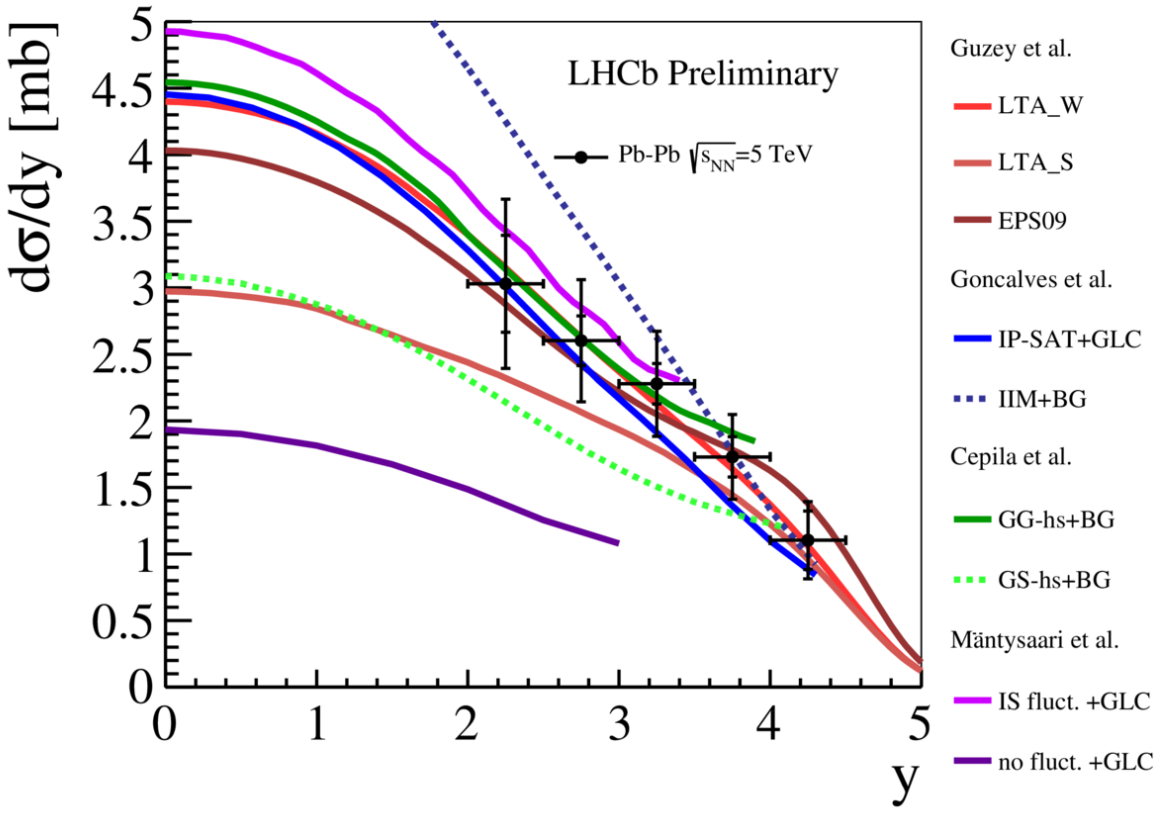

Figure 5.5: Differential cross-section for coherent J/ψ production compared to different phenomenological predictions. The labels used to identify each model are explained in Section 2.3. The LHCb measurements are shown as points, where inner and outer uncertainties represent the statistical and the total errors respectively.

5.7 Updated measurement

In this section an update of the measured cross-section is presented. This update comprises the use of full reconstructed STARlight samples used in order to perform the fits, the inclusion of an individual template for the feed-down contribution in the fits and the addition of a selection step based on the HeRSCheL detector [70]. The results described in the Section 5.6 do not exploit the capabilities of the HeRSCheL's FOM, defined in Equation 3.1.

As it was described in Section 3.2.9, HeRSCheL is a set of plastic scintillators used in order to detect any activity in high pseudorapidity range, typically $\eta \gtrapprox 8$. The absence of detector activity in this range evince the presence of rapidity gaps thus indicating a typical coherent production and improving the quality of the cross-section measurement. In the next sections we describe the steps needed to choose the requirement on the HeRSCheL's FOM and the determination of the efficiency of this selection. A preliminary result of the cross-section measurement in this new scenario is presented.

5.7.1 HeRSCheL requirement

In order to choose the requirement on the HeRSCheL (HRC) variable, $\ln(\chi^2_{\mathrm{HRC}})$, an enriched sample on exclusive non-resonant dimuon production is used. The sample selection is described in Table 5.7. It is expected that the distributions of $\ln(\chi^2_{\mathrm{HRC}})$ for the exclusive non-resonant dimuon production and for the coherent J/ψ production are the same.

An enriched incoherent J/ψ sample is used to illustrate the discrimination power of $\ln(\chi^2_{\mathrm{HRC}})$. The selection of this sample is described in Table 5.8. The requirement $\ln[p_T^2(\mu^+\mu^-)/(\mathrm{GeV}/c)^2] > -2$ removes a large fraction of the coherent J/ψ production.

Figure 5.6 shows the distribution of $\ln(\chi^2_{\mathrm{HRC}})$ for both samples. A clear peak around $\ln(\chi^2_{\mathrm{HRC}}) \approx 6.5$ can be observed and it vanishes completely before $\ln(\chi^2_{\mathrm{HRC}}) = 7.0$. There-

fore, we decided to apply the requirement $\ln(\chi^2_{\text{HRC}}) < 7$.

Table 5.7: Selection applied on LHCb 2015 data to obtain enriched non-resonant sample.

Property	**Criterion**
L0 trigger	`L0MUON`
HLT1 trigger	`Hlt1BBMicroBiasVelo`
Muon ID (both muon candidates)	True
n(SPD hits)	< 20
n(Long tracks)	$= 2$
Pseudorapidity (both muon candidates)	$2 < \eta < 4.5$
Transverse momentum (both muon candidates)	$p_T(\mu^{\pm}) > 500\,\text{MeV}/c$
Dimuon invariant mass	$m(\mu^+\mu^-) < 2.7\,\text{GeV}/c^2$
Transverse momentum (dimuon candidate)	$\ln[p_T^2(\mu^+\mu^-)/(\text{GeV}/c)^2] < -5$

Table 5.8: Selection applied on LHCb 2015 data to obtain enriched incoherent J/ψ sample.

Property	**Criterion**
L0 trigger	`L0MUON`
HLT1 trigger	`Hlt1BBMicroBiasVelo`
Muon ID (both muon candidates)	True
n(SPD hits)	< 20
n(Long tracks)	$= 2$
Pseudorapidity (both muon candidates)	$2 < \eta < 4.5$
Transverse momentum (both muon candidates)	$p_T(\mu^{\pm}) > 500\,\text{MeV}/c$
Dimuon invariant mass (dimuon candidate)	$\lvert m(\mu^+\mu^-) - m(J/\psi)\rvert < 65\,\text{MeV}/c^2$
Transverse momentum (dimuon candidate)	$\ln[p_T^2(\mu^+\mu^-)/(\text{GeV}/c)^2] > -2$

5.7.2 HeRSCheL selection efficiency

The efficiency of the HeRSCheL selection requirement for the coherent J/ψ production is expected to be the same as for the non-resonant exclusive production. The HRC selection is not expected to be fully efficient as it can be seen in Figure 5.6. A fraction of the enriched exclusive non-resonant sample is rejected by the selection $\ln(\chi^2_{\text{HRC}}) < 7$ since some events are observed around $\ln(\chi^2_{\text{HRC}}) \approx 9$. This efficiency is determined using three approaches described on the following sections.

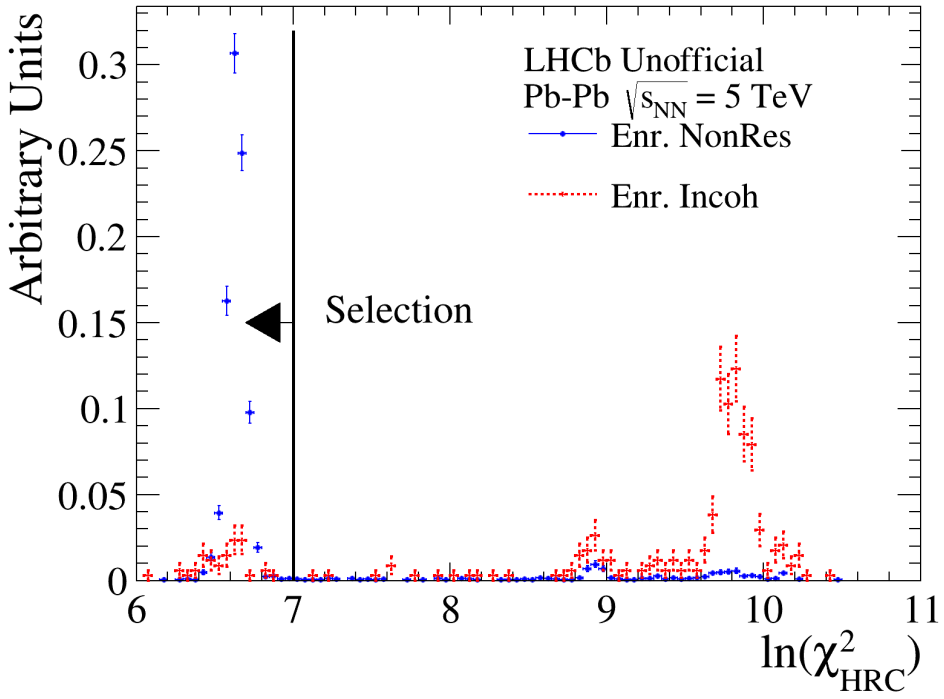

Figure 5.6: $\ln(\chi^2_{\rm HRC})$ using enriched non-resonant and incoherent samples. The HRC selection for this analysis is defined by $\ln(\chi^2_{\rm HRC}) < 7$.

Non-Resonant Sample Fit

Initially the efficiency could be simply determined using the number of candidates before and after the selection, $\varepsilon = N_{\rm after}/N_{\rm before}$, where the N's are obtained simply by counting candidates in the non-resonant sample. However there is an irreducible incoherent contamination in data. The method used in this context is to discriminate between these two contributions using a fit to distributions which are expected to have different models for the coherent and incoherent contributions.

Mass distribution fits are commonly used in this scenario, although it is not suitable in this case because we are dealing with non-resonant candidates. On the other hand, as exploited in the Section 5.5, $\ln[p_T^2(\mu^+\mu^-)/({\rm GeV}/c)^2]$ variable discriminates coherent and incoherent candidates and there are available fit models for both samples.

As the goal becomes to perform fits to the $\ln[p_T^2(\mu^+\mu^-)/({\rm GeV}/c)^2]$ distribution to dis-

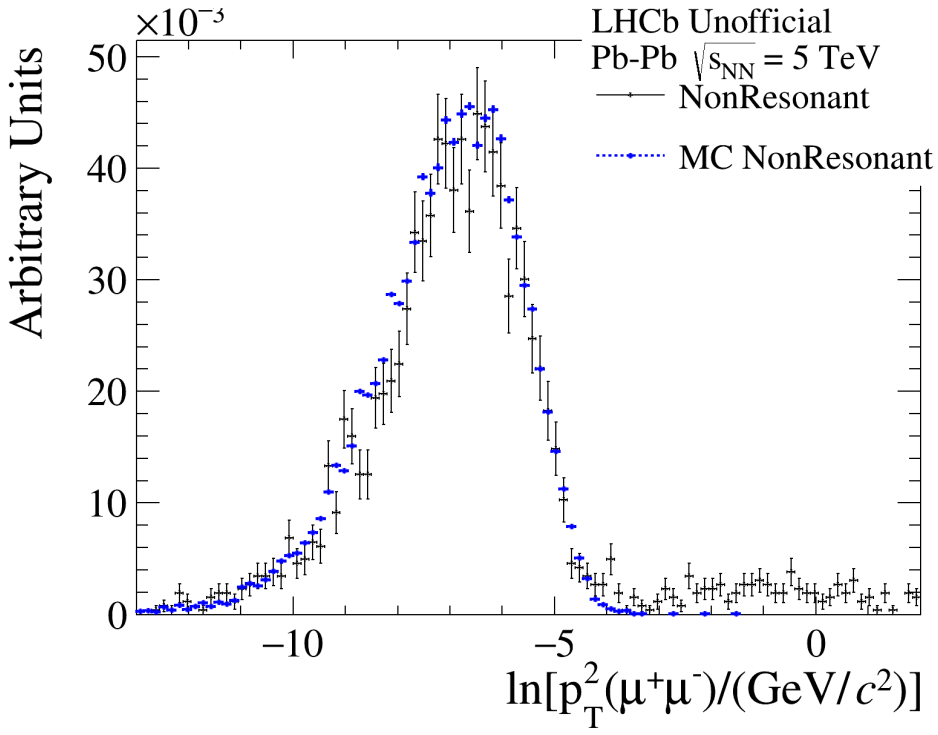

Figure 5.7: Plot of $\ln[p_T^2(\mu^+\mu^-)/(\mathrm{GeV}/c)^2]$ using LHCb 2015 data and simulated sample.

criminate high-p_T (incoherent) and low-p_T (coherent) contributions, a sample with both contributions is needed. Non-resonant sample is selected by the cuts described in Table 5.7 except for the $\ln[p_T^2(\mu^+\mu^-)/(\mathrm{GeV}/c)^2] < -5$ selection on last line (enrichment). Monte Carlo of two-photon reactions $\gamma\gamma \to \mu^+\mu^-$ defined on Section 5.2 is used to access a coherent production sample fit model. Both samples are displayed on Figure 5.7. Incoherent non-resonant dimuons contribution is seen from $\ln[p_T^2(\mu^+\mu^-)/(\mathrm{GeV}/c)^2] \approx -4$.

In order to account for the two contributions a sum of two probability density functions (PDF) is used. The signal (coherent) part is represented by a kernel estimator (RooKeysPdf) template derived from simulated events. A single exponential of p_T^2, $e^{-bp_T^2}$, is used to model the background (incoherent) part. There are 3 free parameters on this PDF: N (coherent yield), B (background yield) and b (exponential parameter). The distribution and the fitted PDF are shown on Figure 5.8.

The same fit procedure is performed after the $\ln(\chi^2_{\mathrm{HRC}}) < 7$ selection (see Figure 5.9).

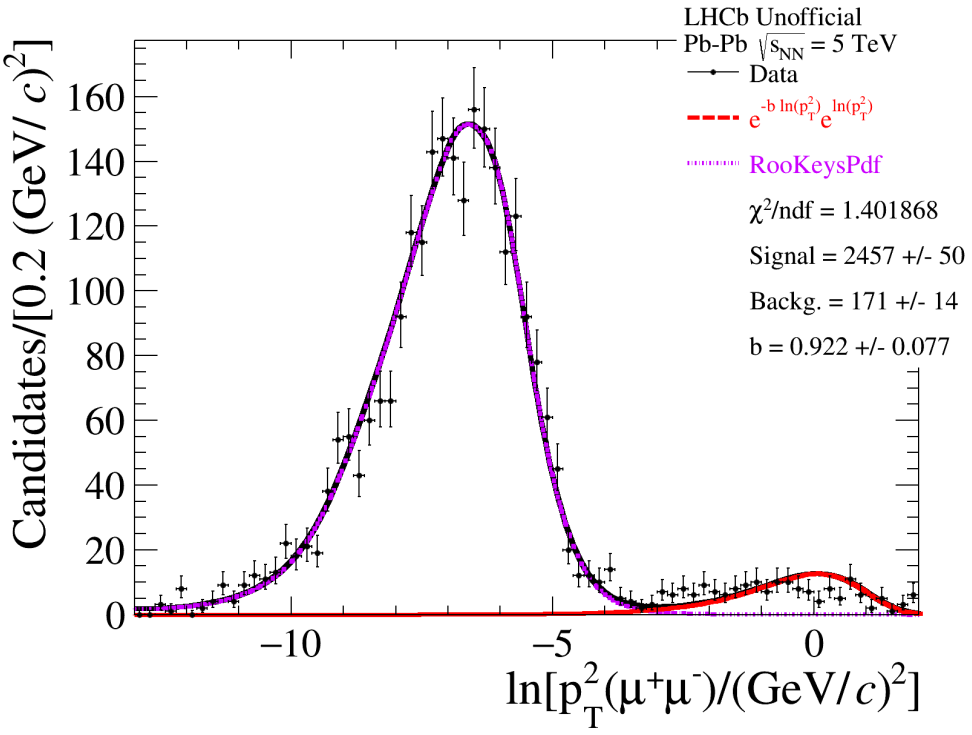

Figure 5.8: Fit of $\ln[p_T^2(\mu^+\mu^-)/(\mathrm{GeV}/c)^2]$ using non-resonant LHCb 2015 data.

In order to determine how many events are rejected by $\ln(\chi^2_{\mathrm{HRC}}) < 7$ a third fit is performed using the inverted selection, $\ln(\chi^2_{\mathrm{HRC}}) > 7$ (see Figure 5.10).

The efficiency can be calculated by

$$\varepsilon(\ln(\chi^2_{\mathrm{HRC}}) < 7) = \frac{N_{\mathrm{passed}}}{N_{\mathrm{passed}} + N_{\mathrm{failed}}} \tag{5.8}$$

and using the yields from Figures 5.9 and 5.10:

$$\boxed{\varepsilon(\ln(\chi^2_{\mathrm{HRC}}) < 7) = (90.03 \pm 0.61)\%}.$$

Efficiency with $\Delta\varphi$ Selection

Comparing the b parameter on the three fits from the previous section a large discrepancy is observed. Nevertheless the background exponential parameter is not expected to vary with the HRC selection i.e. incoherent non-resonant background origin is not changed by the HRC cut.

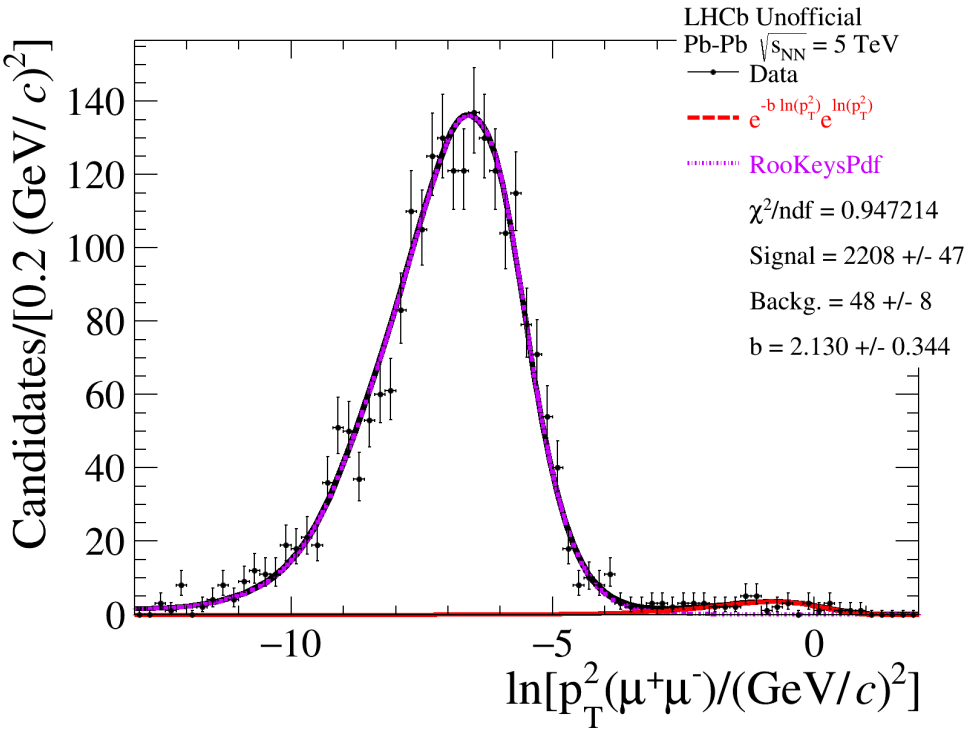

Figure 5.9: Fit of $\ln[p_T^2(\mu^+\mu^-)/(\mathrm{GeV}/c)^2]$ using non-resonant LHCb 2015 data selected by $\ln(\chi^2_{\mathrm{HRC}}) < 7$.

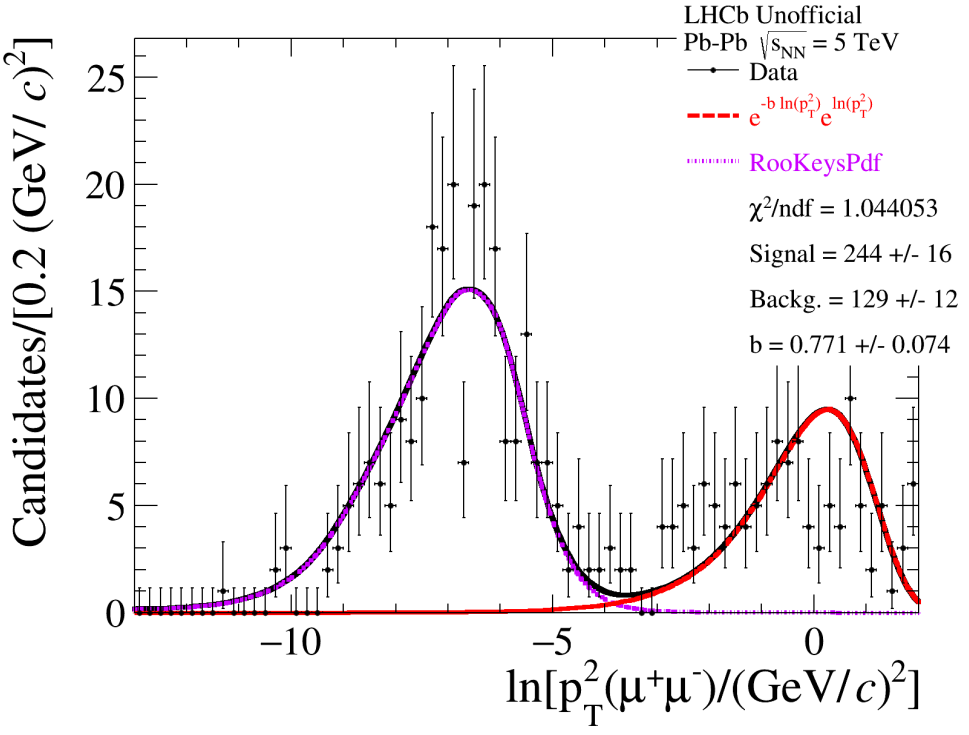

Figure 5.10: Fit of $\ln[p_T^2(\mu^+\mu^-)/(\mathrm{GeV}/c)^2]$ using non-resonant LHCb 2015 data selected by $\ln(\chi^2_{\mathrm{HRC}}) > 7$.

In order to solve this problem a different variable is examined:

$$\Delta\varphi = \left| \frac{\varphi(\mu^+) - \varphi(\mu^-)}{\pi} \right|,$$

where φ is the azimuth angle which is deeply dependent of transverse momentum. In the context of a non-resonant CEP, the transverse momentum of the produced system is expected to be low and than the azimuthal angle between particles must be near of π. Comparing the distribution of this quantity for exclusive non-resonant dimuon sample using LHCb data and MC data, a discrepancy is clear (see Figure 5.11). All MC data is concentrated in the range $\Delta\varphi > 0.9$. Therefore, we opted to apply $\Delta\varphi > 0.9$ requirement on LHCb data.

The same fit procedure is repeated using the non-resonant sample after this cut. The fit without HRC cut is shown in Figure 5.12. After the selection $\ln(\chi^2_{\text{HRC}}) < 7$ another fit is performed (see Figure 5.13). The last one is a fit with the inverted selection $\ln(\chi^2_{\text{HRC}}) > 7$, it is shown in Figure 5.14.

The efficiency is determined using the Eq. 5.8:

$$\boxed{\varepsilon(\ln(\chi^2_{\text{HRC}}) < 7) = (90.09 \pm 0.61)\%}.$$

Fix b Parameter

As it is expected, the b parameter does not vary within the uncertainties in the fits from the previous section. The parameter is fixed to the value found in the no-HRC-cut fit ($b = 4.9762$) for the fits after $\ln(\chi^2_{\text{HRC}}) < 7$ (Figure 5.15) and $\ln(\chi^2_{\text{HRC}}) > 7$ (Figure 5.16).

One more time efficiency is calculated using Eq. 5.8:

$$\boxed{\varepsilon(\ln(\chi^2_{\text{HRC}}) < 7) = (90.10 \pm 0.61)\%}.$$

We use the efficiency calculated above in the cross-section measurement. The difference between the previous calculations are used to estimate a systematic uncertainty of 0.7%.

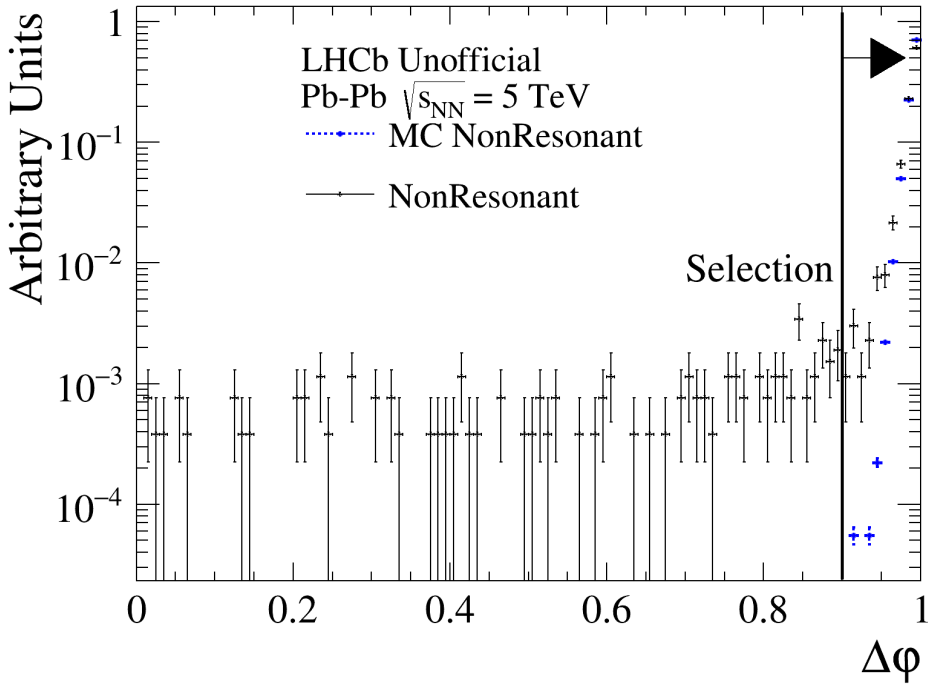

Figure 5.11: $\Delta\varphi$ distribution using both simulated and LHCb data. The vertical line represents the selection $\Delta\varphi > 0.9$ applied.

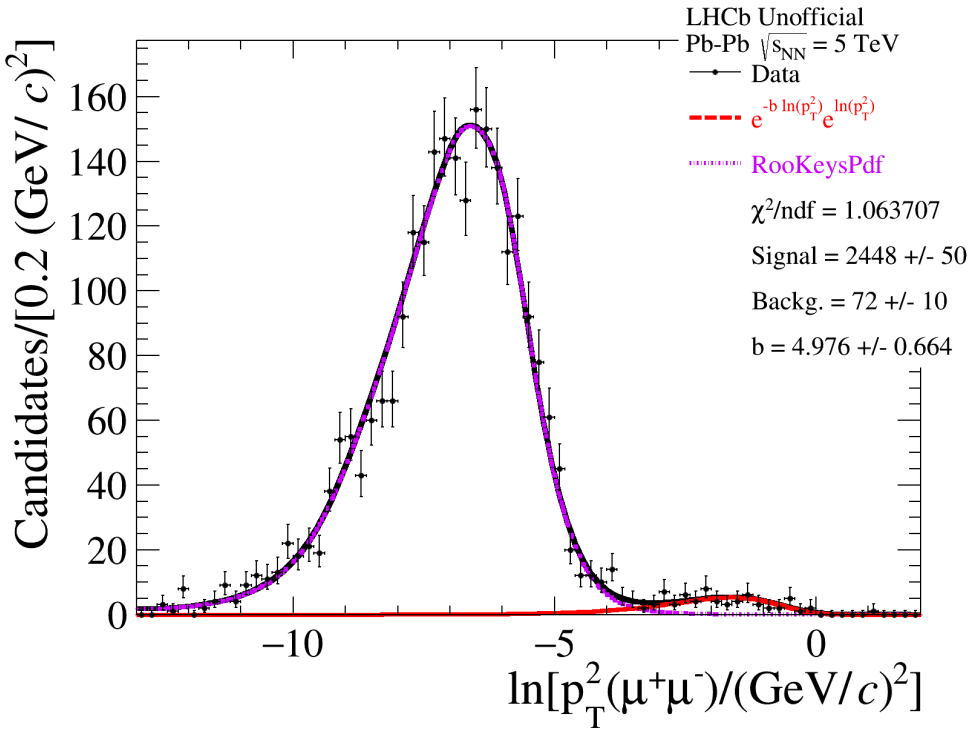

Figure 5.12: Fit of $\ln[p_T^2(\mu^+\mu^-)/(\mathrm{GeV}/c)^2]$ using non-resonant LHCb 2015 data selected by $\Delta\varphi > 0.9$.

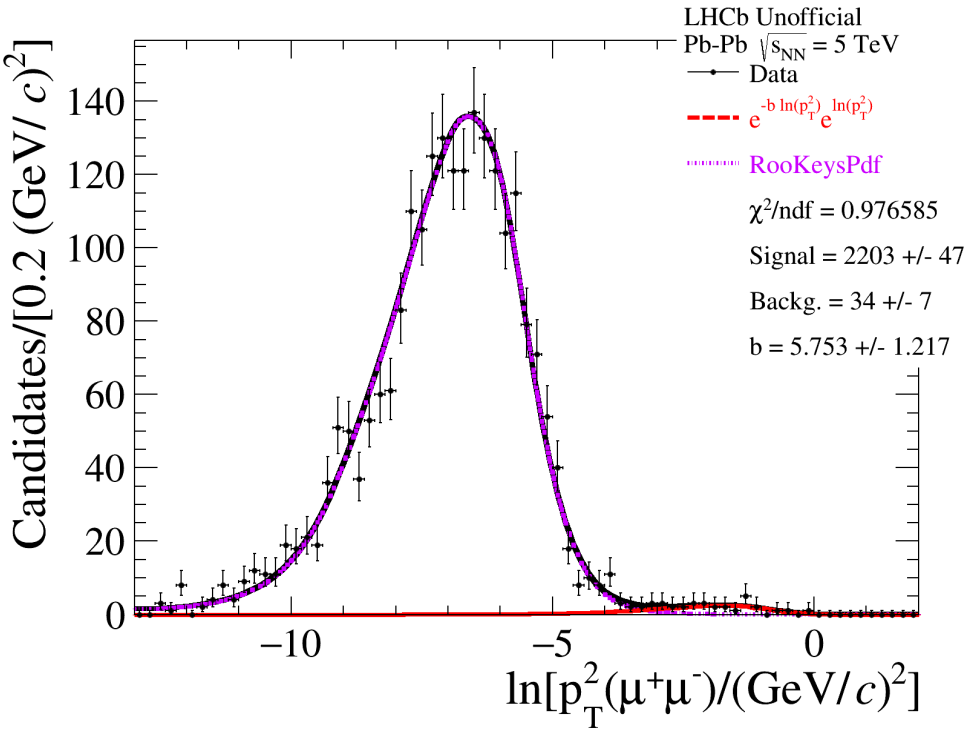

Figure 5.13: Fit of $\ln[p_T^2(\mu^+\mu^-)/(\mathrm{GeV}/c)^2]$ using non-resonant LHCb 2015 data selected by $\Delta\varphi > 0.9$ and $\ln(\chi^2_{\mathrm{HRC}}) < 7$.

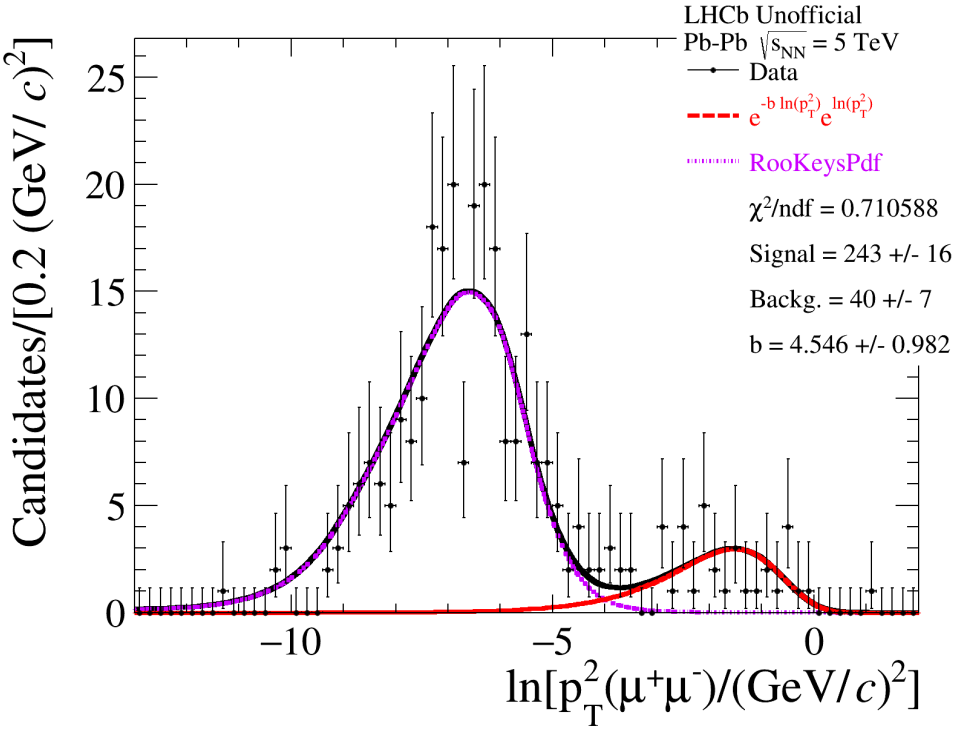

Figure 5.14: Fit of $\ln[p_T^2(\mu^+\mu^-)/(\mathrm{GeV}/c)^2]$ using non-resonant LHCb 2015 data selected by $\Delta\varphi > 0.9$ and $\ln(\chi^2_{\mathrm{HRC}}) > 7$.

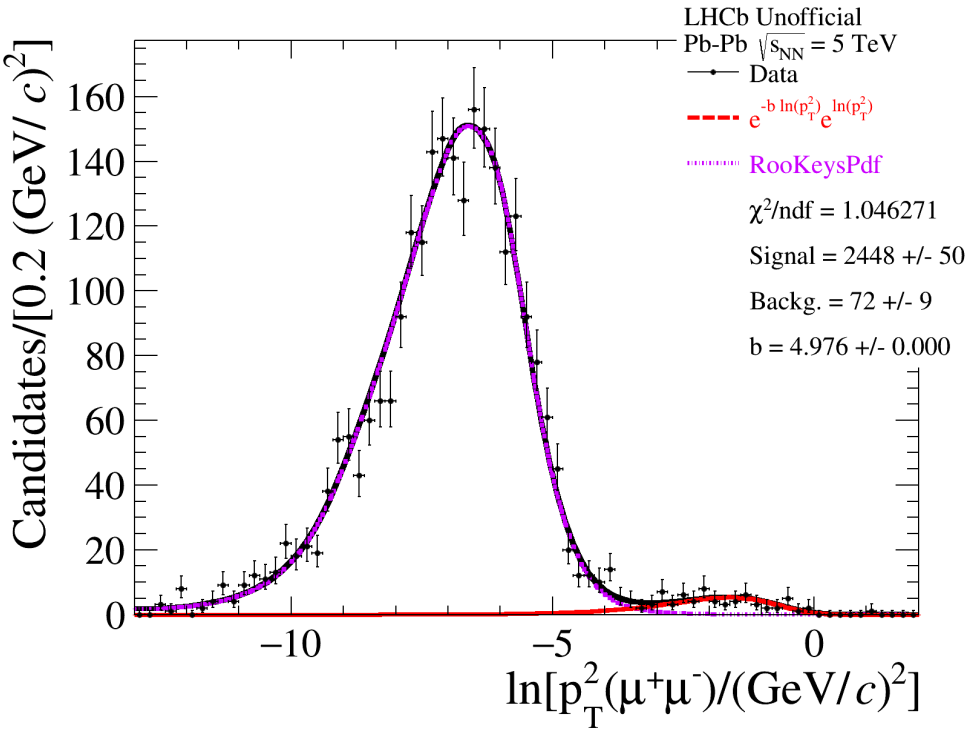

Figure 5.15: Fit of $\ln[p_T^2(\mu^+\mu^-)/(\mathrm{GeV}/c)^2]$ using non-resonant LHCb 2015 data selected by $\Delta\varphi > 0.9$ and $\ln(\chi^2_{\mathrm{HRC}}) < 7$ fixing the b parameter.

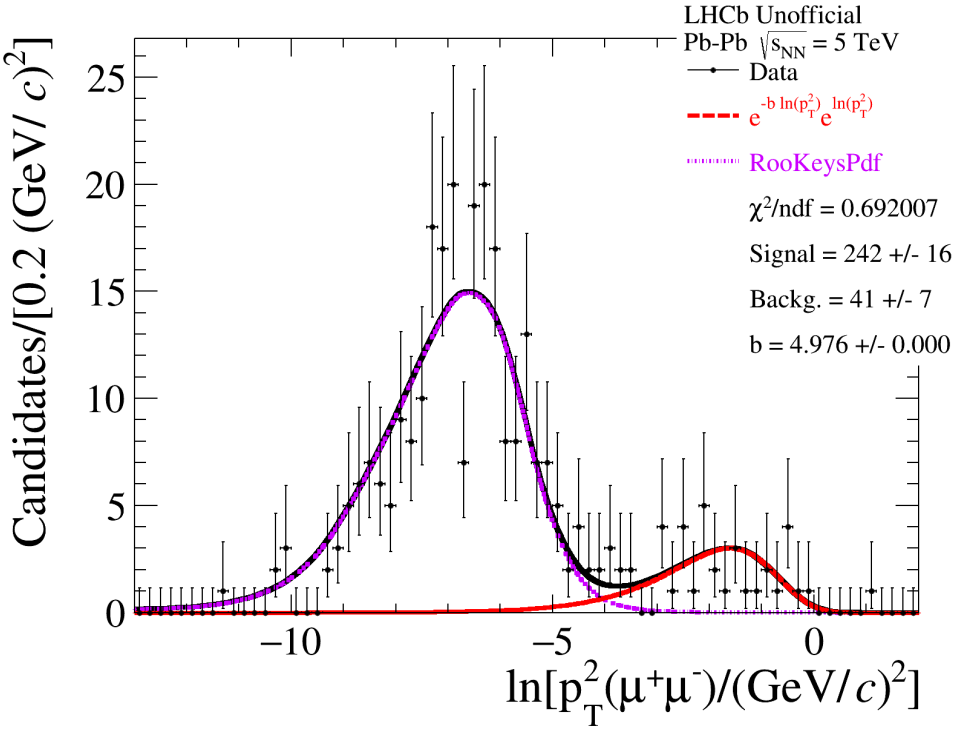

Figure 5.16: Fit of $\ln[p_T^2(\mu^+\mu^-)/(\mathrm{GeV}/c)^2]$ using non-resonant LHCb 2015 data selected by $\Delta\varphi > 0.9$ and $\ln(\chi^2_{\mathrm{HRC}}) > 7$ fixing the b parameter.

5.7.3 Updated cross-section measurement

In order to measure the cross-section in bins of J/ψ rapidity the main equation,

$$\frac{\mathrm{d}\sigma_{\mathrm{coh}}}{\mathrm{d}y} = \frac{n_{\mathrm{coh}}}{\varepsilon_y \cdot \Delta y \cdot \mathcal{L} \cdot \mathcal{B}}, \tag{5.9}$$

is evaluated using the updated efficiency,

$$\varepsilon_y = \varepsilon_{geom.acc} \cdot \varepsilon_{track} \cdot \varepsilon_{mu.acc} \cdot \varepsilon_{muonID} \cdot \varepsilon_{offline} \cdot \varepsilon_{trigger} \cdot \varepsilon_{hrc} \cdot f_{rec}, \tag{5.10}$$

where all efficiencies per bin are the same from the previous measurement except for the HeRSCheL efficiency, $\varepsilon_{hrc} = (90.10 \pm 0.61)\%$ measured in the previous section and assumed to be uniform across all bins. The integrated luminosity, $\mathcal{L} = (10.12 \pm 1.31)\mu\mathrm{b}^{-1}$, branching fraction, $\mathcal{B} = (5.961 \pm 0.033)\%$ [2] and rapidity bin, $\Delta y = 0.5$, are not modified either.

The yields of coherent events per bin however must be evaluated one more time as the HeRSCheL's requirement is not fully efficient and some of the events are removed by this selection. The same method described in the previous measurement is used. First, a fit in the mass spectrum of dimuon is performed and the non-resonant contribution yield is determined within the limits of J/ψ tight mass selection, $3032 < M(\mu\mu) < 3162\,\mathrm{MeV}/c^2$. A second fit is performed in the $\ln(p_T^2)$ spectrum where the non-resonant contribution is constrained to be within the value determined in the the mass fit. The coherent yield is determined from this second fit and its values are used in Equation 5.9. The mass fits are shown in Figure 5.21. The $\ln(p_T^2)$ fits are shown in Figure 5.26. The yield of coherent J/ψ in bins of J/ψ rapidity is presented in the Table 5.9.

Table 5.9: Signal yield in bins of J/ψ rapidity after HeRSCheL selection.

J/ψ y bin	2.0-2.5	2.5-3.0	3.0-3.5	3.5-4.0	4.0-4.5
n_{coh}	65 ± 9	178 ± 14	217 ± 15	126 ± 12	28 ± 6

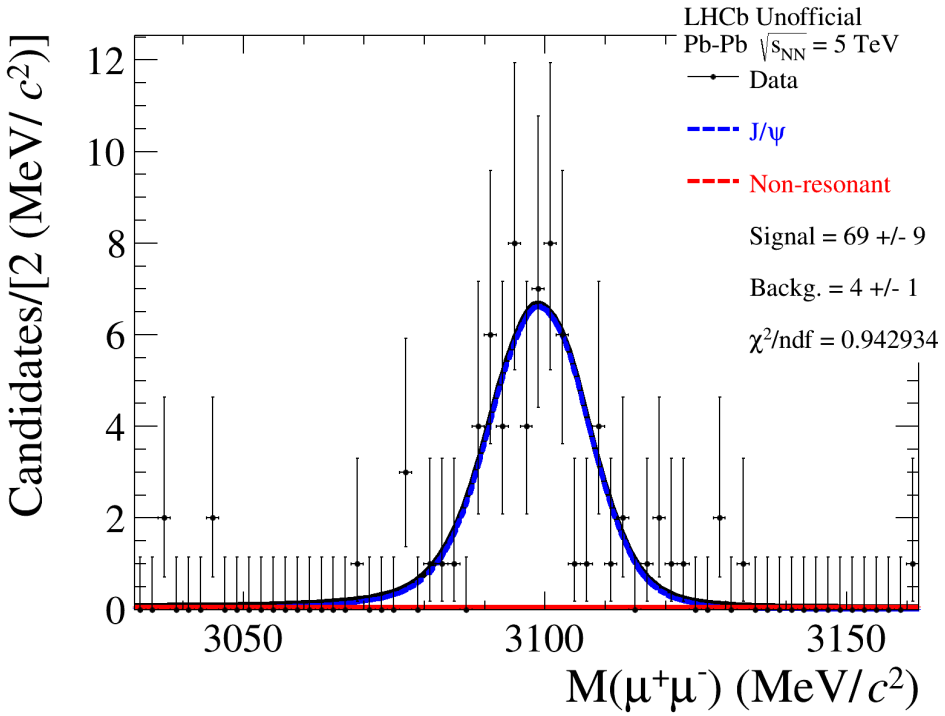

Figure 5.17: Mass fit in the first rapidity bin $2.0 < y(J/\psi) < 2.5$

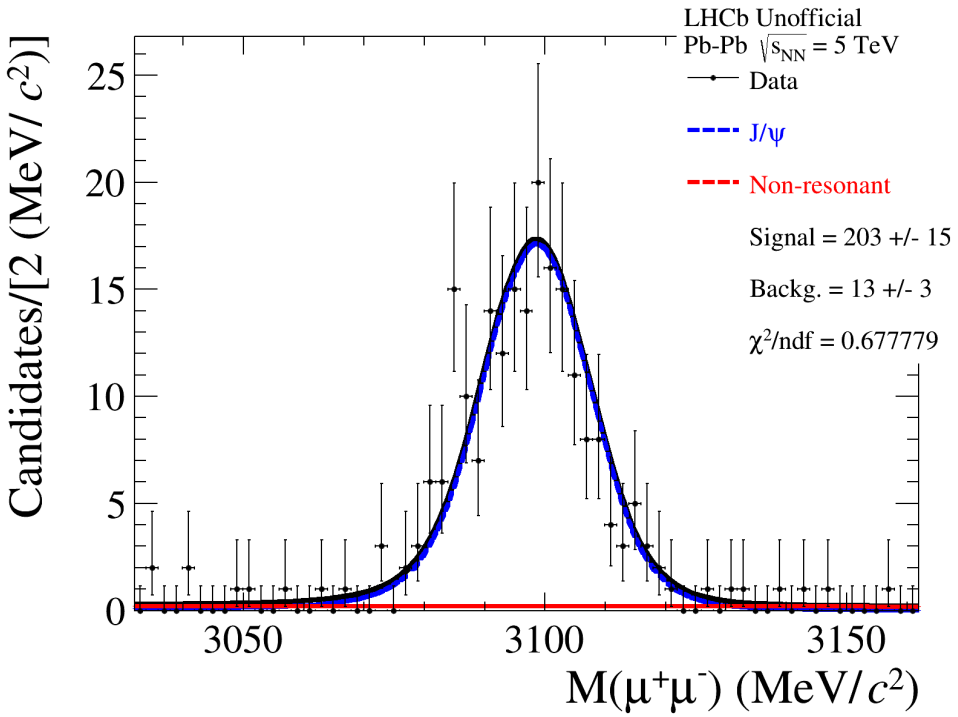

Figure 5.18: Mass fit in the first rapidity bin $2.5 < y(J/\psi) < 3.0$

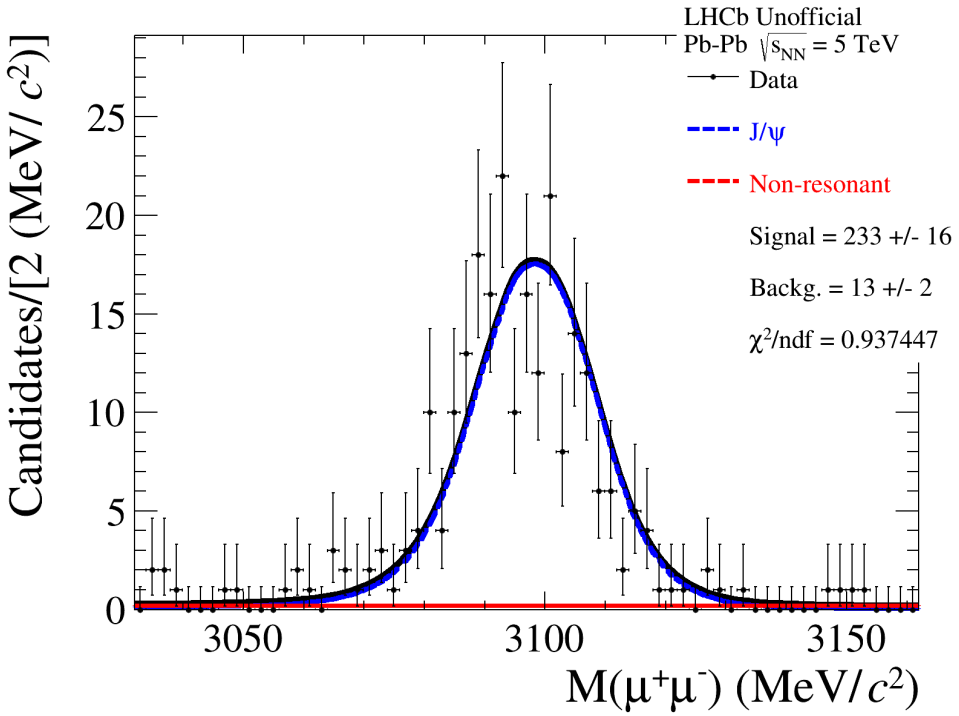

Figure 5.19: Mass fit in the second rapidity bin $3.0 < y(J/\psi) < 3.5$

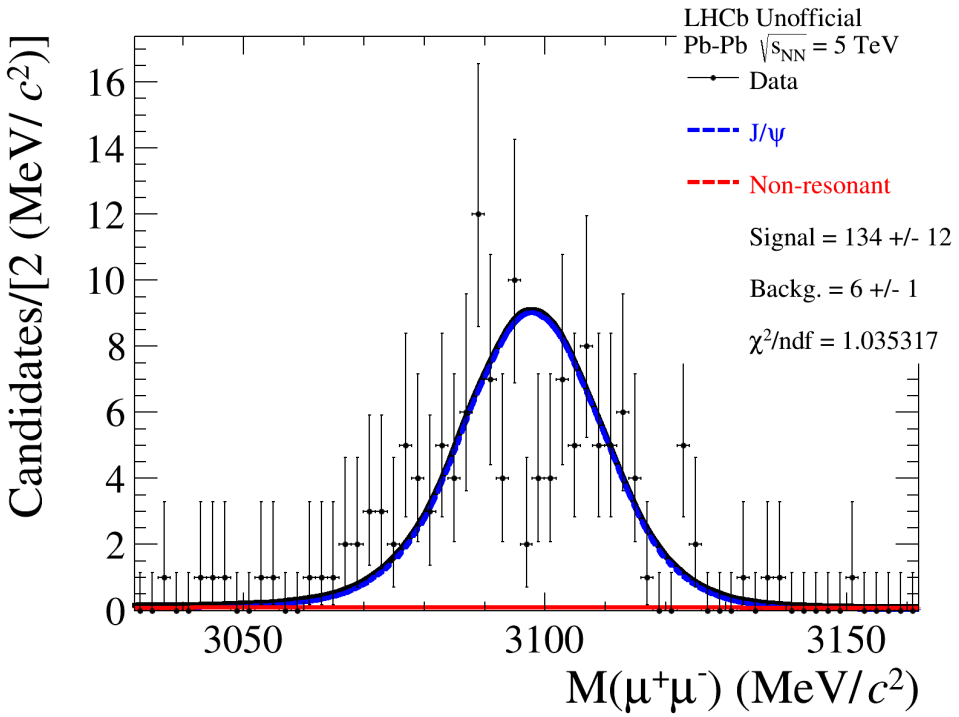

Figure 5.20: Mass fit in the first rapidity bin $3.5 < y(J/\psi) < 4.0$

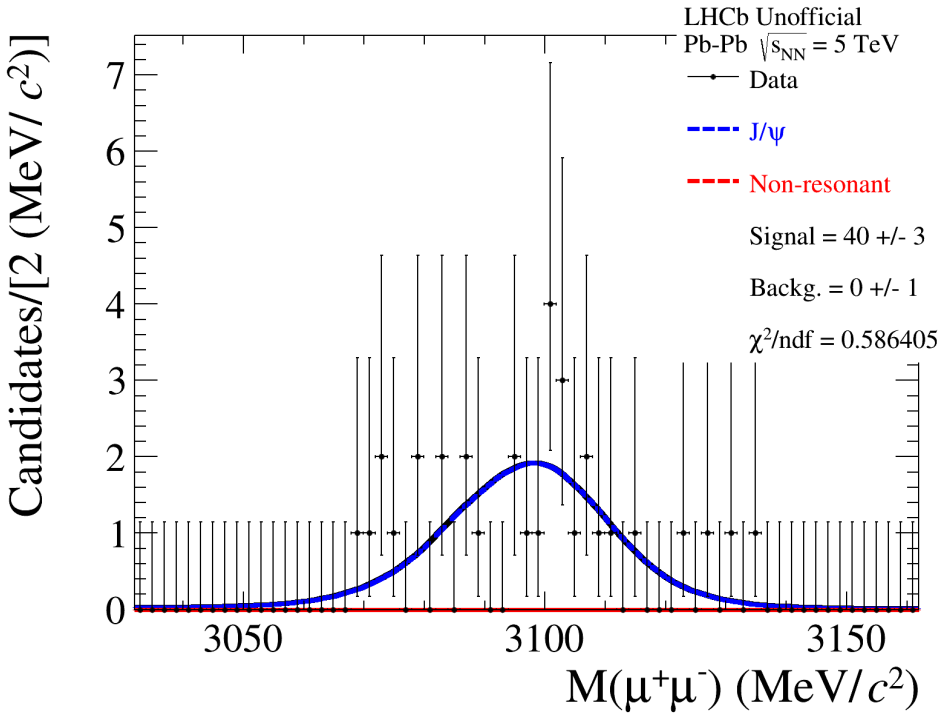

Figure 5.21: Mass fit in the second rapidity bin $4.0 < y(J/\psi) < 4.5$

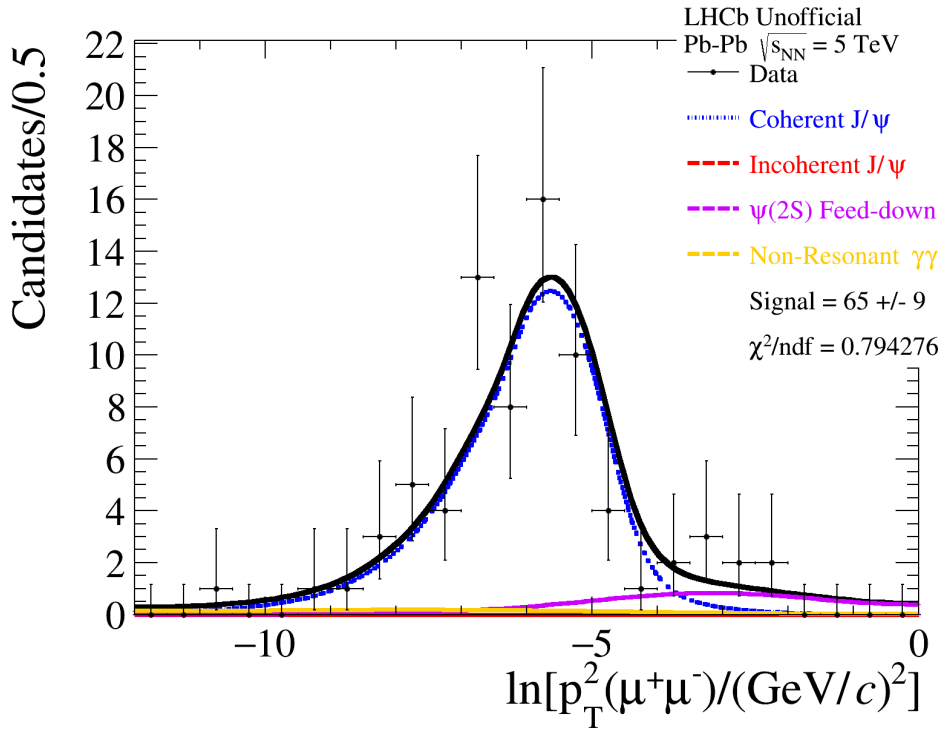

Figure 5.22: $\ln(p_T^2)$ fit in the first rapidity bin $2.0 < y(J/\psi) < 2.5$

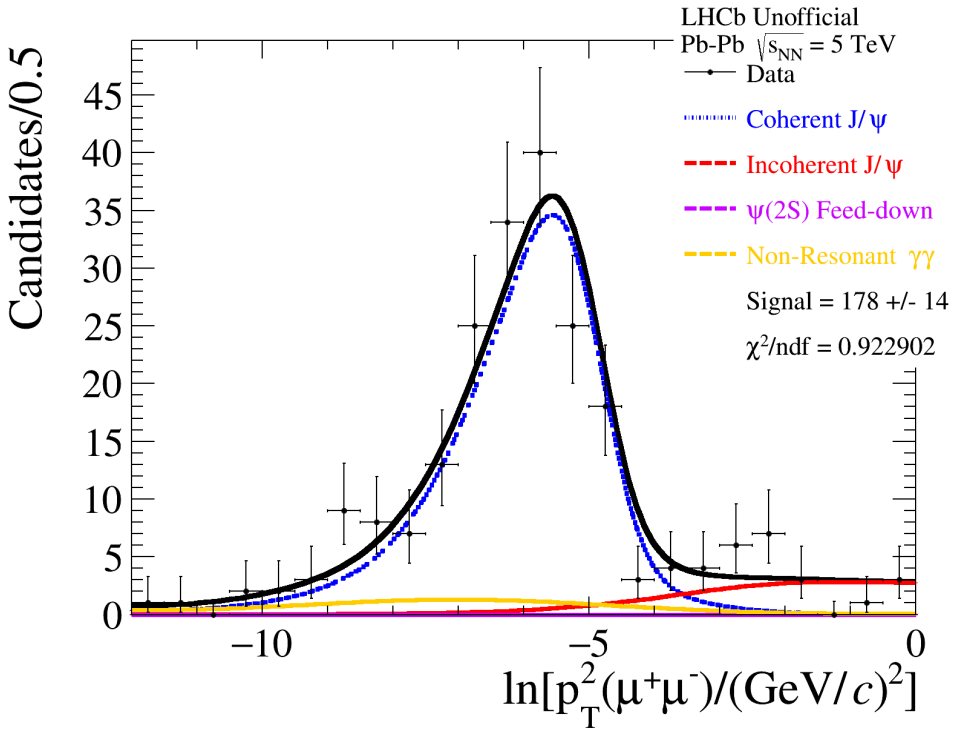

Figure 5.23: $\ln(p_T^2)$ fit in the first rapidity bin $2.5 < y(J/\psi) < 3.0$

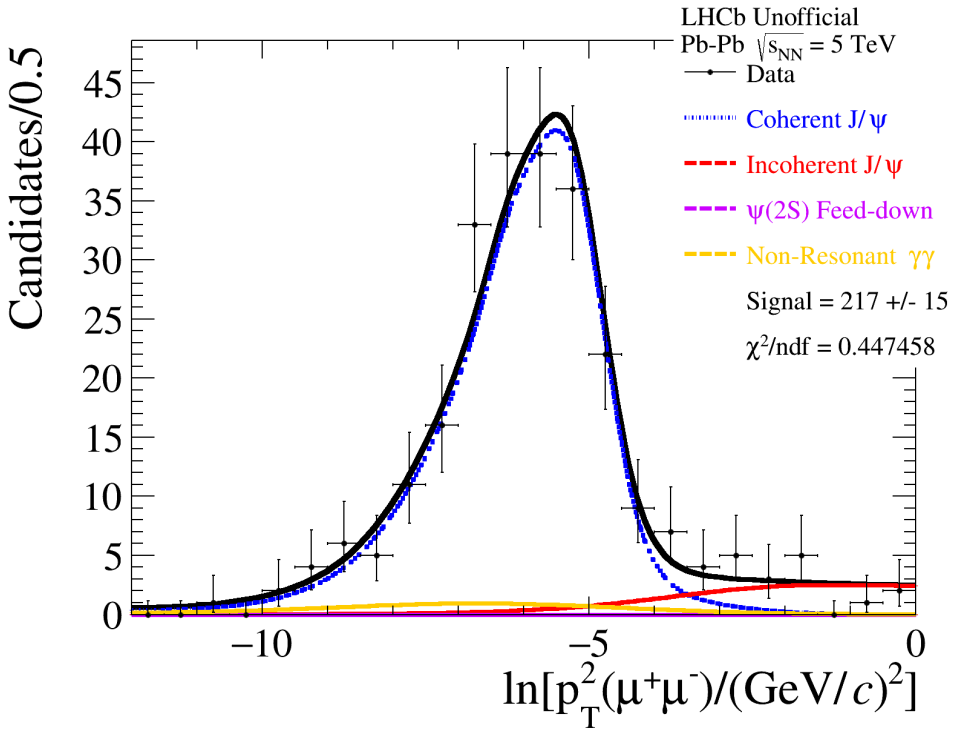

Figure 5.24: $\ln(p_T^2)$ fit in the second rapidity bin $3.0 < y(J/\psi) < 3.5$

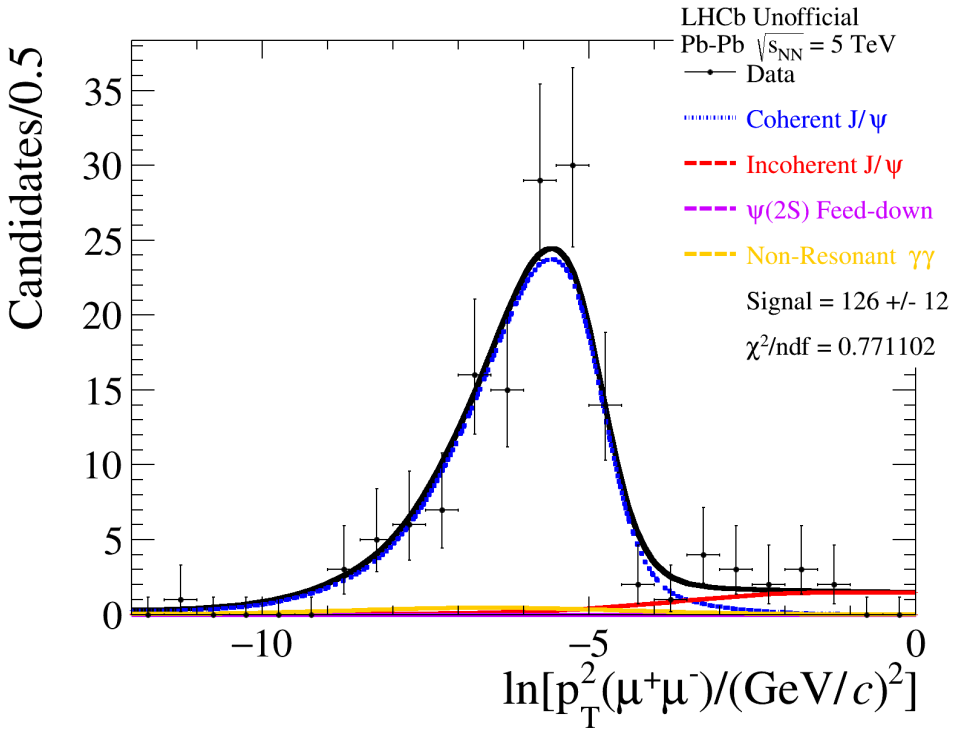

Figure 5.25: $\ln(p_T^2)$ fit in the first rapidity bin $3.5 < y(J/\psi) < 4.0$

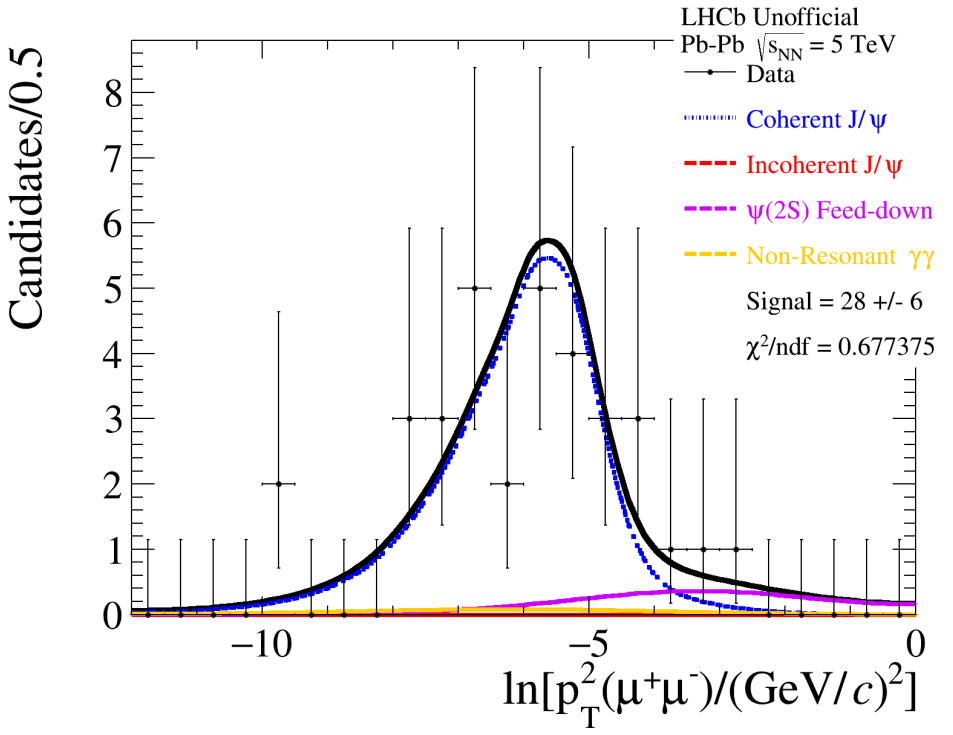

Figure 5.26: $\ln(p_T^2)$ fit in the second rapidity bin $4.0 < y(J/\psi) < 4.5$

The measured cross-section per meson rapidity bin can be seen in Table 5.10 where the uncertainties are statistical only. A comparison with the previous cross-section measurement is presented in the Figure 5.27. The theoretical predictions are presented in the same figure as lines and the ALICE measurement [59] is represented as well. The updated measurement is in agreement with most of the models. The two LHCb measurements are in agreement within their uncertainties. A better accuracy is expected due to the more realistic templates and less background contamination. In order to achieve it the fit models will be improved and the $\Delta\varphi$ selection will be applied in the main analysis as it is expected to be almost 100 % efficient and it can be helpful in order to reduce the incoherent background.

Table 5.10: Cross-section of UPC J/ψ production in bins of J/ψ rapidity with HeRSCheL's FOM selection.

J/ψ y bin	2.0-2.5	2.5-3.0	3.0-3.5	3.5-4.0	4.0-4.5
$\frac{\mathrm{d}\sigma}{\mathrm{d}y}(m\mathrm{b})$	2.88 ± 0.40	2.38 ± 0.19	2.20 ± 0.15	1.72 ± 0.16	1.18 ± 0.25

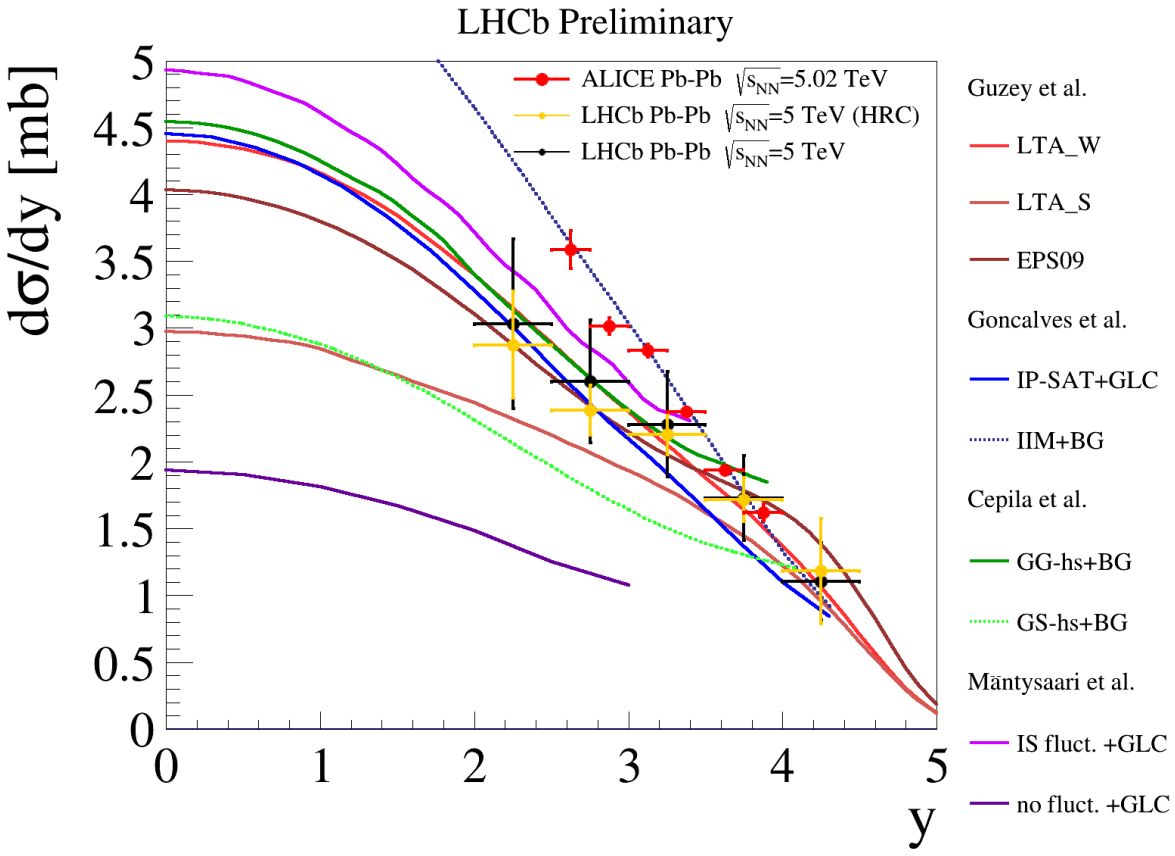

Figure 5.27: Differential cross-section for coherent J/ψ production compared to different phenomenological predictions. The LHCb measurements are shown as points, where the uncertainties are purely statistical for the HeRSCheL update (orange) and statistical and systematic for the former measurement (black). The ALICE measurement is represented by the red points [59].

Chapter 6

Conclusion

Two cross-section measurements of exclusive productions were performed with data collected by the LHCb experiment. The $\gamma\gamma \to \mu^+\mu^-$ central exclusive production was observed in pp collision data with center-of-mass energies $\sqrt{s} = 7$ and 8 TeV. The results, integrated over the LHCb acceptance, are:

$$\sigma(pp \to p\mu^+\mu^- p, \sqrt{s} = 7\,\text{TeV}) = (154.2 \pm 2.5)\,\text{pb} \tag{6.1}$$

$$\sigma(pp \to p\mu^+\mu^- p, \sqrt{s} = 8\,\text{TeV}) = (172.3 \pm 1.9)\,\text{pb} \tag{6.2}$$

where the uncertainties are statistical. A first prediction from QED is available. Foreseen developments of this analysis are the addition of systematic uncertainties and measurements in bins of dimuon rapidity.

The cross-section measurement of the coherent production of J/ψ was performed with PbPb collision data with a nucleus-nucleus center-of-mass energy $\sqrt{s_{\text{NN}}} = 5$ TeV. This measurement is presented in 5 bins of J/ψ rapidity and comparison with many phenomenological predictions is shown. The results are compatible mainly with the predictions using perturbative QCD approach. The theorists can use these results in order to enhance the accuracy of the models. The cross-section integrated over the rapidity interval $2 < y < 4.5$ is

$$\sigma(\text{PbPb} \to \text{Pb}J/\psi\text{Pb}, \sqrt{s_{\text{NN}}} = 5\,\text{TeV}) = (5.18 \pm 0.39)\,\text{mb}. \tag{6.3}$$

The addition of a HeRSCheL requirement, which enhances the purity of the signal sample, is the main difference between this result and the preliminary result shown in [60]. A requirement using the $\Delta\varphi$ variable is included in order to reduce further spurious background while keeping all signal candidates. The simulated events used to obtain the fit templates are updated in order to have the complete detector response simulation. The approval of of these changes by the LHCb collaboration is needed in order to publish the updated result presented in this thesis. Finally, the use of HeRSCheL detector in heavy ions coherent productions is found to be promising to help distinguishing true coherent processes in respect to inclusive productions.

Bibliography

[1] F. Halzen and Alan D. Martin. *QUARKS AND LEPTONS: AN INTRODUCTORY COURSE IN MODERN PARTICLE PHYSICS*. 1984. ISBN: 0471887412, 9780471887416.

[2] M. Tanabashi and other. "Review of Particle Physics". In: *Phys. Rev. D* 98 (3 Aug. 2018), p. 030001. DOI: 10.1103/PhysRevD.98.030001. URL: https://link.aps.org/doi/10.1103/PhysRevD.98.030001.

[3] K. Akiba et al. "LHC Forward Physics". In: *J. Phys.* G43 (2016), p. 110201. DOI: 10.1088/0954-3899/43/11/110201. arXiv: 1611.05079 [hep-ph].

[4] A. G. Shamov and Valery I. Telnov. "Precision luminosity measurement at LHC using two photon production of $\mu^+\mu^-$ pairs". In: *Nucl. Instrum. Meth.* A494 (2002), pp. 51–56. DOI: 10.1016/S0168-9002(02)01444-4. arXiv: hep-ex/0207095 [hep-ex].

[5] Morad Aaboud et al. "Evidence for light-by-light scattering in heavy-ion collisions with the ATLAS detector at the LHC". In: *Nature Phys.* 13.9 (2017), pp. 852–858. DOI: 10.1038/nphys4208. arXiv: 1702.01625 [hep-ex].

[6] G. Bélanger and F. Boudjema. "$\gamma\gamma \to W^+W^-$ and $\gamma\gamma \to ZZ$ as tests of novel quartic couplings". In: *Physics Letters B* 288.1 (1992), pp. 210–220. ISSN: 0370-2693. DOI: https://doi.org/10.1016/0370-2693(92)91979-J. URL: http://www.sciencedirect.com/science/article/pii/037026939291979J.

[7] Sylvain Fichet, Gero von Gersdorff, and Christophe Royon. "Scattering light by light at 750 GeV at the LHC". In: *Phys. Rev.* D93.7 (2016), p. 075031. DOI: 10.1103/PhysRevD.93.075031. arXiv: 1512.05751 [hep-ph].

[8] Vardan Khachatryan et al. "Evidence for exclusive $\gamma\gamma \to W^+W^-$ production and constraints on anomalous quartic gauge couplings in pp collisions at $\sqrt{s} = 7$ and 8 TeV". In: *JHEP* 08 (2016), p. 119. DOI: 10.1007/JHEP08(2016)119. arXiv: 1604.04464 [hep-ex].

[9] Eugene Levin. "An Introduction to pomerons". In: *High energy physics. Proceedings, LAFEX International School, Session C, Workshop on Diffractive Physics, LISHEP'98, Rio de Janeiro, Brazil, February 16-20, 1998*. 1998, pp. 261–336. arXiv: hep-ph/9808486 [hep-ph].

[10] T Regge. "Introduction to complex orbital momenta". In: *Il Nuovo Cimento* 14 (Dec. 1959), pp. 951–976. DOI: 10.1007/BF02728177.

[11] Carlos A. Bertulani, Spencer R. Klein, and Joakim Nystrand. "Physics of ultra-peripheral nuclear collisions". In: *Ann. Rev. Nucl. Part. Sci.* 55 (2005), pp. 271–310. DOI: 10.1146/annurev.nucl.55.090704.151526. arXiv: nucl-ex/0502005 [nucl-ex].

[12] Betty Abelev et al. "Coherent J/ψ photoproduction in ultra-peripheral Pb-Pb collisions at $\sqrt{s_{NN}} = 2.76$ TeV". In: *Phys. Lett.* B718 (2013), pp. 1273–1283. DOI: 10.1016/j.physletb.2012.11.059. arXiv: 1209.3715 [nucl-ex].

[13] H. Leutwyler. "On the history of the strong interaction". In: *Mod. Phys. Lett.* A29 (2014), p. 1430023. DOI: 10.1142/9789814603904_0005,10.1142/S0217732314300237. arXiv: 1211.6777 [physics.hist-ph].

[14] John Ellis. "The Discovery of the Gluon". In: *Int. J. Mod. Phys.* A29.31 (2014), p. 1430072. DOI: 10.1142/9789814618113_0012,10.1142/S0217751X14300725. arXiv: 1409.4232 [hep-ph].

[15] Richard P. Feynman. *QED: The Strange Theory of Light and Matter*. New Ed. Princeton University Press, Oct. 1988. ISBN: 0691024170.

[16] David Griffiths. *Introduction to elementary particles*. 2008. ISBN: 9783527406012.

[17] H. Fritzsch. *Quarks: The Stuff of Matter*. 2018. ISBN: 9783319985268.

[18] E. Rutherford. "The scattering of alpha and beta particles by matter and the structure of the atom". In: *Phil. Mag. Ser.6* 21 (1911), pp. 669–688. DOI: 10.1080/14786440508637080.

[19] Wikimedia Commons. *File:Standard Model of Elementary Particles.svg — Wikimedia Commons, the free media repository*. [Online; accessed 20-March-2019]. 2019. URL: https://bit.ly/2Htwhhb.

[20] S. Nussinov. "Colored Quark Version of Some Hadronic Puzzles". In: *Phys. Rev. Lett.* 34 (1975), pp. 1286–1289. DOI: 10.1103/PhysRevLett.34.1286.

[21] F. E. Low. "A Model of the Bare Pomeron". In: *Phys. Rev.* D12 (1975), pp. 163–173. DOI: 10.1103/PhysRevD.12.163.

[22] V. N. Gribov. "Possible Asymptotic Behavior of Elastic Scattering". In: *JETP Lett.* 41 (1961), pp. 667–669.

[23] V.M. Budnev et al. "The two-photon particle production mechanism. Physical problems. Applications. Equivalent photon approximation". In: *Physics Reports* 15.4 (1975), pp. 181–282. ISSN: 0370-1573. DOI: https://doi.org/10.1016/0370-1573(75)90009-5. URL: http://www.sciencedirect.com/science/article/pii/0370157375900095.

[24] Min-Shih Chen et al. "Lepton Pair Production from Two-Photon Processes". In: *Phys. Rev. D* 7 (11 June 1973), pp. 3485–3502. DOI: 10.1103/PhysRevD.7.3485. URL: https://link.aps.org/doi/10.1103/PhysRevD.7.3485.

[25] V. P. Gonçalves et al. "Exclusive and diffractive $\mu^+\mu^-$ production in pp collisions at the LHC". In: *Phys. Rev.* D97.7 (2018), p. 074024. DOI: 10.1103/PhysRevD.97.074024. arXiv: 1802.07339 [hep-ph].

[26] G. Kubasiak and A. Szczurek. "Exclusive and diffractive production of lepton pairs in *pp* collisions at high energies". In: *Workshop Excited QCD 2011, Les Houches, France, February 20–25, 2011*. 2011, pp. 773–779. DOI: DOI:10.5506/APhysPolBSupp.4.773. URL: https://www.actaphys.uj.edu.pl/fulltext?series=Sup&vol=4&page=773.

[27] E. J. Williams. "Correlation of certain collision problems with radiation theory". In: *Kong. Dan. Vid. Sel. Mat. Fys. Med.* 13N4.4 (1935), pp. 1–50.

[28] J. de Favereau de Jeneret et al. "High energy photon interactions at the LHC". In: (2009). arXiv: 0908.2020 [hep-ph].

[29] Nicolas Schul and Krzysztof Piotrzkowski. "Measurements of two-photon interactions at the LHC". 2011. URL: https://cds.cern.ch/record/1423327.

[30] L. N. Hand, D. G. Miller, and Richard Wilson. "Electric and Magnetic Form Factors of the Nucleon". In: *Rev. Mod. Phys.* 35 (2 Apr. 1963), pp. 335–349. DOI: 10.1103/RevModPhys.35.335. URL: https://link.aps.org/doi/10.1103/RevModPhys.35.335.

[31] J. R. Dunning et al. "Electromagnetic Structure of the Neutron and Proton". In: *Phys. Rev. Lett.* 13 (21 Nov. 1964), pp. 631–635. DOI: 10.1103/PhysRevLett.13.631. URL: https://link.aps.org/doi/10.1103/PhysRevLett.13.631.

[32] L. A. Harland-Lang, V. A. Khoze, and M. G. Ryskin. "Exclusive physics at the LHC with SuperChic 2". In: *Eur. Phys. J.* C76.1 (2016), p. 9. DOI: 10.1140/epjc/s10052-015-3832-8. arXiv: 1508.02718 [hep-ph].

[33] Serguei Chatrchyan et al. "Exclusive photon-photon production of muon pairs in proton-proton collisions at $\sqrt{s} = 7$ TeV". In: *JHEP* 01 (2012), p. 052. DOI: 10.1007/JHEP01(2012)052. arXiv: 1111.5536 [hep-ex].

[34] Georges Aad et al. "Measurement of exclusive $\gamma\gamma \to \ell^+\ell^-$ production in proton-proton collisions at $\sqrt{s} = 7$ TeV with the ATLAS detector". In: *Phys. Lett.* B749 (2015), pp. 242–261. DOI: 10.1016/j.physletb.2015.07.069. arXiv: 1506.07098 [hep-ex].

[35] M. Aaboud et al. "Measurement of the exclusive $\gamma\gamma \to \mu^+\mu^-$ process in proton-proton collisions at $\sqrt{s} = 13$ TeV with the ATLAS detector". In: *Phys. Lett.* B777 (2018), pp. 303–323. DOI: 10.1016/j.physletb.2017.12.043. arXiv: 1708.04053 [hep-ex].

[36] Dermot Moran. "Central Exclusive Production with Dimuon Final States at LHCb". University Coll., Dublin, 2011.

[37] S. P. Baranov et al. "LPAIR: A generator for lepton pair production". In: *Workshop on Physics at HERA Hamburg, Germany, October 29-30, 1991*. 1991, pp. 1478–1482.

[38] David d'Enterria and Gustavo G. da Silveira. "Observing light-by-light scattering at the Large Hadron Collider". In: *Phys. Rev. Lett.* 111 (2013). [Erratum: Phys. Rev. Lett.116,no.12,129901(2016)], p. 080405. DOI: 10.1103/PhysRevLett.111.080405,10.1103/PhysRevLett.116.129901. arXiv: 1305.7142 [hep-ph].

[39] S. Atag, S. C. Inan, and I. Sahin. "Extra dimensions in photon-induced two lepton final states at the CERN-LHC". In: *Phys. Rev.* D80 (2009), p. 075009. DOI: 10.1103/PhysRevD.80.075009. arXiv: 0904.2687 [hep-ph].

[40] S. Atag, S. C. Inan, and I. Sahin. "Extra dimensions in $\gamma\gamma \to \gamma\gamma$ process at the CERN-LHC". In: *JHEP* 09 (2010), p. 042. DOI: 10.1007/JHEP09(2010)042. arXiv: 1005.4792 [hep-ph].

[41] Rick S. Gupta. "Probing Quartic Neutral Gauge Boson Couplings using diffractive photon fusion at the LHC". In: *Phys. Rev.* D85 (2012), p. 014006. DOI: 10.1103/PhysRevD.85.014006. arXiv: 1111.3354 [hep-ph].

[42] Nicolas Schul and Krzysztof Piotrzkowski. "Detection of two-photon exclusive production of supersymmetric pairs at the LHC". In: *Nucl. Phys. Proc. Suppl.* 179-180 (2008), pp. 289–297. DOI: 10.1016/j.nuclphysbps.2008.07.036. arXiv: 0806.1097 [hep-ph].

[43] David M. Asner, Jeffrey B. Gronberg, and John F. Gunion. "Detecting and studying Higgs bosons at a photon-photon collider". In: *Phys. Rev.* D67 (2003), p. 035009. DOI: 10.1103/PhysRevD.67.035009. arXiv: hep-ph/0110320 [hep-ph].

[44] Piotr Lebiedowicz and Antoni Szczurek. "Exclusive production of heavy charged Higgs boson pairs in the $pp \to ppH^+H^-$ reaction at the LHC and a future circular collider". In: *Phys. Rev.* D91 (2015), p. 095008. DOI: 10.1103/PhysRevD.91.095008. arXiv: 1502.03323 [hep-ph].

[45] Enrico Fermi. "On the theory of collisions between atoms and electrically charged particles". In: *Nuovo Cim.* 2 (1925). [,243(1925)], pp. 143–158. DOI: 10.1007/BF02961914,10.1142/9789812704214_0026. arXiv: hep-th/0205086 [hep-th].

[46] C. F. v. Weizsäcker. "Ausstrahlung bei Stößen sehr schneller Elektronen". In: *Zeitschrift für Physik* 88.9 (Sept. 1934), pp. 612–625. ISSN: 0044-3328. DOI: 10.1007/BF01333110. URL: https://doi.org/10.1007/BF01333110.

[47] Robert N. Cahn and J. D. Jackson. "Realistic equivalent-photon yields in heavy-ion collisions". In: *Phys. Rev. D* 42 (11 Dec. 1990), pp. 3690–3695. DOI: 10.1103/PhysRevD.42.3690. URL: https://link.aps.org/doi/10.1103/PhysRevD.42.3690.

[48] G. Baur. "Coherent particle production in relativistic heavy ion collisions". In: *Nuclear Physics A* 538 (1992), pp. 187–191. ISSN: 0375-9474. DOI: https://doi.org/10.1016/0375-9474(92)90770-K. URL: http://www.sciencedirect.com/science/article/pii/037594749290770K.

[49] A. J. Baltz. "The Physics of Ultraperipheral Collisions at the LHC". In: *Phys. Rept.* 458 (2008). Ed. by G. Baur et al., pp. 1–171. DOI: 10.1016/j.physrep.2007.12.001. arXiv: 0706.3356 [nucl-ex].

[50] Adeola Adeluyi and C. A. Bertulani. "Constraining Gluon Shadowing Using Photoproduction in Ultraperipheral pA and AA Collisions". In: *Phys. Rev.* C85 (2012), p. 044904. DOI: 10.1103/PhysRevC.85.044904. arXiv: 1201.0146 [nucl-th].

[51] V. Guzey, E. Kryshen, and M. Zhalov. "Coherent photoproduction of vector mesons in ultraperipheral heavy ion collisions: Update for run 2 at the CERN Large Hadron Collider". In: *Phys. Rev.* C93.5 (2016), p. 055206. DOI: 10.1103/PhysRevC.93.055206. arXiv: 1602.01456 [nucl-th].

[52] L. Frankfurt, M. Strikman, and M. Zhalov. "Tracking Fast Small Color Dipoles through Strong Gluon Fields at the LHC". In: *Phys. Rev. Lett.* 102 (23 June 2009), p. 232001. DOI: 10.1103/PhysRevLett.102.232001. URL: https://link.aps.org/doi/10.1103/PhysRevLett.102.232001.

[53] Spencer R. Klein et al. "STARlight: A Monte Carlo simulation program for ultraperipheral collisions of relativistic ions". In: *Comput. Phys. Commun.* 212 (2017), pp. 258–268. DOI: 10.1016/j.cpc.2016.10.016. arXiv: 1607.03838 [hep-ph].

[54] Jan Cepila, Jesus Guillermo Contreras, and Michal Krelina. "Coherent and incoherent J/ψ photonuclear production in an energy-dependent hot-spot model". In: *Phys. Rev.* C97.2 (2018), p. 024901. DOI: 10.1103/PhysRevC.97.024901. arXiv: 1711.01855 [hep-ph].

[55] Heikki Mäntysaari and Björn Schenke. "Probing subnucleon scale fluctuations in ultraperipheral heavy ion collisions". In: *Phys. Lett.* B772 (2017), pp. 832–838. DOI: 10.1016/j.physletb.2017.07.063. arXiv: 1703.09256 [hep-ph].

[56] V. P. Gonçalves and M. V. T. Machado. "Vector meson production in coherent hadronic interactions: Update on predictions for energies available at the BNL Relativistic Heavy Ion Collider and the CERN Large Hadron Collider". In: *Phys. Rev. C* 84 (1 July 2011), p. 011902. DOI: 10.1103/PhysRevC.84.011902. URL: https://link.aps.org/doi/10.1103/PhysRevC.84.011902.

[57] L. Frankfurt, V. Guzey, and M. Strikman. "Leading Twist Nuclear Shadowing Phenomena in Hard Processes with Nuclei". In: *Phys. Rept.* 512 (2012), pp. 255–393. DOI: 10.1016/j.physrep.2011.12.002. arXiv: 1106.2091 [hep-ph].

[58] K. J. Eskola, H. Paukkunen, and C. A. Salgado. "EPS09: A New Generation of NLO and LO Nuclear Parton Distribution Functions". In: *JHEP* 04 (2009), p. 065. DOI: 10.1088/1126-6708/2009/04/065. arXiv: 0902.4154 [hep-ph].

[59] Shreyasi Acharya et al. "Coherent J/ψ photoproduction at forward rapidity in ultraperipheral Pb-Pb collisions at $\sqrt{s_{\mathrm{NN}}} = 5.02$ TeV". In: (2019). arXiv: 1904.06272 [nucl-ex].

[60] A. Bursche. "Study of coherent J/ψ production in lead-lead collisions at $\sqrt{s_{\mathrm{NN}}} =$ 5 TeV with the LHCb experiment". In: *Nucl. Phys.* A982 (2019), pp. 247–250. DOI: 10.1016/j.nuclphysa.2018.10.069.

[61] A. Augusto Alves Jr. et al. "The LHCb Detector at the LHC". In: *JINST* 3 (2008), S08005. DOI: 10.1088/1748-0221/3/08/S08005.

[62] Roel Aaij et al. "LHCb Detector Performance". In: *Int. J. Mod. Phys.* A30.07 (2015), p. 1530022. DOI: 10.1142/S0217751X15300227. arXiv: 1412.6352 [hep-ex].

[63] G. Aad et al. "The ATLAS Experiment at the CERN Large Hadron Collider". In: *Journal of Instrumentation* 3.08 (Aug. 2008), S08003–S08003. DOI: 10.1088/1748-0221/3/08/s08003. URL: https://doi.org/10.1088%2F1748-0221%2F3%2F08%2Fs08003.

[64] S. Shatrchyan et al. "The CMS experiment at the CERN LHC". In: *Journal of Instrumentation* 3.08 (Aug. 2008), S08004–S08004. DOI: 10.1088/1748-0221/3/08/s08004. URL: https://doi.org/10.1088%2F1748-0221%2F3%2F08%2Fs08004.

[65] Aamodt K. et al. "The ALICE experiment at the CERN LHC". In: *Journal of Instrumentation* 3.08 (Aug. 2008), S08002–S08002. DOI: 10.1088/1748-0221/3/08/s08002. URL: https://doi.org/10.1088%2F1748-0221%2F3%2F08%2Fs08002.

[66] J. W. G. Thomason et al. "Proton driver scenarios at CERN and Rutherford Appleton Laboratory". In: *Phys. Rev. ST Accel. Beams* 16 (5 May 2013), p. 054801. DOI: 10.1103/PhysRevSTAB.16.054801. URL: https://link.aps.org/doi/10.1103/PhysRevSTAB.16.054801.

[67] Torbjorn Sjostrand, Stephen Mrenna, and Peter Z. Skands. "A Brief Introduction to PYTHIA 8.1". In: *Comput. Phys. Commun.* 178 (2008), pp. 852–867. DOI: 10.1016/j.cpc.2008.01.036. arXiv: 0710.3820 [hep-ph].

[68] Torbjorn Sjostrand, Stephen Mrenna, and Peter Z. Skands. "PYTHIA 6.4 Physics and Manual". In: *JHEP* 05 (2006), p. 026. DOI: 10.1088/1126-6708/2006/05/026. arXiv: hep-ph/0603175 [hep-ph].

[69] Regis Lefevre. "Triggering with the LHCb calorimeters". In: *J. Phys. Conf. Ser.* 160 (2009), p. 012063. DOI: 10.1088/1742-6596/160/1/012063.

[70] K. Carvalho Akiba et al. "The HERSCHEL detector: high-rapidity shower counters for LHCb". In: *Journal of Instrumentation* 13.04 (Apr. 2018), P04017–P04017. DOI: 10.1088/1748-0221/13/04/p04017. URL: https://doi.org/10.1088%2F1748-0221%2F13%2F04%2Fp04017.

[71] R Antunes-Nobrega et al. *LHCb computing: Technical Design Report*. Technical Design Report LHCb. Submitted on 11 May 2005. Geneva: CERN, 2005. URL: https://cds.cern.ch/record/835156.

[72] M Clemencic et al. "The LHCb Simulation Application, Gauss: Design, Evolution and Experience". In: *Journal of Physics: Conference Series* 331.3 (Dec. 2011), p. 032023. DOI: 10.1088/1742-6596/331/3/032023. URL: https://doi.org/10.1088%2F1742-6596%2F331%2F3%2F032023.

[73] David J. Lange. "The EvtGen particle decay simulation package". In: *Nuclear Instruments and Methods in Physics Research Section A: Accelerators, Spectrometers, Detectors and Associated Equipment* 462.1 (2001). BEAUTY2000, Proceedings of the 7th Int. Conf. on B-Physics at Hadron Machines, pp. 152–155. ISSN: 0168-9002. DOI: https://doi.org/10.1016/S0168-9002(01)00089-4. URL: http://www.sciencedirect.com/science/article/pii/S0168900201000894.

[74] S. Agostinelli et al. "Geant4—a simulation toolkit". In: *Nuclear Instruments and Methods in Physics Research Section A: Accelerators, Spectrometers, Detectors and Associated Equipment* 506.3 (2003), pp. 250–303. ISSN: 0168-9002. DOI: https://doi.org/10.1016/S0168-9002(03)01368-8. URL: http://www.sciencedirect.com/science/article/pii/S0168900203013688.

[75] John Allison et al. "Geant4 developments and applications". In: *IEEE Trans. Nucl. Sci.* 53 (2006), p. 270. DOI: 10.1109/TNS.2006.869826.

[76] J. A. M. Vermaseren. "Two Photon Processes at Very High-Energies". In: *Nucl. Phys.* B229 (1983), pp. 347–371. DOI: 10.1016/0550-3213(83)90336-X.

[77] Roel Aaij et al. "Precision luminosity measurements at LHCb". In: *JINST* 9.12 (2014), P12005. DOI: 10.1088/1748-0221/9/12/P12005. arXiv: 1410.0149 [hep-ex].

[78] L. A. Harland-Lang, V. A. Khoze, and M. G. Ryskin. "Exclusive LHC physics with heavy ions: SuperChic 3". In: *Eur. Phys. J.* C79.1 (2019), p. 39. DOI: 10.1140/epjc/s10052-018-6530-5. arXiv: 1810.06567 [hep-ph].

[79] "Central exclusive production of J/ψ and $\psi(2S)$ mesons in pp collisions at $\sqrt{s} = 13$ TeV". In: (Aug. 2016). URL: https://cds.cern.ch/record/2209532.

[80] M. Oreglia. "A Study of the Reactions $\psi' \to \gamma\gamma\psi$". PhD thesis. SLAC, 1980. URL: http://www-public.slac.stanford.edu/sciDoc/docMeta.aspx?slacPubNumber=slac-r-236.html.